Transport Properties of LaTiO $_{3+\delta}$ and REBa $_2$ Cu $_3$ O $_{7-\delta}$ Thin Films: a Study of Correlation Effects

THÈSE

présentée à la Faculté des sciences de l'Université de Genève pour obtenir le grade de docteur ès sciences, mention physique

par

Stefano GARIGLIO

de

Gênes (Italie)

Thèse n° 3419

GENÈVE Atelier de Reproduction de la Section de Physique 2003 La Faculté des sciences, sur le préavis de Messieurs J.-M. TRISCONE, professeur ordinaire (Département de physique de la matière condensée) et directeur de thèse, Ø. FISCHER, professeur ordinaire (Département de physique de la matière condensée), K.A. MÜLLER, professeur (Université de Zurich – Institut de Physique), J.-P. LOCQUET, docteur (IBM Research Division, Zurich Research Laboratory – Rüschlikon) et J. FOMPEYRINE, docteur (IBM Research Division, Zurich Research Laboratory – Rüschlikon), autorise l'impression de la présente thèse, sans exprimer d'opinion sur les propositions qui y sont énoncées.

Genève, le 12 février 2003

Thèse - 3419 -

Le Doyen, Jacques WEBER

Contents

Ré	ésumé	en français	vii							
	R .1	Introduction	vii							
	R.2	Effet de champ ferroélectrique	viii							
		R.2.1 Modulation de la supraconductivité	ix							
		R.2.2 Modulation de T_c	X							
		R.2.3 Transition supraconducteur-isolant	хi							
		R.2.4 Modulation des propriétés dans l'état normal	хi							
	R.3	Couches minces de LaTi $O_{3+\delta}$	xiv							
In	trodu	ction	1							
Main goal of the Thesis										
	Outl	ine of the Thesis	3							
1	Electron correlations in solids 5									
	1.1	Metal-insulator transition	5							
	1.2	Mott insulator	6							
	1.3	Hubbard model	6							
	1.4	Slater's theory of Mott insulators	8							
	1.5	MIT phase diagram	9							
	1.6	Polarons	10							
	1.7	Anomalous metallic phases	11							
	1.8	High- T_c superconductors	11							
		1.8.1 Crystal and electronic structure	12							
		1.8.2 Phase diagram	13							

<u>ii</u> Contents

	1.9	LaTiO ₃ : structure and phase diagram	14				
2	Exp	erimental set-up	۱7				
	2.1	Thin film deposition	17				
		2.1.1 Sputtering	18				
		2.1.2 Molecular Beam Epitaxy	19				
	2.2	Structural analysis of thin films	20				
		2.2.1 X-ray analyses	20				
		2.2.2 Transmission Electron Microscopy	22				
	2.3	Lithographic patterning	23				
	2.4	Transport measurements: resistivity and Hall effect	23				
3	Ferr	roelectric Field Effect in thin superconducting films	25				
	3.1	Ferroelectric Field Effect	25				
	3.2	High-Temperature Superconductivity	26				
		3.2.1 The polaron-bipolaron model	27				
		3.2.2 The spin fluctuation scenario	28				
	3.3 Ferroelectricity						
		3.3.1 Sawyer-Tower circuit	30				
	3.4	Ferroelectric Field Effect Devices					
	3.5	Thin Film Growth and Characterization	33				
		3.5.1 Cuprate growth	33				
		3.5.2 Finite size effect in High- T_c thin films	34				
		3.5.3 PZT thin films	37				
3.6 Modulation of Superconductivity		Modulation of Superconductivity	39				
		3.6.1 PZT/GBCO/PBCO heterostructures	39				
		3.6.2 $P-E$ and $R-E$ loops	39				
		3.6.3 Shift of T_c	10				
		3.6.4 Superconductor-insulator transition	12				
	3.7	Modulation of Normal State Properties	18				
		3.7.1 PZT/NBCO heterostructures	18				

Contents

		3.7.2	Lithographic patterning of FFE heterostructures	49			
		3.7.3	Local ferroelectric poling	50			
		3.7.4	Resistance and Hall modulation	51			
		3.7.5	Variable <i>versus</i> fixed carrier density	52			
		3.7.6	Anderson localization of bipolarons	54			
		3.7.7	Two scattering times model	55			
		3.7.8	Implication of the modulation of the normal state properties	55			
4	LaT	$\mathbf{iO}_{3+\delta}$ \mathbf{t}	hin films: growth and transport properties	61			
4.1 Growth of LaTiO _{3+δ} thin films		h of LaTi $O_{3+\delta}$ thin films $\ldots \ldots \ldots \ldots \ldots \ldots$	62				
4.2 Structural analysis				64			
4.3 Transport properties for films prepared on (001) LAO substrates .		port properties for films prepared on (001) LAO substrates	68				
		4.3.1	Transport mechanism	70			
	4.4	Films	prepared on (001) STO substrates	74			
Co	Conclusions						
A	Acknowledgements						
Re	References						

<u>iv</u> Contents

Abbreviations

AF antiferromagnetic/antiferromagnet AFM atomic force microscope/microscopy

ARPES

angle-resolved photoemission spectroscopy

Bardeen-Cooper-Schrieffer BCS

DPMC Departement de Physique de la Matière Condensée

ferroelectric field effect FFE

Fermi liquid FL FS Fermi surface

full width at half maximum **FWHM**

high-temperature superconductor HTSC

MBE molecular beam epitaxy MIT metal-insulator transition **NMR** nuclear magnetic resonance

reflection high-energy electron diffraction **RHEED**

SI superconductor-insulator

STM scanning tunneling microscope/miscroscopy

transmission electron microscope **TEM**

GBCO GdBa₂Cu₃O₇

LAO LaAlO₃

 $La_{1-x}Sr_xTiO_3$ LSTO LaTiO_{3+ δ} LTO **NBCO** NdBa₂Cu₃O₇ PrBa₂Cu₃O₇ **PBCO PZT** $Pb(Zr_{0.2}Ti_{0.8})O_3$

STO SrTiO₃

REBa₂Cu₃O₇ RE=Y, Nd, Gd Y123/123

<u>vi</u> Abbreviations

Résumé

R.1 Introduction

La théorie conventionnelle des solides, basée sur la mécanique quantique des électrons libres se déplaçant dans un potentiel périodique, fournit une excellente description des éléments s'étendant du silicium semi-conducteur à l'aluminium supraconducteur. Cependant, au cours des cinquante dernières années et en particulier pendant les quinze dernières années, il est apparu de plus en plus clairement qu'il existe des substances pour lesquelles l'approche conventionnelle échoue. Ce sont notamment certains oxydes de métaux de transition, comprenant les supraconducteurs à hautes températures et les manganites. La propriété commune de ces composés est leur densité de porteurs relativement faible qui se situe entre celle des semi-conducteurs avec des densités de porteurs s'étendant de 10^{14} à 10^{18} charges/cm³ et celle des métaux avec des densités de l'ordre de 10^{22} charges/cm³. Une des conséquences de cette relative faible densité de porteurs est qu'ils sont moins fortement écrantés que dans les métaux ordinaires, augmentant ainsi leurs corrélations électroniques (par exemple, la répulsion de Coulomb).

Les propriétés électroniques de ces "nouveaux" matériaux sont fortement affectées par les interactions électroniques, ayant pour conséquence des comportements uniques observés lors de changements de température ou lors de l'application d'un champ magnétique. Ces nouveaux matériaux montrent également souvent des diagrammes de phase complexes en fonction du dopage, relié au nombre de porteurs dans le système. Cette complexité est à la fois stimulante car les nouveaux phénomènes ne sont pas toujours compris, et attrayante, les applications potentielles de ces propriétés étant multiples. Ces possibilités passionnantes ont sensiblement amplifié la recherche sur les oxydes de métaux de transition durant ces quinze dernières années. Il existe de multiples possibilités permettant d'explorer les propriétés électroniques et les diagrammes de phase de ces matériaux. Dans cette thèse nous avons éxploré l'effet de champ ferroéléctrique dans les oxydes supraconducteurs et nous avons étudié les propriétés de transport d'un composé particulièrement intéressant, le LaTiO $_{3+\delta}$.

viii Résumé

R.2 Effet de champ ferroélectrique

Lorsqu'un champ électrique est appliqué à travers une couche isolante à la surface d'un semi-conducteur, on peut changer la résistivité de ce dernier de nombreux ordres de grandeur en raison de la formation d'une couche faible ou riche en nombre de porteurs dans la région d'interface. Cet effet, appelé l'effet de champ, est à la base du fonctionnement du transistor à effet de champ, dispositif au coeur de l'électronique moderne. L'effet de champ peut également être observé dans des métaux et des supraconducteurs, bien que son amplitude soit sensiblement diminuée par rapport aux semiconducteurs en raison de l'écrantage du champ électrique par une plus grande densité de porteurs libres. Dans les supraconducteurs, l'utilisation de l'effet de champ permet de moduler les propriétés supraconductrices telles que la température critique ou le courant critique. Suite à la découverte des supraconducteurs à haute température critique en 1986 par Bednorz et Müller [1], l'intérêt dans des expériences d'effet de champ s'est accru car les proprietées de ces matériaux sont extrêmement sensibles à de petits changements de la concentration de porteurs.

Une approche alternative à l'application d'un champ électrique externe consiste à remplacer le matériel diélectrique par un material ferroélectrique. Le ferroélectrique peut être décrit comme un diélectrique avec un moment dipolaire électrique différent de zéro en l'absence d'un champ électrique. Ce moment électrique macroscopique est spontané et non-volatile, et peut être inversé en appliquant un champ électrique plus grand que le champ coercitif à travers le matériau. Il est ainsi possible d'injecter ou d'enlever des porteurs dans le supraconducteur juste à l'interface d'une hétérostructure composée d'un ferroéléctrique et d'un supraconducteur. On peut ainsi changer les propriétés du supraconducteur en basculant la direction de polarisation du ferroélectrique.

L'avantage d'une polarisation non-volatile dans un dispositif d'effet de champ ferroéléctrique réside justement dans la possibilité d'induire un changement non-volatile de la densité de charge. Cela nous permet de mesurer les propriétés de transport du supraconducteur sans qu'aucune tension ne soit appliquée à travers le ferroéléctrique. Cette même propriété nous permet de remplacer l'électrode métallique du ferroélectrique par la pointe conductrice mobile d'un microscope à force atomique (AFM). L'idée est de balayer avec l'AFM la région ferroélectrique où l'on souhaite inverser la polarisation en appliquant une tension entre la pointe du microscope et le canal de charge. Cette technique s'est avérée efficace pour modifier localement la densité de charge [2].

Si la charge induite par effet de champ ferroélectrique participe entièrement à la conduction, on peut expliciter le changement de la concentration de porteurs mobiles moyenné sur l'épaisseur d du film métallique de la façon suivante

$$\Delta n = \frac{2P_r}{ed} \tag{R.1}$$

où P_r est la polarisation rémanente du matériau ferroélectrique et e la charge élémentaire. La polarisation rémanente P_r de notre matériau ferroéléctrique, le Pb(Zr_{0.2}Ti_{0.8})O₃ (PZT), se situe entre 15 et 45 μ C/cm². Cette polarisation produit un changement de porteurs

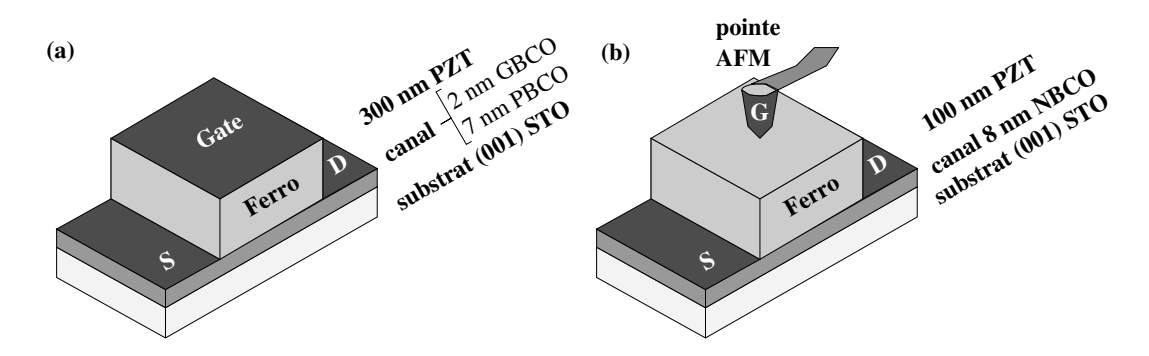


Figure R.1: Vue schématique des dispositifs d'effet de champ ferroélectrique. Gauche: pour des expériences de modulation de supraconductivité dans des dispositifs conventionels d'effet de champ nous avons déposé sur un substrat de SrTiO₃ (STO) orienté (001) une couche mince de PBCO, une couche supraconductrice ultra-mince de GBCO et une couche de PZT. Droite: pour des expériences de modulation dans l'état normal dans des dispositifs permettant l'approche locale par microscope à force atomique nous avons déposé sur un substrat de STO orienté (001) une couche supraconductrice mince de NBCO et une couche de PZT.

de Δn =2-5·10²¹ cm⁻³ dans une cellule unitaire d'une épaisseur de 1 nm. Cette valeur correspond à la densité de porteur dans un supraconducteur à haute temperature critique avec un dopage optimal et montre que le potentiel de l'effet de champ ferroélectrique sur ces matériaux est important. Comme on peut le voir dans la formule R.1, l'effet de champ est fortement réduit lorsque l'épaisseur de la couche augmente.

R.2.1 Modulation de la supraconductivité

Le schéma des hétérostructures utilisées pour moduler la supraconductivité dans des couches ultra-minces d'oxide de cuivre est présenté sur la figure R.1(gauche). La croissance des hétérostructures de PZT/GBCO/PBCO est effectuée par la méthode de pulvérisation cathodique à magnétron. Nous avons caractérisé les couches ferroélectriques par une mesure d'hystérèse ferroélectrique à l'aide d'un circuit de Sawyer-Tower. La figure R.2 affiche la mesure effectuée sur une hétérostructure de 300 nm PZT/2 nm GdBa₂Cu₃O₇(GBCO)/7,2 nm PrBa₂Cu₃O₇ (PBCO): la couche ferroélectrique a une polarisation rémanante de $\sim 10 \ \mu \text{c/cm}^2$ et un champ coercitif de 100 kV/cm. Nous avons également examiné les propriétés ferroélectriques en mesurant la résistance à température ambiante d'une bicouche GBCO/PBCO dans une hétérostructure du type présenté dans la figure R.1 en fonction du champ électrique appliqué à travers la couche ferroélectrique. Après avoir appliqué une tension pendant environ une seconde à travers le ferroélectrique, nous avons mesuré la résistance de la bicouche. En répétant ce procédé pour une série de différentes tensions, l'hystérèse ferroélectrique a été observée. La figure R.2 montre une boucle résistance en fonction du champ électrique (R-E) mesurée sur le même échantillon que celui utilisé par la mesure Sawyer-Tower. Nous observons un changement de 10% de la résistance de la bicouche GBCO/PBCO entre les deux états de polarisation du PZT.

x Résumé

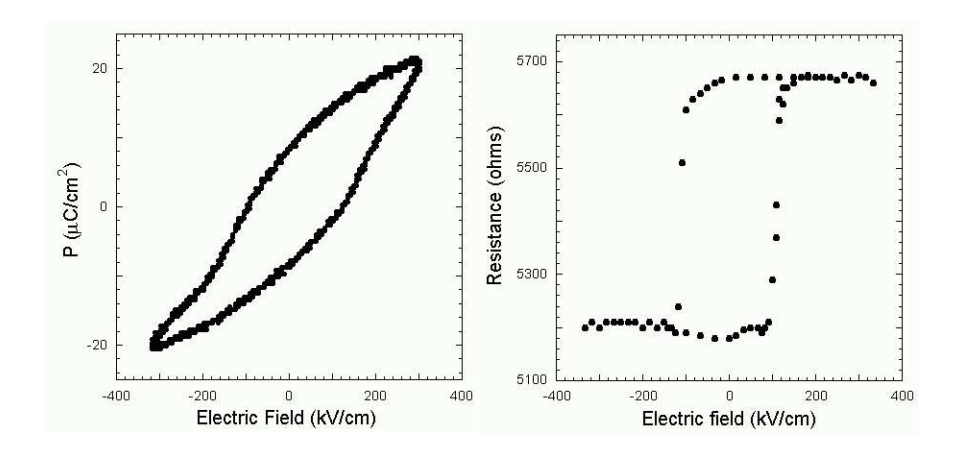


Figure R.2: (gauche) Boucle d'hystérèse ferroélectrique P-E d'une hétérostructure de PZT/GBCO/PBCO obtenu par la methode de Sawyer-Tower. (droite) Boucle d'hystérèse ferroélectrique R-E de la même hétérostructure obtenu avec une mesure resistive.

On peut également observer que le signe du changement de la résistance est en accord avec le caractère des porteurs du GBCO (trous). L'état de la résistance après l'application de la tension est stable pendant des semaines (la longueur des expériences) et réversible, comme démontré par l'hystérèse.

R.2.2 Modulation de T_c

Nous avons aussi étudié les propriétés de transport à basse température de ces hétérostructures. La résistivité d'une hétérostructure de 300 nm de PZT/2 nm GBCO/7,2 nm PBCO en fonction de la température pour les deux états de polarisation de la couche de PZT est montrée sur la figure R.3(A). La résistivité observée résulte de la contribution des deux couches reliées en parallèle: la couche de PBCO qui a un comportement semi-conducteur et la couche de GBCO qui est métallique et devient supraconductrice à la température de \sim 20 K. A température ambiante nous avons mesuré un changement de résistivité de 15% en inversant la polarisation de PZT. A la température critique l'effet de champ augmente jusqu'à ~50% et induit un décalage de 7 K entre les deux courbes de résistivité, le décalage étant maintenu dans toute la région de transition, comme démontré dans la figure R.3(B). Pour la courbe supérieure, le vecteur de polarisation se dirige vers le substrat, correspondant à une diminution des trous dans le GBCO, et a comme conséquence une diminution de la température critique. La courbe inférieure quant à elle correspond à une augmentation des trous du système. Afin de mieux quantifier l'effet de champ ferroélectrique, nous avons effectué des mesures d'effet Hall pour déterminer la concentration de porteurs de ces films. Les mesures de la constante de Hall à 100 K suggèrent une densité de porteur de $\sim 2~10^{21}$ trous/cm³. En utilisant la polarisation remanente mesurée de 10 μ C/cm², on peut calculer que le champ de polarisation du ferroéléctrique enlève 6·10²⁰ trous/cm³ dans notre couche de GBCO d'une épaisseur de 2 nm ($\Delta n = P/ed$).

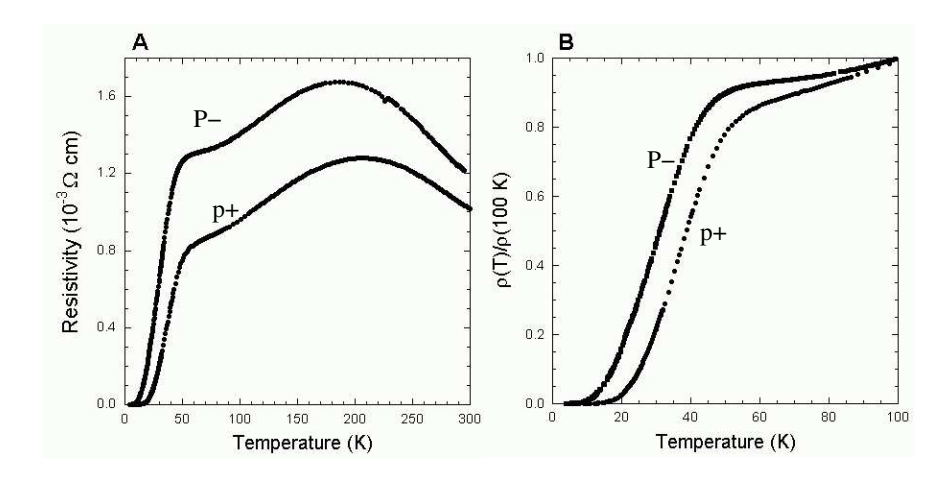


Figure R.3: (A) Résistivité en function de la température d'une hétérostructure de 300 nm de PZT/2 nm GBCO/7,2 nm PBCO pour les deux états de polarisation du PZT. La courbe supérieure (P-) correspond à une diminution des trous du GBCO, ayant pour résultat une augmentation de la résistivité dans l'état normal et une diminution de la temperature critique de 7 K. (b) Zoom des données présentées en (A). La résistivité des deux courbes a été normalisées à 100 K.

R.2.3 Transition supraconducteur-isolant

La figure R.4 montre la résistivité en fonction de la température pour une hétérostructures de 300 nm de PZT/2 nm GBCO/7,2 nm PBCO. Pour les courbes inférieures, la résistivité est essentiellement indépendante de la température jusqu'à ~50 K, où le début de la transition supraconductrice se produit. Les différentes courbes pour un état de polarisation ferroélectrique donné correspondent à des mesures faites à des champs magnétiques différents. On peut observer que l'application de champs magnétiques jusqu'à 7 T endessous de 50 K élargit sensiblement la transition résistive. En revanche, les courbes supérieures, qui correspondent à une diminution de trous, ont un comportement isolant dans toute la plage de température étudiée. Dans ces expériences nous avons ainsi induit pour la première fois une transition entre un état supraconducteur et un état isolant par un effet purement électrostatique. L'analyse des mesures de transport dans l'état isolant suggère que cet état isolant induit par effect de champ est différent de celui obtenu par dopage chimique.

R.2.4 Modulation des propriétés dans l'état normal

Déterminer le rôle de la densité de porteurs dans les dépendances en température des conductivité longitudinale et transversale dans les supraconducteurs à haute temperature critique est une tâche expérimentale difficile. Le dopage chimique, qui est la technique la plus généralement employée pour changer le dopage, induit invariablement du désordre, rendant l'interprétation des données difficile. Notre approche expérimentale, basée

xii Résumé

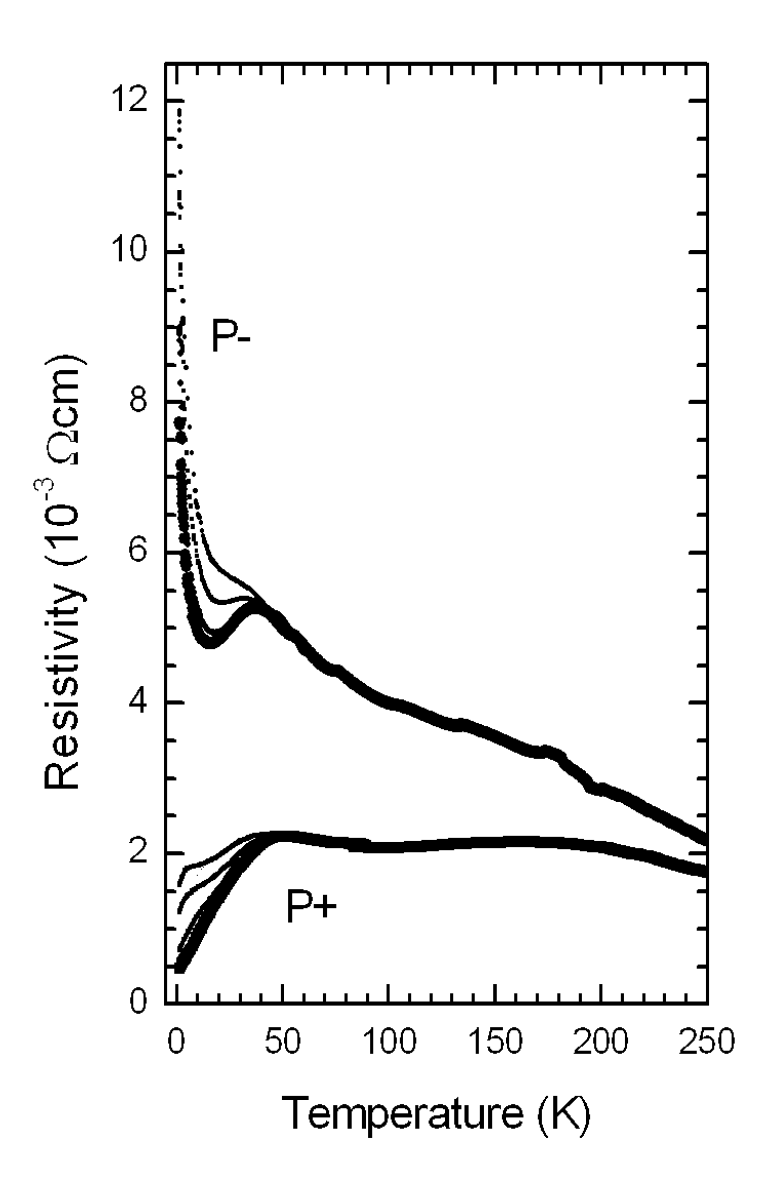
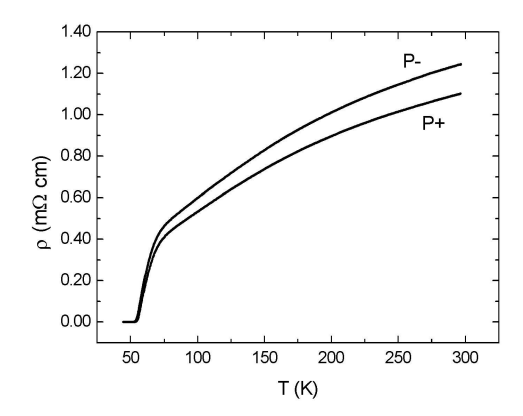


Figure R.4: Résistivité en fonction de la température d'une hétérostructure de 300 nm de PZT/2 nm GBCO/7,2 nm PBCO pour les deux états de polarisation de la couche de PZT. Les courbes supérieures correspondant à une diminution de trous, ont un comportement isolant sur toute la plage de températures étudiée. Les courbes épaisses sont des mesures en champ magnetique nul, tandis que les autres courbes sont des mesures pour des champs magnétiques de 1, 4 et 7 T.



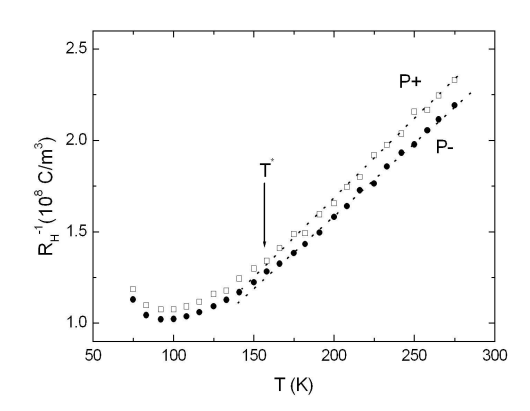


Figure R.5: (Gauche) Résistivité en fonction de la température pour les deux états de polarisation du ferroélectrique. P^+ est la direction de la polarisation qui ajoute des trous à la couche supraconductrice.(Droite) Inverse de la constante de Hall R_H^{-1} en fonction de la température pour les deux états de polarisation. Les lignes pointillées sont des fits aux données dans la région linéaire.

sur l'effet de champ ferroélectrique où la modulation de la concentration des porteur de charge est controllée, bien definie et, ne modifiant en rien la structure, nous a permis d'étudier le rôle de la concentration des porteurs dans la résistivité et la constante de Hall. La figure R.1(droite) montre une vue schématique des dispositifs utilisés dans cette étude. Afin d'éviter la difficulté d'avoir deux couches "conduisant" en parallèle, nous n'avons utilisé qu'une seule couche supraconductrice de NdBa₂Cu₃O₇ (NBCO). Pour obtenir des informations quantitatives sur les propriétés de transport du supraconducteur, nous avons localement inversé la polarisation ferroéléctrique à l'aide d'un microscope à force atomique sur des petites pistes, définies par un processus lithographique. La figure R.5(gauche) montre la résistivité d'une hétérostructure de 100 nm de PZT/8 nm NBCO en fonction de la température pour les deux états de polarisation. On observe pour les deux polarisations que la résistivité est métallique dans l'état normal et va à zéro aux alentours de 50 K. La différence dans la résistivité entre les deux états de polarisation est d'environ 9% et est essentiellement constante en function de la température. Nous avons ensuite effectué des mesures d'effet Hall sur ces échantillons. Dans la figure R.5(droite) nous montrons l'inverse de la constante de Hall ${\cal R}_H^{-1}$ en fonction de la température pour les deux états de polarisation. Comme cela peut être vu dans les données, l'effet de champ ferroélectrique induit un changement d'environ 6% dans la constante de Hall. Dans la théorie la plus simple de l'effet Hall, l'inverse de la constante de Hall est reliée à la densité de porteur n: $R_H^{-1} = qn$, où q est la charge des porteurs. Dans les supraconducteurs à hautes températures critiques où la constante de Hall dépend de la température, la valeur de R_H^{-1} à une température donnée (habituellement 100 K) peut être reliée au dopage du matériel et de ce fait également à sa concentration de porteurs. Le changement de R_H^{-1} démontre ainsi directement la variation de la concentration de charge produite par l'inversion de la polarxiv Résumé

isation. Si on essaye d'estimer le champ de polarisation en utilisant les données de Hall (voir formule R.1), $\Delta R_H^{-1} \sim 2~10^7~\text{C/m}^3$ à 100 K dans une couche d'épaisseur d'environ 10 nm, on obtient une polarisation de $\sim \! 10~\mu\text{C/cm}^2$, une valeur qui est bien conforme à la polarisation mesurée dans ces hétérostructures.

Comme la polarisation ferroélectrique de PZT est indépendante de la température endessous de la température ambiante [3], on s'attend à ce que le changement Δn induit par la polarisation soit constant en fonction de la température ($\Delta n = P/ed$). Cependant, les données expérimentales montrent que ΔR_H^{-1} n'est pas constant en fonction de la température. Dans un scénario où la resisitivé ρ et l'effet Hall R_H sont inversément proportionels à une densité de porteurs n indépendants de la température, comme dans un model à electrons libres, on doit pouvoir faire coïncider les deux courbes de resistivité et d'effet Hall pour les deux états de polarisation. Les courbes de résistivité et de l'inverse de la constante de Hall de la figure R.5 renormalisées à 100 K coïncident parfaitement entre elles sur la plage de température étudiée.

Nos données d'effet de champ dans l'état normal suggèrent que la conductivité longitudinale et transverse sont proportionnelles à la densité de porteurs. La modulation de champ de la réponse de Hall en particulier suggère que la concentration de porteurs dans les oxydes supraconducteurs à base de cuivre ne dépend pas de la température. La dépendance en température de la constante de Hall observée expérimentalement pourrait être reliée à la présence de differents temps de relaxation pour les porteurs.

R.3 Couches minces de LaTiO_{$3+\delta$}

Le deuxième sujet de recherche de cette thèse est l'étude de l'effet des corrélations électroniques sur les propriétés de transport dans des couches minces de LaTiO_{3+ δ}. LaTiO_{3+ δ} (LTO) est un composé qui a été intensivement étudié pour sa transition d'un état métallique à un isolant de Mott. En fait, en changant le dopage, les propriétés électroniques évoluent d'un isolant de Mott (Ti³⁺) à un isolant de bande (Ti⁴⁺) en passant par une région métallique intérmédiaire. L'idée est d'étudier la physique de cette région métallique pour indiquer le type de corrélations qui conduisent à l'état isolant du système.

Dans cette thèse nous avons profité d'une collaboration existant entre le laboratoire de recherches d'IBM Zürich et les Universités de Neuchâtel et Genève. Le laboratoire d'IBM est en effet spécialisé dans la croissance épitaxiale de couches minces de haute qualité. Ces couches sont préparées dans un système de dépôt par épitaxie par jets moléculaire, système développé à IBM. Les Université de Neuchâtel et de Genève sont quant à elles spécialisées dans la caractérisation physique des supraconducteurs et de façon plus générale des systèmes d'oxydes à forte corrélation. Cette collaboration nous a permis d'étudier des échantillons de très haute qualité avec un grand contrôle sur la composition, ce qui nous a permis de réduire l'importance des défauts, et d'accéder ainsi aux propriétés intrinsèques des matériaux.

Les couches minces épitaxiales de LTO ont été préparées en utilisant une méthode

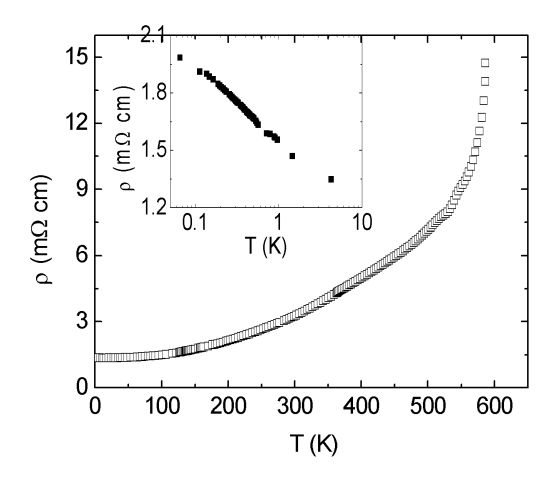


Figure R.6: Résistivité d'une couche mince de LTO en fonction de la température. L'augmentation rapide de la résistivité aux températures élevées ainsi qu'une irreversibilité observée dans le comportement de la résistivité en dessus de 550 K suggèrent un changement de composition et/ou de structure du film à cette température. Encart: résistivité à très basses températures démontrant un état fondamental isolant.

séquentielle de dépôt. Le lanthane (La) et le titane (Ti) ont été évaporés à l'aide d'un faisceau d'électrons (e^- -beam) et ont été déposés sur différents substrats sous forme de séquences d'une monocouche de La- O_x suivie d'une monocouche de Ti- O_x . Une haute pression d'oxygène dans la chambre de dépôt de l'ordre de 10^{-6} Torr favorise la croissance du LaTiO_{3.5} ferroélectrique. Pour faire croître des couches de LTO métalliques avec un contenu en oxygène inférieur, nous avons ramené la pression de l'oxygène dans la chambre à 10⁻⁷ Torr. Les couches minces ont été déposées sur des substrats de LaAlO₃ orientés (001). Nous avons étudiés en détails les propriétés de transport de ces couches à l'aide de pistes de résistivité et d'effet Hall préparées par un processus lithographique. Pour mesurer le dopage des films nous avons mesuré l'effet Hall en fonction de la température pour obtenir la densité de porteurs. L'étude de Tokura et al. [4] a démontré que la densité de porteurs peut être reliée au dopage et donc à la valence du Ti. La constante de Hall, R_H , est essentiellement indépendante de la température entre 50 K et 300 K. La densité de porteurs n calculée à partir de $R_H^{-1}=ne$, où e la charge de l'électron, est typiquement comprise entre 5 et 12·10²¹ électrons par centimètre cube, correspondant à une valence du Ti entre l'isolant de bande et l'isolant de Mott [$x^*=0.3-0.7$ avec x^* , paramètre de la valence defini comme $x^*=Ti^{3+}/(Ti^{3+}+Ti^{4+})$].

La figure R.6 montre la résistivité ρ en fonction de la température entre 4 K et 600 K pour une couche mince (25 nm) de LTO, avec une concentration de porteurs de $1.2 \cdot 10^{22}$ cm⁻³. A basse température, une transition métal-isolant est systématiquement observée au-dessous d'une température caractéristique. La recherche de la supraconductivité dans les oxydes de Ti a été le sujet d'une intense recherche. Sur nos échantillons les plus métalliques nous avons effectué des mesures de résistivité dans un cryostat à dilution jusqu'à

xvi Résumé

15 mK, aucune superconductivité n'a cependant été observée. Au contraire, la résistivité augmente lorsque l'on réduit la température, suggérant un état fondamental isolant. A plus haute température, la resistivité a un comportement métallique et une dépendance qui va approximativement comme le carré de la température jusqu'à 500 K. La brusque augmentation du comportement de la résistivité avec la température est probablement dû à un changement de la composition ou de la structure de la couche.

Le comportement résistif observé dans la figure R.6 peut être analysé dans le cadre d'un mécanisme de transport polaronique. La résistivité dans le régime métallique prend alors la forme suivante [5]:

$$\rho(T) = \rho_o + C/\sinh^2(\hbar\omega_o/2k_B T) \tag{R.2}$$

où ρ_o est la resistivité résiduelle, C une constante de couplage électron-phonon et ω_o la fréquence du phonon couplé à la charge. La figure R.7 montre la résistivité en fonction

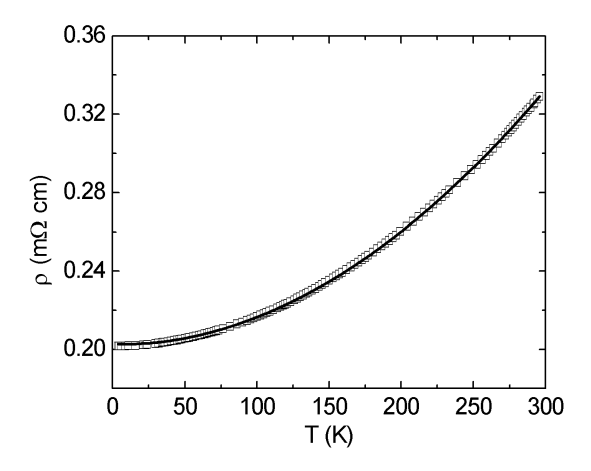


Figure R.7: Résistivité d'une couche mince de LTO en fonction de la température. La ligne continue est un fit de la résistivité à un mécanisme de conduction polaronique.

de la température entre 4 K et 300 K et le fit pour le transport polaronique obtenu de l'équation R.2. Comme on peut le voir sur la figure, celui-ci est excellent avec ρ_o =0.20 m Ω cm, C=2.3 $\mu\Omega$ cm, et $\hbar\omega_o/k_B$ =80 K. La fréquence phononique obtenue à partir du fit peut être comparée aux mesures de spectres des phonons réalisés sur ce composé par spectroscopie Raman. Ces mesures [6] donnent une évidence claire de l'existence d'un mode phononique à une énergie d'environ 100 K, ce qui renforce sensiblement notre interprétation des données résistives. Ce mode phononique semble être caractéristique d'une rotation des octaèdres de l'oxygène et est présente dans différents matériaux de structure perovskite. L'analyse des propriétés de transport semble indiquer que la conduction dans ce matériel a une nature polaronique et nous permet de proposer un scénario réconciliant ces mesures de transport avec des données de photoémission obtenues sur

ce composé [7]. L'ensemble des données de l'état métallique du LTO dans la gamme de composition étudiée, suggère que la physique dans ce système est dominée par des interactions électron-phonon.

The conventional theory of solids, based on the quantum mechanics of single electrons moving in periodic potentials, provides an excellent description of substances ranging from semiconducting silicon to superconducting aluminium. Over the last fifty years and in particular during the last fifteen years, it has, however, become increasingly clear that there are substances for which the conventional approach fails. Among these are certain transition metal oxides, including high-temperature superconductors and manganites. The common feature of these compounds is their relatively low carrier density which falls between that of semiconductors with carrier densities ranging from 10^{14} to 10^{18} charges/cm³ and metals with densities of $\sim 10^{22}$ charges/cm³. A consequence of this relatively low carrier density is that the carriers are less heavily screened than in ordinary metals, increasing the electronic correlations (for instance, the Coulomb repulsion between them). In semiconductors, charge carriers are far apart and consequently semiconductor theories disregard any correlation effect. In metals, Landau's theory provides a unification of the theories of neutral and charged uniform Fermi systems: the influence of Coulomb interaction leads to a quantitative renormalization of the quasiparticles (the excitations of the interacting system), but those are in a 1-to-1 correspondence with the excitations of noninteracting fermions.

The electronic properties of these "novel" materials turn out to be strongly affected by the electronic interactions, resulting in unique behaviors observed as the temperature is changed or as a magnetic field is applied. Often, these new materials also display complex phase diagrams as a function of the doping level (the number of carriers in the system). This complexity is both challenging as many of the new phenomena are still not understood, and appealing, due to the potential applications of these extraordinary properties. These exciting possibilities have significantly boosted research in transition metal oxides in the last fifteen years. Among the important challenges, one will also have to address some fundamental weaknesses of these novel materials which may ultimately undermine their technological usefulness. For instance, it is found in many compounds of interest that the carriers are often sharply localized in planes or chains, lowering the dimensionality of the systems and sometimes resulting in extremely anisotropic properties. In high temperature superconductors, another difficulty is the extremely short coherence lengths, typically a few unit cells. This makes the materials very sensitive to defects such as impurities, grain boundaries and interfaces, and may promote phase separation at the nano-

metric scale.

There are different routes that enable exploration of the electronic properties and intriguing phase diagrams of these materials. In this thesis we will explore one of these possibilities: the ferroelectric field effect.

Main goal of the Thesis

This thesis has developed along two main lines with a common goal: the study of the effect of electronic correlations on transport properties.

A collaboration between the IBM Zürich Research Laboratory and the Universities of Neuchatel and Geneva was established in 1995 to combine the high-quality control of epitaxial thin film growth, possible with a molecular beam epitaxy system developed at IBM, and the Neuchatel and Geneva expertise in the physical characterization of superconductors and more generally correlated oxide systems. This approach, allowing the study of the highest quality samples with finely tuned composition, will help reduce the importance of defects, to access intrinsic material properties. In the first part of this thesis, we have investigated LaTiO_{3+ δ} (LTO), a strongly correlated electron oxide. LTO is a compound that has been extensively studied for its metal-Mott insulator transition. In fact, as the doping level is changed, the electronic properties evolve from a Mott insulator (Ti³⁺) to a band insulator (Ti⁴⁺) with a metallic region in between. The idea was to study the physics of this metallic region to reveal the type of correlations that drive the system insulating. The growth of this material has proven challenging and we have established a phase diagram for the growth conditions under different epitaxial constrains. In studying its physical (transport) properties we tried to clarify whether electron-electron interactions or electron-phonon interactions can be regarded as the dominant correlations in the material. We also tried to connect the transport properties of films grown on different substrates with a study of structural properties performed by transmission electron microscopy by Dr. M. Seo. Our results suggest that different epitaxial constrains promote different oxidation mechanisms in LTO thin films, resulting in a different crystallization and very different transport properties.

The second topic of my thesis takes advantage of the expertise of the group to address the question of correlation effects in cuprate superconductors using a powerful and clean technique: the field effect. This technique, based on high-quality ferroelectric/superconductor heterostructures, uses the non-volatile ferroelectric polarization to electrostatically tune the doping level of ultrathin superconducting layers. Since in high temperature superconductors the electronic properties are particularly sensitive to the carrier concentration, this results in a modulation of the superconducting and normal state properties. The polarization of $Pb(Zr_{0.2}Ti_{0.8})O_3$, our choice as ferroelectric material, is very large and can, in principle, deplete a one-unit-cell thick high T_c layer completely, thus suppressing superconductivity. We have used the ferroelectric field effect to modulate the superconducting properties of ultrathin high T_c superconducting layers, achieving reversible shifts of T_c and inducing a transition from a superconducting behavior to an insulating one. We also

took advantage of the well defined induced charge to study the transport properties in the normal state, in particular the Hall effect, which displays a particularly complex response in cuprate superconductors.

Outline of the Thesis

Chapter 1 presents a theoretical introduction to the field of correlated materials with a detailed analysis of the Hubbard model. It also describes the structure and phase diagram of the electronic properties of the materials under investigation, LTO and $REBa_2Cu_3O_7$, RE=Nd or Gd, later referred to as Y123.

Chapter 2 introduces the experimental techniques used in this work and describes the various parameters controlling the growth process and the information obtainable from the characterization measurements.

Chapters 3 and 4 contain the results of this study. Chapter 3, after some introductory sections on high- T_c theories and the ferroelectric field effect technique, deals with the field effect in superconductors, presenting the modulation of their transport properties. Our understanding of these results is compared with existing theories. In chapter 4 we return to theories of the metallic phases close to a Mott insulator and after the description of LTO epitaxial thin film growth, we summarize the structural and transport measurements and our understanding of the results.

Chapter 1

Electron correlations in solids

1.1 Metal-insulator transition

Three years after Thomson discovered the electron, Drude (1900) [8,9] constructed his theory of electrical and thermal conduction by applying the highly successful kinetic theory of gases to a metal, considered as a gas of electrons. In his theory, Drude described the electrons as particles wandering around fixed ions with no forces acting between them, except during collisions. This first theory, although successfully describing the transport properties of metals, could not explain the origin of the metallic state. The basic distinction between metals and insulators was proposed and established in the early years (1928-1929) of quantum mechanics (Bethe, Bloch, Sommerfeld) [10, 11, 12]. The distinction was stated as follows: in crystalline materials the energies of the electron states lie in bands: an insulator is a material in which all bands are either full or empty, while in a metal one or more bands are only partially full. In other words, the Fermi level lies in a band gap in insulators and inside a band for metals. In the non-interacting electron theory, the formation of band structure is totally due to the periodic lattice structure of atoms in crystals. By the early 1930s, it was recognized that insulators with a small energy gap would be semiconductors due to thermal excitation of the electrons [13, 14]. Although this band picture was successful in many aspects, experimental reports observed that different transition-metal oxides with a partially filled d-electron band were nonetheless poor conductors and indeed often insulators. Peierls (1937) pointed out the importance of the electron-electron correlation: strong Coulomb repulsion between electrons could be the origin of insulating behavior. His observations launched the long and continuing history of the field of strongly correlated electrons, where a particular effort is made to understand how partially filled bands can result in insulators. The transition from an insulator to a metal, driven by tunable parameters, as illustrated in figure 1.4, is called the *metal*insulator transition (MIT).

1.2 Mott insulator

Among the theoretical approaches, Mott (1949) [15, 16] took the first important step towards understanding how electron-electron correlations could explain the insulating state, later called a *Mott insulator*. He considered a model of a lattice with a single electronic orbital on each site. Without electron-electron interactions, a single band would be formed in this system from the overlap of the atomic orbitals, where the band becomes fully occupied when two electrons, one with spin-up and the other with spin-down, sit on each site. However, two electrons occupying the same site would feel a large Coulomb repulsion, which Mott argued would split the band in two: a lower band, corresponding to singly-occupied sites and an upper band formed from sites occupied by two electrons. With one electron per site, the lower band would be full and the system an insulator.

In contrast to Mott, Slater (1951) [17] ascribed the origin of the insulating behavior to antiferromagnetic long-range order. In Slater's picture, the insulator may arise due to a band gap generated by a superlattice structure of the magnetic periodicity. Although most Mott insulators have magnetic ordering at least at zero temperature, there are several examples of Mott insulators without magnetic ordering. Since the proposals by Mott and Slater, these two viewpoints have played complementary roles in understanding insulators resulting from correlation effects.

1.3 Hubbard model

A prototype model for the theoretical description of the Mott insulator is the *Hubbard model* [18, 19, 20, 21]. This model considers only one atomic orbital per lattice site. The nearest-neighbor Hubbard Hamiltonian is given by

where $c^{\dagger}_{i\sigma}(c_{i\sigma})$ denotes the creation (annihilation) of an electron with spin σ at site i and $n_{i\sigma} \equiv c^{\dagger}_{i\sigma}c_{i\sigma}$ is the number operator. H_t is the kinetic-energy operator (t is the hopping integral between two adjacent sites) and the on-site term H_U describes the Coulomb repulsion of two electrons at the same site (U>0 is the on-site Coulomb repulsion energy). Because it includes both overlap and Coulomb repulsion terms, the Hubbard model spans the range from independent-electron band theory to the fully localized Mott insulator. If U=0, the first term leads simply to the usual tight-binding band of width $W\sim 2zt$, where z is the number of neighbors in the lattice. For $U\gg t$ and a density of one electron per site, the ground state is an antiferromagnet with localized magnetic moments. An exchange coupling $J=4t^2/U$ acts between neighboring spins.

Does the Hubbard model which considers only a single orbital apply in the situation of

1.3. Hubbard model 7

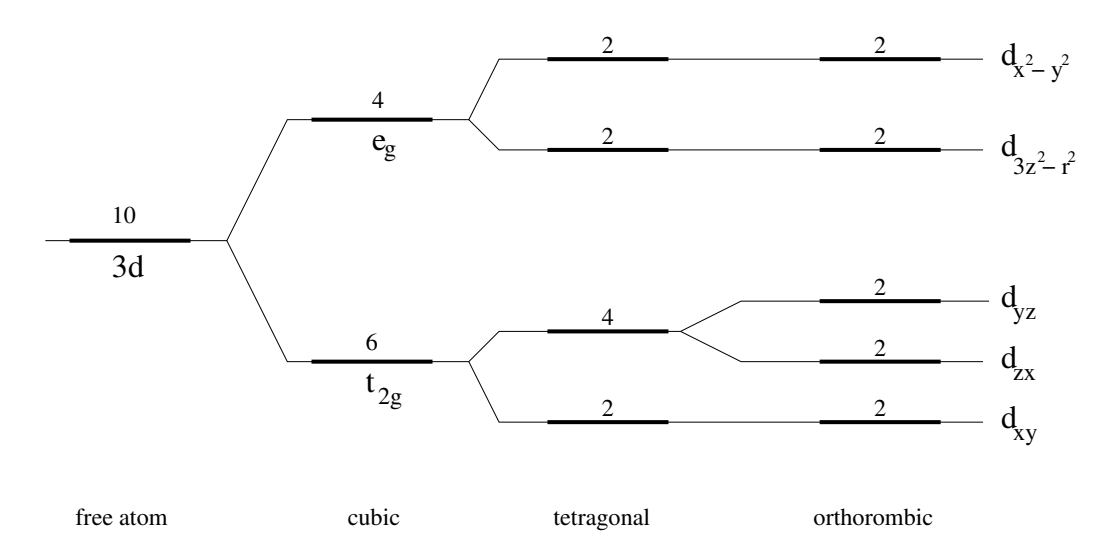


Figure 1.1: Crystal-field splitting of 3d orbitals under cubic, tetragonal and orthorhombic symmetries. The level degeneracy (including spins) is indicated.

transition-element compounds? In solids, bands are formed from the overlap of atomic orbitals arranged in a periodic configuration. In transition-metal systems, the overlap comes from two d-orbitals on two adjacent transition metal atoms. Because d-wave functions have a small radius compared to the crystal lattice constant, d-electron systems have, in general, small overlap and hence small bandwidths. In solids, the bands are under the strong influence of anisotropic crystal fields. The effect of the crystal fields is to lift the orbital degeneracy of the d-electrons, as shown in figure 1.1. The orbital degeneracy in transition-metal compounds plays a major role because it produces a rich structure of low-energy excitations through orbital fluctuations and orbital orderings. The orbital degeneracy can also be lifted by several on-site mechanisms, including the spin-orbit interaction and the Jahn-Teller distortion. In the case of spin-orbit interaction, splitting of orbital levels is usually accompanied by simultaneous breaking of spin symmetry. For example, if the spins order along the z axis, then the LS interaction (spin-orbit interaction) λ **LS** immediately stabilizes the orbital with the z component of the angular momentum $L_z \neq 0$. When a finite L_z state is chosen, it may also induce lattice distortion. In fact, if the electrons occupy states such as yz or zx orbitals, a Jahn-Teller distortion occurs in such a way that the octahedron elongates in the z direction. The Jahn-Teller distortion can by itself play an important role as a driving force to remove the degeneracy. The Jahn-Teller theorem asserts that it is energetically favorable for the crystal to distort in such a way as to lower the symmetry of the ground-state enough to remove the degeneracy. This occurs because the energy gain due to this splitting of the degeneracy, which is linear in the distortion, always wins in comparison with the cost of energy due to the lattice elastic energy, which is quadratic in the distortion. Various types of Jahn-Teller distortions may be realized in perovskite structures. The magnitude of this lifting of degeneracy compared to the thermal energy determines if the Jahn-Teller effect will be observable.

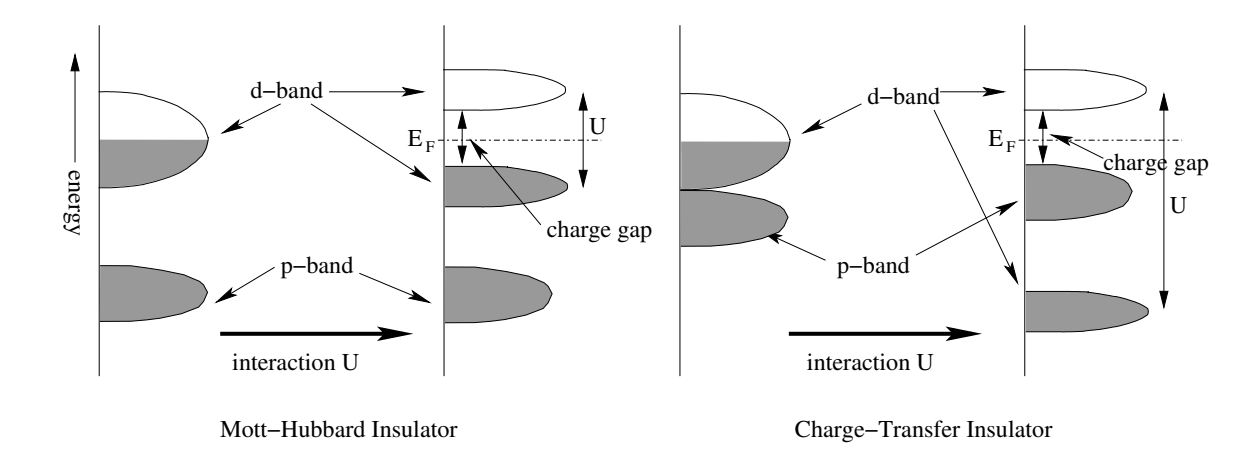


Figure 1.2: Schematic illustration of energy levels for a Mott-Hubbard insulator and a charge-transfer insulator.

In the case of transition metal oxides, the overlap is often determined by indirect transfer between d-orbitals through ligand p-orbitals: the p-orbital makes a bridge between two transition-metal atoms, hybridizing the d-wave functions. The strength of this hybridization becomes stronger moving from light transition-metal elements (Ti, V, Cr) to heavy transition-metal elements (Cu and Ni). This dependence is due to the oxygen 2p level that moves closer to the level of the partially filled 3d band for heavier transition-metal elements.

For transition-metal compounds the model of a single d-band is correct when the charge excitation gap is formed between the lower Hubbard band (LHB) with single occupancy of the atomic sites and the upper Hubbard band (UHB) separated from the former by a Mott gap of order U. However, when the p level is closer to the d half filled band (or the Fermi level), the charge excitation gap extends between a fully occupied p-band and the UHB. Since the excitation is a p hole and a d electron this kind of insulator is called a charge-transfer (CT) insulator to be distinguished from the Mott-Hubbard (MH) insulator, the former case. This distinction was clarified by Zaanen, Sawatzky and Allen [22] and it is schematically illustrated in figure 1.2. Following this distinction for Mott insulators, titanates, vanadates and chromates fall in the MH family where both holes and electrons move in d bands and are heavy, while cuprates and nickelates belong to the CT type where holes in p band are light and electrons in d band are heavy.

1.4 Slater's theory of Mott insulators

Slater was the first to suggest that the insulating properties of magnetic and antiferromagnetic transition-metal compounds could be explained by supposing that the band was split by the magnetic/antiferromagnetic interaction [17].

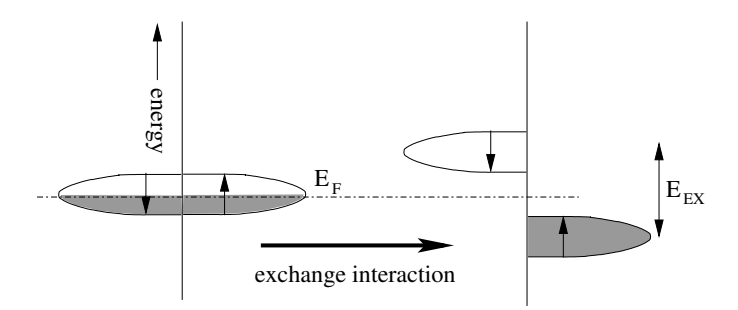


Figure 1.3: In a molecular-field model the spin-up \uparrow and spin-down \downarrow states in one of the bands are considered separately. The exchange interaction causes the two halves of the band to be relatively displaced along the energy axis, eventually opening a gap.

In the model put forward by Stoner and by Slater [23], in order to take account of the influence of exchange energy in ferromagnetic metals the states of 'upward' spin are considered separately from those of 'downward' spin. Each band is therefore treated as two half-bands, one comprised of the states with upward spins and the other of those with downward spins: in the nonmagnetic state they will be similar. The exchange interactions cause the two halves of the band to be displaced along the energy axis relative to each other. In fact, when electrons are transferred one by one from downward to upward states, the exchange energy decreases as the number of parallel electrons increases. This exchange energy can be included in the density-of-states curves by displacing all the states of upward spin downwards on the energy axis and all the states of downward spin upwards on the axis.

The exchange energy density is expressed by

$$E_{EX} = -\frac{1}{2}\gamma n^2 \mu_B^2 \tag{1.2}$$

where γ is the molecular field constant, n is the difference of electrons per unit volume between the two spin orientations and μ_B is the Bohr magneton.

If the exchange forces are intense, and the half-bands narrow, the latter might be shifted with respect to each other to the extent that an energy gap appears, as illustrated in figure 1.3. A half-filled band system with magnetic ordering may then be insulating.

Antiferromagnetic ordering can also be treated within this model, by dividing the crystal lattice into two equivalent and interpenetrating sublattices and then introducing two molecular field constants. Lidiard's theory for antiferromagnetic ordering then follows Stoner's for the magnetic one.

1.5 MIT phase diagram

The two important parameters in the Hubbard model are the electron correlation ratio U/t and the band filling n, as depicted in the MIT phase diagram in figure 1.4. In the case of

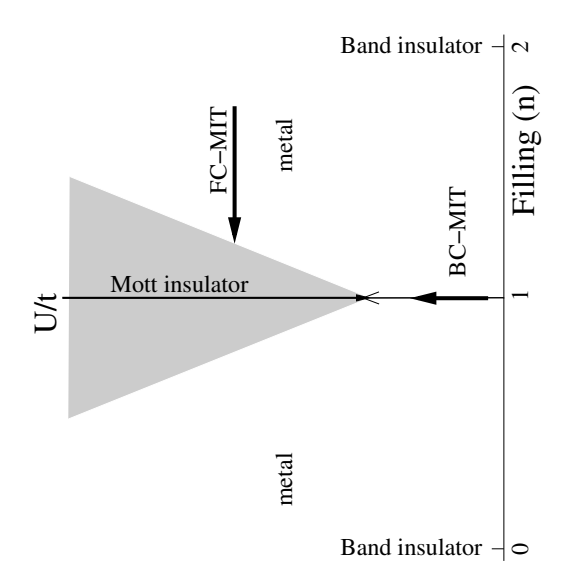


Figure 1.4: Metal-insulator phase diagram in the plane of U/t and filling n at T=0 K. The shaded area is under the strong correlations that drive the system to MIT: in this region carriers are easily localized by extrinsic forces. The FC-MIT and the BC-MIT routes for MIT are shown.

a non-degenerate band, for fillings n=0 and n=2, the material is a band insulator. For the case n=1 (half filling), it is the strength of U/t that determines the electronic nature of the material.

By controlling experimental parameters it is possible to move along the two axes of the phase diagram to induce the MIT. For half-filling and finite U, it is possible to vary the hopping energy t of the conducting particles by changing the electron bandwidth W ($t \sim W/2z$ where z is the coordination number). This transition, called bandwidth control (BC)-MIT, is obtained by applying external or internal (chemical) pressure. Otherwise, moving away from half-filling (n=1) usually leads to the metallic state. This filling control (FC)-MIT is obtained by doping the parent Mott insulator by modifying the chemical composition, introducing extra oxygen or its vacancies. We finally note that in a large U/t region near the insulating phases n=0,1,2 the compounds can suffer from the carrier localization effect arising from the static random potential and electron-lattice interactions.

1.6 Polarons

We have seen the effect of the interaction between electrons on inducing magnetic moments and MITs. In a solid the electrons also interact with the lattice vibrations. Interaction with phonons plays an important role, particularly in some transition-metal oxides. The phonons in a solid conductor have different effects on mobile electrons or holes. Besides the exchange of energy in inelastic collisions where a phonon is absorbed or gen-

erated by a charge carrier, thus being responsible for an important part of the electrical resistivity, phonons can interact with electrons or holes in a narrow-band material forming polarons or bipolarons. The charge carrier polarizes and thereby distorts the ion lattice in its neighborhood; the polarization, in turn, acts on the charge carrier and lowers its energy. As the carrier moves through the crystal, it takes along the distortion of the lattice. The carrier, together with its accompanying polarization, can be thought of as a quasiparticle with effective mass larger than that of a Bloch charge carrier; this quasiparticle is called polaron. Polaron formation is caused by the dynamic electron-lattice interaction. The size of the polaron is measured by the extension of the lattice distortion induced by the excess electron. For a large polaron, the lattice distortion is much larger than the lattice constant; for a small polaron, it is restricted to the vicinity of the electron over a volume comparable with or smaller than the volume per atomic site. A detailed description of polaron formation and their contribution to the physical properties is given in [24, 16]. In chapter 3 we will see the concept of polarons linked to high-temperature superconductivity and in chapter 4 we will present the mobility properties of polarons in a metal and discuss the applicability of this model to the metallic phase of LTO.

1.7 Anomalous metallic phases

A theoretically and experimentally challenging subject is the metallic phase near the Mott insulator. Close to the MIT, fluctuations and ordering in the spin, charge and orbital degrees of freedom show up in the metallic state: colossal magneto-resistance in manganites and charge-ordering phases in nickelates are some spectacular examples; superconductivity in cuprates, exceptional for its highest T_c values, is still unexplained, with a lack of consensus on its microscopic origin. Established single-particle theories fail to describe these anomalous metallic phases. Fermi-liquid theory, successful for normal metals, breaks down in the face of strong correlation effects: the normal state of cuprate superconductors, for example, shows many unusual properties which are far from the standard Fermi-liquid behavior. New theoretical approaches have been developed in order to explain these novel electronic properties and in the following chapters we will present the ones pertinent to this study. The perovskites, being very suitable for FC-MIT, exhibit these extraordinary electronic properties and are the principal materials under investigation.

1.8 High- T_c superconductors

The work by Bednorz and Müller on the FC-MIT in perovskites and related structures, followed by the discovery of a new family of superconductors in the 1986 [1], opened the era of high- T_c superconductivity, changing the history of a phenomenon that had previously been confined to very low temperatures. This result prompted intense activity in the

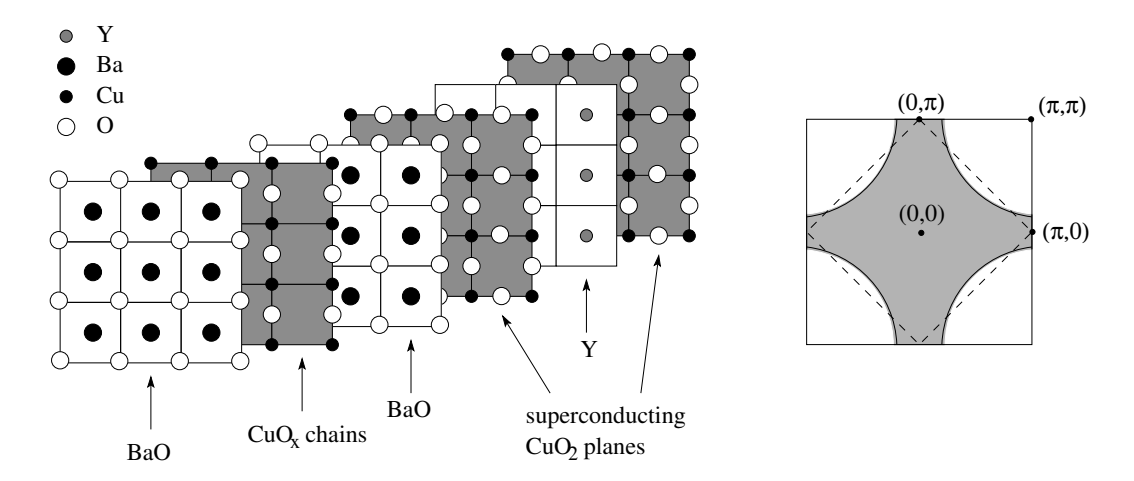


Figure 1.5: Left: Stacking of planes in YBCO: the planes are stacked along the *c*-axis. Note the Cu-O chains in the interleaving plane. Right: 2D projection of the Brillouin zone with the Fermi surface (gray area) and the magnetic Brillouin zone boundary (dashed line).

field of transition metal oxides with a perovskite structure due, both to the fundamental interest of obtaining solid solutions with filling (n) varied continuously in an extended region close to the critical n=1 value (Mott insulator) and to the technological promise of anomalous metallic phases for novel applications.

1.8.1 Crystal and electronic structure

The cuprate superconductors [25] have a layered perovskite structure with a stacking sequence of CuO₂ planes which form single (LSCO) or multi-layer (YBCO) blocks separated from each other by the so called *charge reservoir* layers. An additional complexity of YBCO compounds is that it has a chain structure of Cu and O embedded in the charge reservoir block, as shown in figure 1.5. However this Cu-O chain structure makes only a minor contribution to the dc conductivity. Because of the anisotropic lattice structure, the cuprates have a quasi 2D electronic structure. By substituting different elements in the reservoir layers or by varying their oxygen content, one can dope charge carriers into the CuO₂ planes. The latter are believed to be responsible for the high-temperature superconductivity as the Cu-O bands are the lowest energy electronic states and therefore directly determine the macroscopic electronic properties. The parent compounds (YBa₂Cu₃O₆ in our case) are antiferromagnetic insulators. These systems, with an odd number of electrons per unit cell, belong to the class of Mott insulators with a partially filled d-band. In these compounds, the Cu-O charge-transfer energy Δ (1-3 eV) is smaller than the on-site Coulomb repulsion U (6-10 eV) which characterizes the cuprates as charge-transfer insulators. The 2D projection of the Fermi surface, shown in figure 1.5, initially obtained from band structure calculations, has been confirmed by photoemission experiments in a variety of cuprate superconductors.

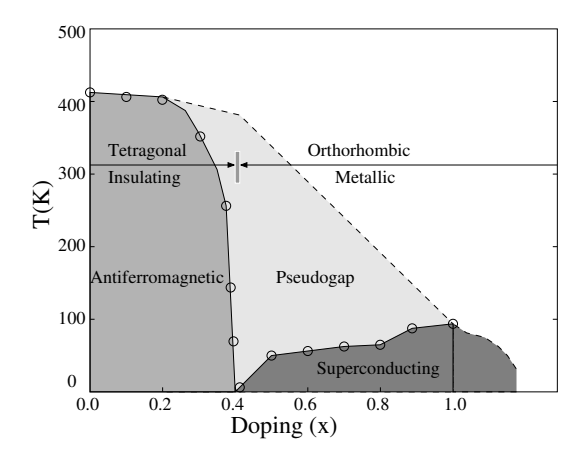


Figure 1.6: Temperature-doping phase diagram of electronic properties for $YBa_2Cu_3O_{6+x}$ (after [26]).

1.8.2 Phase diagram

Insulating YBa₂Cu₃O_x with $x \le 0.4$ has a tetragonal structure and displays antiferromagnetic long-range order ($T_N \sim 400$ K). In the region 0 < x < 0.4, holes are doped mainly into the CuO chain sites, with negligible effect on the doping concentration of the CuO₂ planes. Just below x = 0.4 holes start being transferred to the CuO₂ planes, which destroys the antiferromagnetic ordering. Around x = 0.4, the compound undergoes a structural transition, becoming orthorhombic, and an electronic transition to a metallic state. Superconductivity appears, and T_c then rises as the hole concentration in the CuO₂ layer increases further, maximizing at ~ 90 K for about 0.15 hole per unit cell, then falling again to zero. The very slight tetragonal-orthorhombic lattice transition appears to have little interaction with the superconductivity and appears at different points in the doping phase diagram for different rare-earth doping.

Short-range antiferromagnetic correlations survive in the metallic state. However, magnetic properties show rather different features between the underdoped and the optimally doped or overdoped samples. These observations (1991) [27] were the first pioneering indications of a normal-state excitation gap, called pseudogap, in the high- T_c cuprates well above T_c . A variety of successive experimental measurements has clarified the nature of this excitation gap and a pseudogap line has been traced in the phase diagram [28].

Still lacking a definitive theory that, like the Bardeen-Cooper-Schrieffer theory, describes the microscopic origin of the interaction that binds electrons into pairs, we will present in chapter 3 two different theories of the cuprate superconductors relevant to this study.

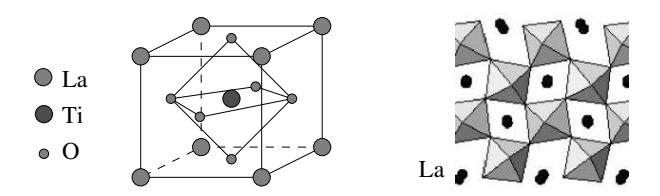


Figure 1.7: Cubic perovskite structure and GdFeO₃-type tilting distortion of MO₆ octahedron.

1.9 LaTiO₃: structure and phase diagram

LaTiO₃ is a d^1 compound barely in the insulating region of the Mott insulator phase diagram ($U/W \sim 1$) and belongs to the Mott-Hubbard insulator family. It has an orthorhombic structure with $a \simeq b = \sqrt{2a_0}$ and $c = 2a_0$ where a_0 is the lattice parameter of the unit cubic perovskite (a = 0.562 nm, b = 0.560 nm, c = 0.791 nm). This is due to a GdFeO₃-type distortion of the arrangement of the oxygen octahedra, as shown in figure 1.7. Stoichiometric LaTiO₃ is an antiferromagnetic insulator with a Néel temperature of approximately 150 K: the canting of the adjacent spins results in a small ferromagnetic moment observed in magnetization measurements. With a charge gap of 0.2 eV, this compound is just barely insulating: a slight deviation in the stoichiometry induces a metal-insulator transition. Doping by vacancies in the La site, excess of oxygen or chemical substitution of divalent atoms (Sr or Ba) onto the trivalent La site are all routes being used to explore the phase diagram of LTO. As the d band filling is varied, the electronic structure evolves from a Mott insulator (Ti³⁺) to a band insulator (Ti⁴⁺). Figure 1.8 shows the phase diagram obtained by Tokura with Sr doping and the one obtained by Bednorz with O doping. Close to the Mott insulator region, the two diagrams look similar: a small amount of doping suppresses the long-range G-type antiferromagnetic ordering with a rapid fall of T_N and turns the system metallic. A large part of chapter 4 is devoted to the nature of this metallic phase. For higher doping, $La_{1-x}Sr_xTiO_3$ (LSTO) and LaTiO_{3+ δ} behave differently. LSTO evolves continuously towards the band insulator STO, suppressing the orthorhombic distortion, and the metallic character persists up to the composition x = 0.98. The O doping phase diagram instead displays a structural transition at $\delta = 0.4$ from the 3D orthorhombic distorted perovskite structure to a 2D layered-type. This transition reveals a new family of phases $La_{n+1}Ti_{n+1}O_{3n+5}$. The observed phases (n=3 and n=4) have a layered structures with two blocks of n+1perovskite unit cells separated by an additional oxygen plane. For $\delta \sim 0.3$ the system becomes semiconducting and for $\delta = 0.5$ the band insulator is a ferroelectric material.

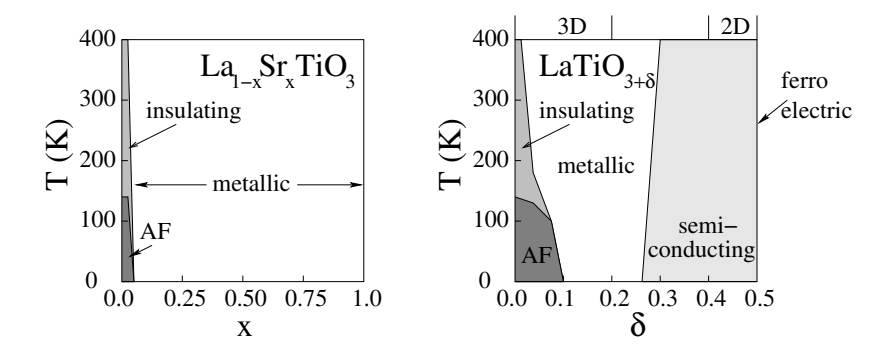


Figure 1.8: Temperature-doping phase diagram for electronic properties and structure of $La_{1-x}Sr_xTiO_3$ from Tokura (left) [4] and $LaTiO_{3+\delta}$ from Bednorz (right) [29].

Chapter 2

Experimental set-up

Introduction

The preparation (growth, characterization and patterning) of thin films and heterostructures for physical measurements is an important and difficult task that could by itself constitute a full thesis. Transition-metal oxides are particularly sensitive to defects such as grain boundaries, interfaces, inhomogeneities and vacancies: materials scientists are currently working on these topics to improve the quality of these materials to access their fundamental and intrinsic properties and to prepare for future technological applications. In this thesis we prepared oxide thin films and heterostructures taking advantage of the local knowledge of thin film growth [30, 31, 32, 33] and characterization. This chapter summarizes the deposition processes and the characterization techniques used.

2.1 Thin film deposition

Oxide thin film growth can be achieved by a large variety of deposition techniques, which have been developed over many years. To prepare epitaxial thin films, the desired materials are in general vaporized and transported to the substrate where deposition takes place. Solid materials can be vaporized by thermal evaporation produced, for instance, by an energetic beam of electrons, or photons (laser ablation) or extracted through a gas bombardment (sputtering). These methods are categorized as *physical* vapor deposition (PVD). Alternatively, solid sources can be *chemically* converted to vapors or supplied as a gas or as a liquid (CVD). Among the different PVD techniques used for the growth of epitaxial films, one can identify essentially two kinds of methods. The first kind (laser ablation and sputtering) uses as the material source a target of a given stoichiometry to produce a film with more or less the same composition. The second kind (molecular beam epitaxy) combines the fluxes of separate elements, generated by different heated sources,

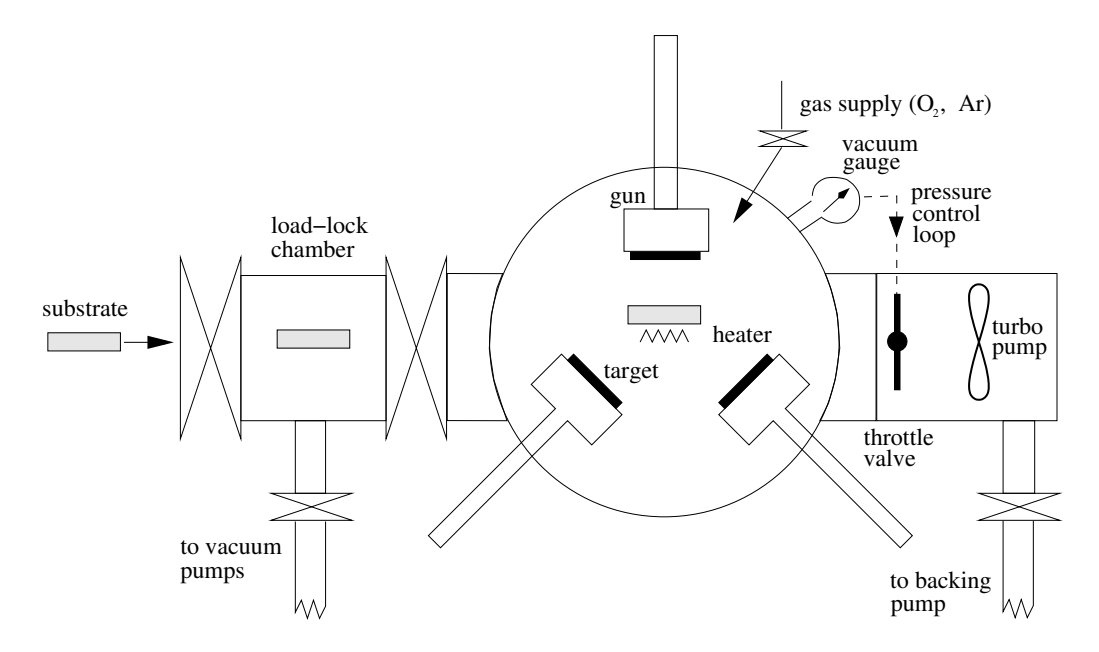


Figure 2.1: Schematic view of the home-made deposition chamber for the growth of sputtered thin layers.

in sequential or co-deposition to form a compound with the desired stoichiometry. A complete description of the different thin film deposition processes and techniques can be found in [34,35].

2.1.1 Sputtering

The thin films and heterostructures for the field effect studies were grown using a home-made sputtering system at the DPMC. Figure 2.1 shows a schematic drawing of our deposition system.

In the sputtering deposition, ion-bombardment erodes a solid target, volatilizing the compound. The sputtered atoms diffuse in the gas and condense on a heated substrate leading to the formation of a thin layer. Ions are generated in a glow-discharge plasma and are accelerated out of the plasma into the target by applying a voltage bias to the target; if the target is insulating, rf power is used to obtain the desired bias. Confinement of the plasma near the target is improved by the magnetic field of the "magnetron" sputter source, as shown in fig. 2.2, resulting in an enhancement of the sputtering rate. In oxide thin film growth, the inert-gas (Ar) used as a source for the plasma is mixed with oxygen and *insitu* post-deposition oxygen annealings can be further used to fully oxidize, for instance, superconducting layers.

The chamber is designed with the heater in the center and with three sputtering guns that, moved sequentially into the deposition position, allow the growth of heterostructures. The substrate is positioned at 90° to the target (off-axis configuration) with the substrate

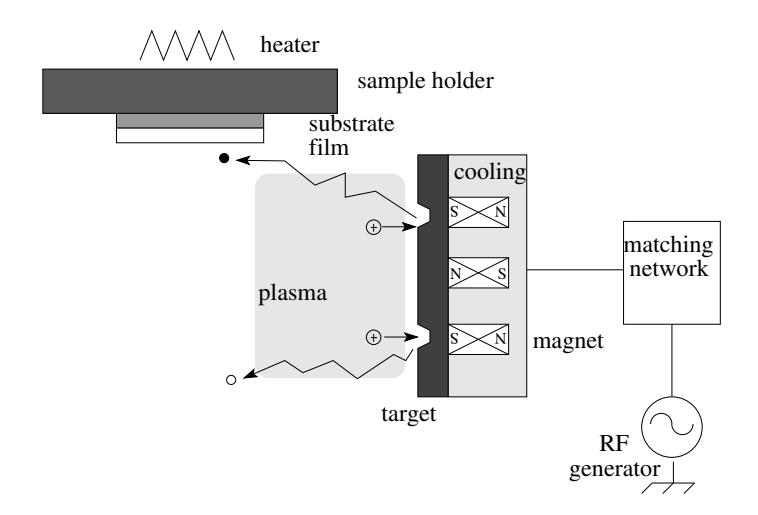


Figure 2.2: Sputtering process with the magnetron gun structure in the *off-axis* configuration.

surface pointing downwards, minimizing the possibility of small particles falling onto the substrate [36, 37]. The substrate temperature is measured with a pyrometer, a technique that in spite of suffering from the change in emissivity of the film surface, is found to be sufficiently reliable and sensitive.

2.1.2 Molecular Beam Epitaxy

The LTO samples were grown using a custom-made MBE (RIBER ISA) illustrated in Fig. 2.3, at the IBM Zürich Research Laboratory in Rüschlikon. In an ultrahigh vacuum chamber (base pressure 10^{-9} Torr), molecular oxygen is introduced in order to deposit oxide thin films in a background oxygen pressure. Electron-beam gun evaporators were used for our materials, La and Ti. In order to ensure good film deposition and to reduce flux transients, the electron beams were de-focused and swept over the entire surface of the crucibles. A sequential deposition process was used, whereby the molecular beam flux was controlled by the main quadrupole mass spectrometer, which was previously calibrated using a quartz monitor inserted in the substrate deposition location. Two other mass spectrometers were placed above the La and Ti evaporation sources to control and regulate their beam flux using a PID feedback loop. Before proceeding to the growth, a calibration procedure, completely described in Ref. [38] was run. This calibration procedure takes about 4 hours. The substrate growth temperature was monitored by a pyrometer and a very slow evaporation rate of ≈ 0.5 unit cell per minute was used.

Reflection high-energy electron diffraction (RHEED) was used to monitor *in situ* thin film growth. Two-dimensional layer-by-layer epitaxial growth is characterized by sharp and streaky RHEED patterns as well as oscillations in the intensity of the specular beam during deposition. We used RHEED to characterize the growth in real time, allowing

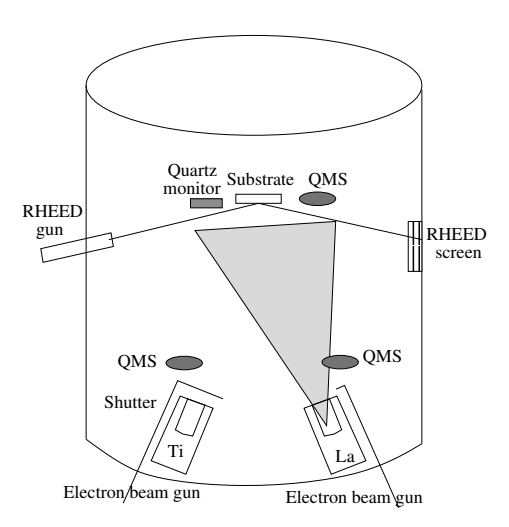


Figure 2.3: Schematic of the deposition and analysis facility used at IBM Zürich Research Laboratory for the growth of oxide materials.

modification of the growth parameters as well as corrections to any departure from stoichiometry, if necessary. These deviations usually appear as precipitates, easily recognizable by the presence of spots, with different spacings and geometry, on the RHEED patterns [39, 38].

2.2 Structural analysis of thin films

After the deposition process and before proceeding to the physical measurements, a detailed structural characterization of the films was carried out. X-ray analyses allow the determination of the phase and the structural quality and provide information on the epitaxial relation between the crystallographic structure of the thin film and that of the substrate. In the study of LTO, where intergrowth of different structures was suspected (due to the incorporation of additional oxygen), Dr. Maria Seo performed transmission electron microscopy (TEM) measurements to investigate the structure of LTO thin films.

2.2.1 X-ray analyses

X-ray is a powerful non destructive technique to study the structure of thin films. We used a four-circle Siemens D5000 diffractometer equipped with a graphite monochromator in the diffracted beam, particularly suited for reflectivity measurements and in the last six months a four-circle Philips X-Pro diffractometer equipped with an asymmetric 4 bounce Ge(220) monochromator on the incident beam path, both with a Cu-tube $(\lambda_{K\alpha} = 1.5406\text{\AA})$. A four-circle diffractometer allows four degrees of freedom for sam-

ple positioning:

 2θ : angle between the source and the detector

w: angle between the source and the sample-holder plane

 ϕ : rotating angle around the vector normal to the sample-holder plane

 ψ : angle between the sample-holder and the vector normal to the observed plane

The following measurement were performed in this study:

- \star $\theta-2\theta$ scan. ϕ and ψ are fixed and $\omega-2\theta$ are coupled scanned. The resulting spectrum yields the diffraction peaks of all planes oriented in one direction, according to the choice of ϕ and ψ .
- \star ω scan (rocking curve). ψ , ϕ and 2θ are fixed for a given diffraction plane, ω is scanned around the θ value: the width of the resulting peak gives information on the coherence of the grains oriented along the chosen direction.
- \star ϕ scan. ψ , ω and 2θ are fixed for a given diffraction plane, the film is rotated around ϕ allowing diffraction of all equivalent families of the considered planes. This analysis gives information on the symmetry of the unit cell and allows us to determine the epitaxial relation of the grown layer with respect to the substrate.
- * reflectivity. $\theta-2\theta$ are coupled scanned at grazing incident angles. The intensity spectrum is due to the reflection of the incident beam on the sample surface and the film-substrate interface. Depending on the sample surface roughness, the reflected beams from the different interfaces (air-film, film-substrate) can lead to an interference pattern observable through oscillations in the spectrum. The period of these oscillations depends only on the film thickness, irrespective of the cristallinity of the layer.

Finite size effect

For thin layers the diffraction profile broadens with decreasing layer thickness and exhibits interference fringes whose period is related to the layer thickness. Hence by modeling the broadening and the fringing it is possible to obtain an accurate measurement of the layer thickness. A rough estimation (if the x-ray coherence is larger than the film thickness) can be obtained by the Scherrer expression [40,41] that relates the thickness t to the profile breadth on the angular scale at half maximum $\Delta\theta$ of a given reflection 2θ

$$t = \frac{0.89\lambda}{\Delta\theta\cos\theta} \tag{2.1}$$

Making use of the oscillations, we can obtain a better estimation of the thickness:

$$t = \frac{(i-j)\lambda}{2\sin(\omega_i' - \omega_j')}$$
 (2.2)

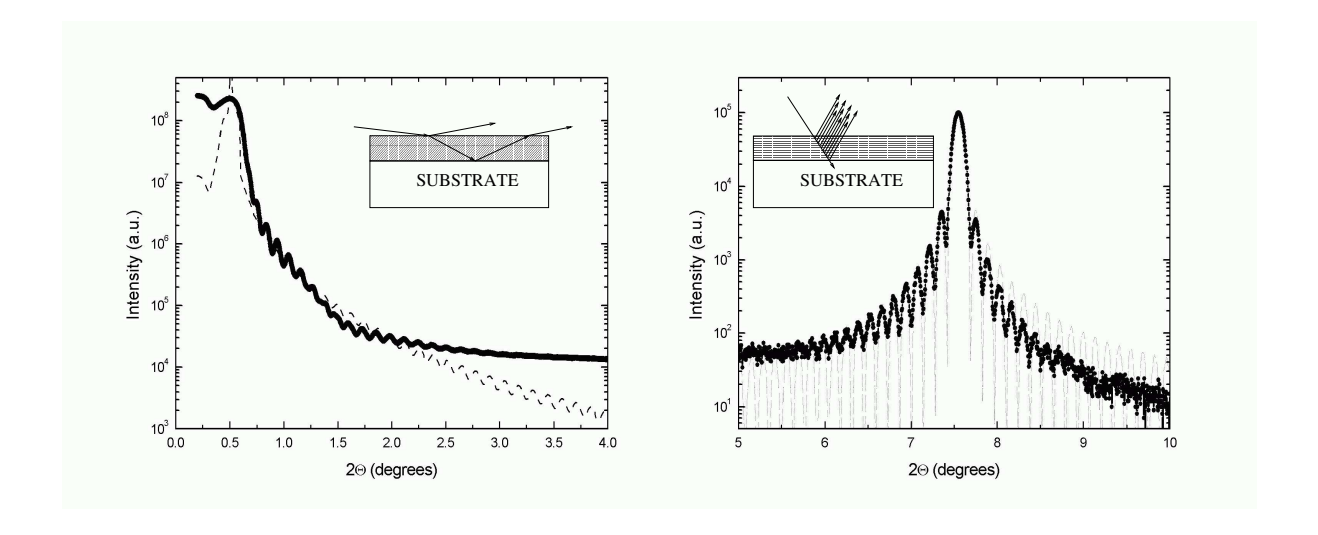


Figure 2.4: Left: Reflectivity measurement of a NBCO film: the fit (dashed line) yields a thickness of 65 nm. Inset: schematic view of the reflectivity principle: reflected beams from the interfaces interfere inphase or out-of-phase as a function of the incoming angle. Right: finite size effect maxima around the (001) peak of the same film and the fit for a layer with 50 unit cells with cell parameter 0.1186 nm (total thickness 64 nm). Inset: schematic view of Bragg diffraction from a finite number of diffracting cells: diffracted beams from each atomic layer interfere in-phase or out-of-phase as a function of the diffraction angle.

where i and j are the fringe orders and ω' is half the scattering angle. This formula, derived from Bragg's law, is obtained from the interference of the beam diffracted from the changes in x-ray refractive index and thus can be used in reflectometry and in high angle diffraction. In order to increase the precision of the thickness measurement, we have numerically simulated these oscillations. Figure 2.4 shows finite size effect oscillations for a thin NBCO film with the numerical fits superimposed. In this numerical approach we have simulated the subsidiary maxima appearing on the side of the diffraction peak as originating from a multilayer structure where the diffraction intensity is given by

$$I = I_{max} \left(\frac{\sin(2\pi Nc\sin\theta/\lambda)}{\sin(2\pi c\sin\theta/\lambda)} \right)^2$$
 (2.3)

where N is the number of unit cell with lattice constant c. With this simple formula we can estimate the thickness with a precision of 5%-10%. A detailed description of low angle finite size effect oscillations is given in [42, 43] and a complete review of thin film x-ray analysis can be found in [44, 45].

2.2.2 Transmission Electron Microscopy

Transmission electron microscopy analyses were carried out by Dr. Maria Seo to determine the structural properties of the LTO thin films grown on different substrates at

different oxygen working-pressure. Plan-view samples were prepared by cutting, grinding and finally thinning the material with an Ar-ion beam until electron transparency was achieved. Two microscopes were used for this study: a JEOL 2010 located at IBM Zürich Research Laboratory and a JEOL 4000FX located at the Research Centre of Jülich, Germany, operating at 200 and 400 kV respectively.

2.3 Lithographic patterning

The need for a well-defined geometry for transport property measurements in thin films, especially for Hall effect analysis, led us to lithographically pattern our films and heterostructures with two different processes. In this section we introduce the standard lithographic process while the second process developed for field effect heterostructures will be describe in chapter 3.

In the standard process, the superconducting sample is covered with an amorphous layer to protect the film from any degradation (mainly loss of oxygen) during the lithographic process; bare LTO films proved to be unaffected by the processing. A 1.3 μ m positive photoresist is deposited onto the surface, spun at 4000 t/min for 30 s and heated at $90^{\circ}C$ on a hot plate for 1 min. Using a mask-aligner with the desired path to pattern on a negative mask, the photoresist layer is exposed to a light beam (λ =348 nm) for 20-30 s with a power of 200 W. The sample is immersed in photoresist developer for 1 min and then rinsed in water. We note that the energy of the light (time and power) and the developing process ultimately define the real dimensions of the path. We used a neutralized ion-beam to remove the material outside the path operated with an ion-current of 1 mA/cm² and an energy of 500 V, equivalent to an etching rate of 15 nm/min for our materials. Finally, an ultrasonic bath of acetone removes the photoresist from the path.

2.4 Transport measurements: resistivity and Hall effect

Transport measurements are an effective technique to get information on conduction processes, charge carrier density and charge carrier sign. We performed resistivity and Hall effect measurements at low temperatures and investigated the resistivity at high temperatures for the LTO compound. The measurement of the resistivity in the low temperature range was performed using a homemade dipping station, where the sample temperature is varied continuously between room temperature and liquid 4 He. The resistance is measured using a 4-point technique. This technique eliminates contact resistance by forcing a current through the sample with one pair of leads while measuring the voltage drop with a second pair of leads. In addition, the current reversal method is used to eliminate the effects of thermoelectric offset voltages. High-temperature resistivity measurements were performed in a quartz tube, where the atmosphere can be changed from reducing (Ar pressure) to oxidizing (O_2 pressure), inserted in a furnace. The temperature is mea-

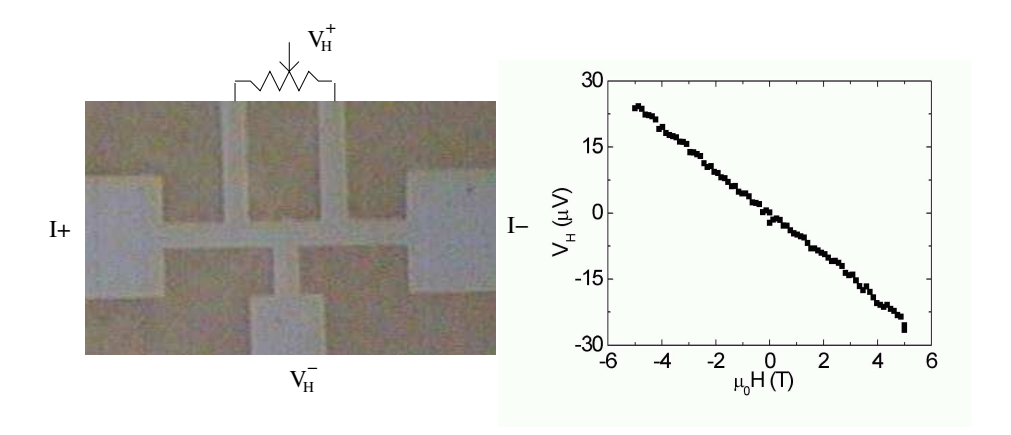


Figure 2.5: Left: Microscope view of a Hall path in a field effect heterostructure: the width of the path is $20\mu m$ and the distance between the resistivity (top) contacts is $80\mu m$. Right: Hall voltage as a function of magnetic field for a LTO thin film. The Hall constant is obtained from the slope of the linear fit to the curve.

sured with a thermocouple (type S) coupled to the alumina sample holder. We used silver paste to contact gold wires to the sample and we measured the resistivity with a 4-probe technique.

Hall effect is measured in an Oxford Spectromag flux-flow cryostat with an 8 Tesla split-coil magnet. We use a three-terminal technique where a single Hall electrode is opposed to two electrodes connected by a variable resistance, in order to null the longitudinal contribution in zero field (fig. 2.5). Particular attention has been paid to stabilizing the sample temperature ($\pm 0.005^{\circ}$ below 200 K) before sweeping the magnetic field between +5 Tesla and -5 Tesla. The Hall constant $R_H = \frac{V_H h}{IB}$ being V_H the Hall or transversal voltage, h the thickness of the layer, I the current and B the magnetic field, is calculated from the slope of the Hall voltage in the magnetic field sweep, as shown in figure 2.5. By applying two current densities, we verified the sample to always be in an ohmic regime where V_H is proportional to I.

The quality and the noise of transport measurements is determined mainly by the electrical contacts to the sample. Contact resistances with values higher than the sample resistance define the impedance for the nanovoltmeter, limiting the resolution of the measurement and bringing the main contribution to the Johnson noise. Moreover these set a limit on the current in order to prevent local heating due to the dissipated power and consequently limit the signal to noise ratio . To contact our samples, we evaporate a thin gold layer ($\approx 20nm$) on the lithographically-defined contacts, to which we attach 25 μ m of diameter aluminium wire using an ultrasonic bonding machine. The bonding needle punches the wire into the film, reaching the substrate; due to the local heating some gold diffuses in the thin film and the wire bonds to the metallic gold layer.

Chapter 3

Ferroelectric Field Effect in thin superconducting films

3.1 Ferroelectric Field Effect

An electric field applied through an insulating layer to the surface of a semiconductor can change the resistivity of the latter by many orders of magnitude as a result of the formation of depletion or accumulation layers in the surface region. This effect, called the field effect, is the basis of operation of the field-effect transistor. The field effect can also be observed in metals, though its magnitude is appreciably decreased because the electrostatic field is effectively screened by the high density of free carriers and penetrates into the metal for less than 0.1 nm, a distance equal to the Thomas-Fermi screening length. The resulting relative change of the carrier concentration is small and leads to only a small change of the properties. Another category of materials where field effect can be interestingly applied is superconductors. There, the idea is to use the field effect to control or modulate the properties of the superconductor. Indeed, pioneering field effect experiments in classical superconductors were performed by Glover and Sherrill [46] in 1960. Those showed an extremely small shift of the transition temperature, about 10^{-4} K. The discovery of high temperature superconductors (HTSCs) opened up new possibilities for the investigation and application of the field effect. Since HTSCs have a carrier density much lower than classical superconductors and since their superconducting $(T_c, \text{ critical})$ current J_c) and normal state properties are extremely sensitive to small changes of the carrier concentration, these materials seem particularly interesting candidates for field effect experiments. In 1991, Mannhart, Schlom, Bednorz and Müller first applied this idea to HTSCs [47], rapidly followed by others [48,49,50]. These experiments performed in the 1990s established the technique as a helpful new tool for investigating the nature of high temperature superconductivity and a potential basis of practical applications. A summary of the state of the field was given by Mannhart in 1996 [51].

An alternative approach to the field effect experiments described above is to replace the

dielectric material by a ferroelectric. A ferroelectric material can be described as a dielectric with a non-zero electric dipole moment in the absence of any electric field. This macroscopic, spontaneous electric dipole moment is nonvolatile and can be switched by applying an electric field larger than the coercive field across the material. It is thus possible to inject or deplete carriers at the superconducting surface (interface) in a ferroelectric/superconductor heterostructure, eventually changing its properties, by switching the polarization direction of the ferroelectric. Already in 1965 the use of ferroelectric materials as insulating layers to induce field effect was demonstrated in low-temperature superconductors [52]. Today, materials such as $Pb(Zr_{0.2}Ti_{0.8})O_3$ (PZT), with a very large polarization of the order of $P \sim 40 \ \mu\text{C/cm}^2$ (1-3 $10^{14} \text{ charges/cm}^2$), can be epitaxially grown with HTSCs in heterostructures, making the ferroelectric field effect an interesting approach to investigate the nature of HTSCs and eventually to realize new devices. An advantage of this approach is that it offers a way to tune the carrier concentration reversibly, over a wide range, without changing the stoichiometry and without introducing disorder. In this thesis we have carried out ferroelectric field effect experiments on HTSC ultrathin films with the following aims:

- \star superconductivity modulation. We have modulated the superconducting properties (inducing a shift of the critical temperature), in the most extreme case successfully inducing a superconductor-insulator transition. These experiments allow us to access the insulating state through a pure electrostatic hole doping of the CuO₂ plane without modifying the disorder of the system.
- * **normal state modulation**. We have measured the transport properties in the normal state for the two different polarization states to help clarify the role of the carrier concentration in the temperature dependence of the longitudinal and transverse resistivity.

3.2 High-Temperature Superconductivity

The cuprate HTSCs have highlighted a major problem of the quantum theory of solids which, in the form of one-electron band theory, has been very successful in describing semiconductors or good metals (like Cu) but has proven inadequate for strongly correlated electron systems. The Bardeen-Cooper-Schrieffer (BCS) theory [53] which was developed for Fermi liquid (FL)-like metals and has been so successful in describing conventional superconductors, does not seem to have the appropriate foundation for the description of high- T_c superconductivity either (see table 3.1). Soon after their discovery, it became clear that a new theoretical approach was needed [54]. HTSCs are poor conductors in the normal state with a behavior fundamentally different from the FL paradigm [55], and in fact are better described as doped antiferromagnetic (AF) insulators. It is well know that the pairing state in the BCS theory does not need to be caused by an interaction between electrons and lattice vibrations. In the literature there are different

Physical properties	BCS/FL prediction	Experiment				
$T < T_c$						
NMR $1/T_1$	Coherent peak	absent				
Isotope effect	α =0.5 or less	$-0.013 < \alpha < +1.0$				
Thermal conductivity	Decreasing	Enhancement				
Gap	$3.5K_BT_c$	$7-8K_BT_c$ (for T_c =90 K), indep. of T_c				
$T > T_c$						
Hall constant	constant	~1/T				
Korringa ratio $1/T_1T$	constant	T dependent				
Thermopower	\sim T, small	Nonlinear, large				
Infrared conductivity	Drude law	Mid-infrared maximum				

Table 3.1: BCS/FL predictions and experimental results for high- T_c copper oxides [56].

theories of unconventional pairing that replace phonons by another collective bosonic excitation of the solid. In the BCS theory, superconductivity results from an instability of the normal state, an instability of the Fermi surface. In HTSC today, there is no widely accepted theory allowing a description of the normal state. In particular, the discovery of a gap in the excitation spectrum in the normal state for the underdoped compounds, called the pseudogap (see [28] for a complete review), has divided theoretical approaches into two possible scenarios. In the first one, the normal state phase, including the pseudogap, is considered as being a phenomenon which is independent of superconductivity. In the second scenario, normal state properties and superconductivity are closely related and the pseudogap is believed to result from precursor pairing correlations above T_c .

In the next section we explore two different theories whose starting point is a new type of *normal* state, with new types of excitations in which the superconducting condensation involves wavefunctions very different in character from the BCS ground state. Our choice focuses on theories that have a model for transport properties in the normal state that can be tested in our field effect experiments.

3.2.1 The polaron-bipolaron model

The introduction of small polarons and small bipolarons (bound states of two polarons) into the theory of superconductivity has been proposed by Alexandrov and Ranninger (1981) [57]. They considered the BCS formula for the binding energy of the Cooper pairs (or energy gap)

$$\Delta \simeq 2\hbar w \exp(-1/\lambda)$$
 with $\lambda = VN(0)$ (3.1)

 $V \simeq 2E_P$ being the electron-electron interaction mediated by phonons, N(0) the density of states and w the Debye phonon frequency. λ is about 0.1-0.3 for metallic low

temperature superconductors. T_c is given by

$$k_B T_c \simeq \hbar w \exp\left(-\frac{1+\lambda}{\lambda}\right)$$
 (3.2)

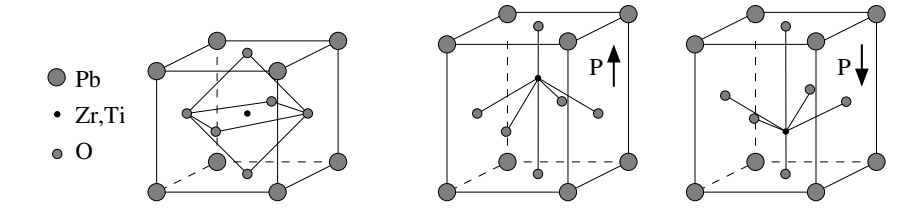
and remains fairly low (<40 K) for reasonable values of w and λ . In the limit of pairs with small size (no overlap between pairs) the effect of λ on the pair is important. As the coupling constant λ rises, we expect to find independent pairs existing above T_c . For extremely *strong* coupling we would expect to find electrons permanently bound into *pre-existing small pairs* at high temperatures. Superconductivity might then appear as a separate phenomenon at some lower temperature, if these pairs underwent Bose condensation into a common momentum state, with relatively weak binding into it because of the lack of overlap. The new point is that $\lambda \simeq 1$ is the condition for polaron formation. The electron band collapses into a narrow small-polaron one so that a gap extends across the whole Fermi distribution: the basic phenomenon that allows high T_c is the polaron narrowing of the band followed by an increase in the density of states N(0).

The bipolaron model for a CuO_2 plane assumes that all electrons are bound in small intersite bipolarons by lattice and spin distortion. Hole pairs, which appear with doping, have enough space to move and are responsible for the low-energy charge excitations of the CuO_2 plane. Above T_c a copper oxide contains a non-degenerate gas of these hole bipolarons. The low-energy band structure for hole pairs consists of two bosonic bands (for singlet and triplet states), separated by the singlet-triplet exchange energy J. The bipolaron binding energy is assumed to be large, $\Delta \gg k_B T$ and therefore single polarons are irrelevant in the temperature region under consideration. Alexandrov and Mott [56] argue that many features of the spin and charge excitations of cuprate oxides can be described within this simple model.

3.2.2 The spin fluctuation scenario

As we have seen in the phase diagram of cuprate superconductors (section 1.8.2), the materials with high T_c are located reasonably close to an antiferromagnetic (AF) state and have shown significant AF correlations in the paramagnetic state in magnetic experiments (NMR and neutron scattering). These observations have motivated the investigation of the role of AF spin fluctuations as a possible cause for both anomalous normal state behavior and unconventional superconductivity.

A semi-phenomenological theory of spin-mediated pairing proposed by Pines and coworkers [58] originates from the following experimental findings: ARPES measurements show that the planar quasiparticles possess a well-defined Fermi surface and NMR experiments reveal that there are strong AF correlations between neighboring Cu^{2+} spins and that the spin-spin correlation function $\chi(\mathbf{q}, w)$ is strongly peaked at $\mathbf{Q} = (\pi, \pi)$. The model assumes an effective *magnetic* interaction between *conduction* quasiparticles determined from fits to magnetic (NMR) experiments. In this model, the nearly antiferromagnetic



29

Figure 3.1: Perovkite ABO₃ structure of a ferroelectric compound: cubic structure at high temperatures (left) and tetragonal phases (middle and right) in the polar state with an indication of the two polarization states.

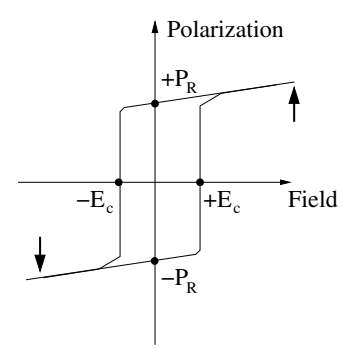


Figure 3.2: Ferroelectric (P-E) hysteresis loop. The arrows represent the polarization states.

Fermi liquid, the spin and charge degrees of freedom are not separated and their properties are determinated by quasiparticle interactions, as in a normal Fermi liquid. Finally, this model has demonstrated that AF spin fluctuations can yield high-temperature superconductivity in a 2D system.

3.3 Ferroelectricity

Ferroelectric materials possess a reversible, non-volatile macroscopic spontaneous electric dipole moment in the absence of any electric field. In the ferroelectric phase, the center of gravity of the positive ions within the unit cell is not equivalent to the center of gravity of the negative ions. This is shown in figure 3.1: comparing the cubic paraelectric phase and, for instance, the tetragonal ferroelectric phase of a ABO₃ perovskite structure (this will be the structure of the ferroelectric material used in our experiment) we observe a shift of the B and O ions relative to the A cations. In fact, the polar state is a consequence of the structural transition from a high temperature paraelectric phase into a low temperature ferroelectric phase; the temperature of the phase transition is called the Curie temperature.

The onset of P at the transition temperature induces the formation of a surface charge

which produces an electric field in the opposite direction, called the depolarization field, rendering an unscreened ferroelectric domain unstable. However, screening the depolarization field with charges from the surrounding material stabilizes the ferroelectric domains. The ferroelectric polarization can be reversed by applying an electric field E and the ferroelectric hysteresis (P-E) loop can be measured by using the so called Sawyer-Tower circuit (see section 3.3.1). Figure 3.2 shows a typical P-E loop. As one goes from a state with negative displacement (\downarrow) and starts to apply a positive field, a minimum field called the coercive field (E_c) is needed to switch into a positive displacement (\uparrow). All ferroelectric materials are also piezoelectric, such that applied stress will induce a linear change in the polarization. The inverse is also true, with an applied field inducing a linear strain in the material: depending on the sign of the applied voltage with respect to the direction of the polarization the material will either expand or contract.

3.3.1 Sawyer-Tower circuit

A common technique used to characterize ferroelectric materials is the polarization hysteresis loop measurement performed with a Sawyer-Tower circuit, shown in fig. 3.3 [59,60]. The sample is connected in series with a reference capacitor C_{ref} much greater than the ferroelectric capacitor. The charge on the two capacitors being equal, the voltage across C_{ref} is proportional to the sample surface charge. Therefore, the polarization P of the sample is extracted from the value of the voltage V_y , knowing the surface of the electrodes on the ferroelectric sample. To obtain a hysteresis loop, the polarization value is recorded as a function of the sweep voltage V_x (saw-tooth signal). Since the voltage V_x is applied mainly across the ferroelectric layer ($C_{eq}^{-1} = C_{fer}^{-1} + C_{ref}^{-1}, C_{ref} >> C_{fer} \rightarrow C_{eq} = C_{fer}$) the effective field E is deduced from V_x knowing the sample thickness d. The data acquisition is performed using an oscilloscope, typically at an excitation signal of 1 kHz.

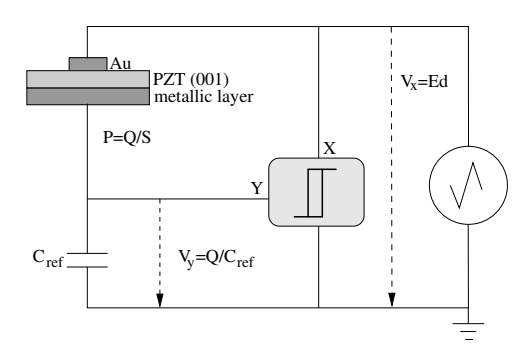


Figure 3.3: Circuit for the Sawyer-Tower polarization hysteresis loop. The sample is a PZT film with thickness d deposited on a metallic layer covered with a top electrode of surface S. X and Y are the input channels of the oscilloscope where the data are acquired and plotted.

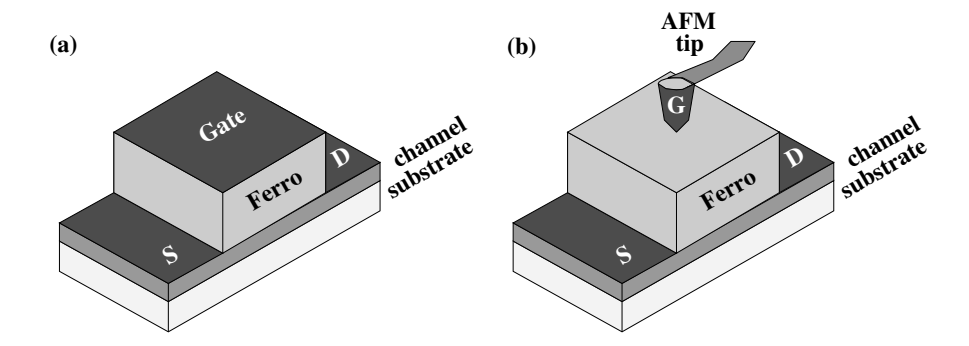


Figure 3.4: Schematic diagrams of the different configurations of ferroelectric field effect devices. (a) Conventional field effect geometry, (b) field effect geometry without gate electrode for AFM-based local probe approaches.

3.4 Ferroelectric Field Effect Devices

The basic structure of a ferroelectric field effect (FFE) device is shown in figure 3.4(a). In this three-terminal device, the flow of the current in the channel between the source (S) and drain (D) contacts can be modified by switching the polarization using the gate (G) electrode. In our experiments we used two different device configurations.

The FFE device has the advantage of a non-volatile polarization which induces a non-volatile change in the surface charge density. This allows the transport properties of the channel to be measured without any voltage applied to the gate. The same property allows us to replace the metallic gate electrode by a mobile conducting AFM tip. The idea is to scan the area to be switched with the AFM while applying a voltage between the tip and the bottom electrode. This technique has been shown to be effective for locally inducing charge doping [2].

The structure shown in figure 3.4(a) was used to modulate superconductivity while the device shown in figure 3.4(b) was used to modulate the normal state properties (in this latter case the area to be switched was rather small and the use of the AFM technique allowed us to avoid any possible short circuit problem).

The field effect in metals can be described by the Thomas-Fermi screening theory [61,62]. In this approach the depth of field penetration in metals is defined by the Thomas-Fermi screening length λ_{TF} [cm]:

$$\lambda_{TF} = \sqrt{\frac{\epsilon E_F}{6\pi n e^2}} \tag{3.3}$$

where ϵ is the permittivity, $n[\text{cm}^{-3}]$ is the carrier density of the channel, $E_F[\text{eV}]$ is the Fermi energy and e is the electronic charge. This formula shows that it is the carrier density that determines the screening length and thus the magnitude of the field effect. An estimation of λ_{TF} for Y123 using the values $\epsilon \simeq 100$, $E_F=1$ eV, and n=5 10^{21} holes/cm³ gives $\lambda_{TF} \simeq 1$ nm, roughly one unit cell. Substantial effects will thus be observed in

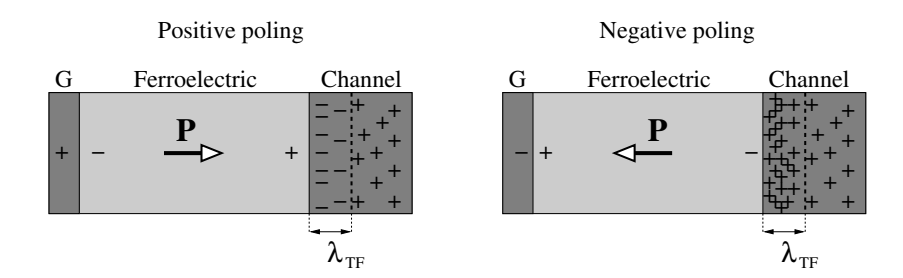


Figure 3.5: Schematic of a ferroelectric field effect structure with inversion (left) and accumulation (right) layers in a p-type conducting channel.

ultrathin films. Since the channel thickness d often exceeds the screening length, the channel layer can be described as made up of an undisturbed layer of thickness $d - \lambda_{TF}$ and of the layer with a modified carrier concentration of thickness λ_{TF} (however, the real situation is more complex: in a "continuous" material, the carrier concentration profile is exponential; in HTSCs, the layered structure of the materials will further modify the screening profile). The conduction in the channel can be described using a simple model of two resistances connected in parallel.

If we assume that the entire field-induced charge participates in conduction (equivalent to assuming that the effect of interface charge-trap states is negligible), the change in the mobile carrier concentration averaged over the entire metallic film due to ferroelectric polarization switching can be expressed in the form

$$\Delta n = \frac{2P_r}{ed} \tag{3.4}$$

where P_r is the remnant polarization of the ferroelectric material. The remnant polarization for PZT is $P_r \sim 15$ -45 $\mu \text{C/cm}^{-2}$ and yields a carrier change in a one-unit-cell thick layer (d=1 nm) of Δn =2-5 10^{21} cm⁻³. This value, being equal to the carrier density in optimally doped high T_c materials, demonstrates the potential of the ferroelectric polarization to induce strong field effects. As formula 3.4 shows, the field effect is strongly reduced as the film thickness is increased.

The sign of the resistance change depends on the type of carriers present in the channel with respect to the polarization direction. Assuming mobile hole-type carriers, a positive poling of the gate will result in a ferroelectric polarization pointing towards the channel and labeled P^- , inducing a hole depletion or inversion layer in the channel, as illustrated in figure 3.5, and thus causing an increase of the source-drain resistance. A negative poling of the gate will induce a ferroelectric polarization vector pointing towards the gate and labeled P^+ , inducing an accumulation layer in the channel.

Au

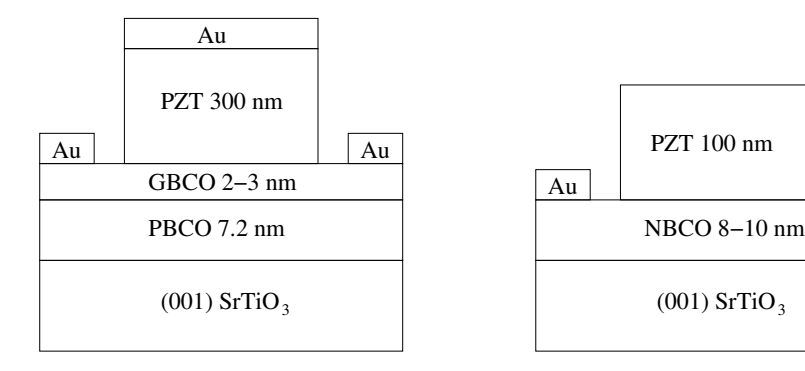


Figure 3.6: Schematic view of the FFE devices. Left: for superconductivity modulation experiments on a (001) SrTiO₃ substrate, a thin (001) PBCO buffer layer, an ultrathin superconducting (001) GBCO layer and a (001) PZT layer have been deposited. Right: in normal state modulation experiments we have grown on a (001) SrTiO₃ substrate a thin superconducting (001) NBCO layer and a (001) PZT layer.

3.5 Thin Film Growth and Characterization

3.5.1 Cuprate growth

As mentioned above, we have used different heterostructures for FFE experiments: figure 3.6 shows the schematics of the devices for superconductivity modulation (left) and normal state modulation (right). To grow extremely thin $GdBa_2Cu_3O_7$ layers, ~ 1 to 2 unit cells thick, in order to obtain substantial field effects in superconductivity modulation, we first grew a buffer layer of insulating $PrBa_2Cu_3O_7$ on the $SrTiO_3$ substrate. The use of a buffer layer, as shown previously for the growth of ultrathin $YBa_2Cu_3O_7$ [63] and multilayers [64], is necessary to observe superconductivity in ultrathin films (we discuss this effect in section 3.5.2). To prepare the cuprate oxides, we used off-axis radio-frequency-magnetron sputtering, with a mixture of oxygen and argon gas. We summarize in table 3.2 the growth parameters for $REBa_2Cu_3O_7$ (RE=Pr, Gd, Nd) on (001) $SrTiO_3$ single crystal substrates. After deposition, cuprate films were cooled slowly ($10^{\circ}C/min$) in an O_2 background pressure of 600 Torr.

A $\theta-2\theta$ x-ray analysis performed on a typical 10 nm thick NBCO film is shown in figure 3.7(left) and reveals c-axis growth. Low angle and finite size effect oscillations allowed us to determine the film thickness and to calibrate the deposition rate. To inves-

Compound	P(mTorr)	Ar/O_2	$T_{sub}(^{o}C)$	RF power(W)	rate(nm/min)
PrBa ₂ Cu ₃ O ₇	150	2.5	720	100	0.3-0.6
GdBa ₂ Cu ₃ O ₇	150	2.5	720	100	0.3-0.6
NdBa ₂ Cu ₃ O ₇	250	20	730	100	0.3-0.6

Table 3.2: Deposition parameters for $REBa_2Cu_3O_7$ on (001) SrTiO₃ substrate.

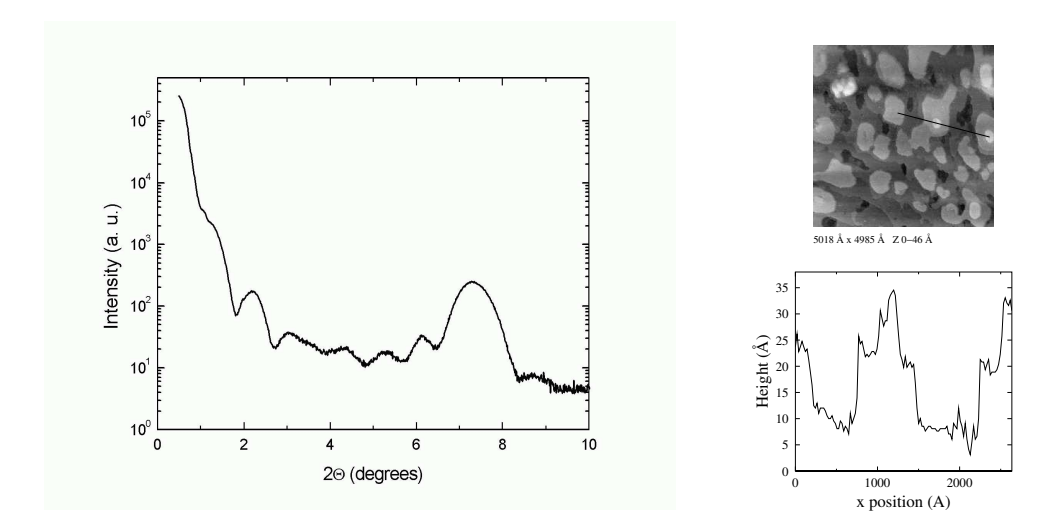


Figure 3.7: (left) $\theta - 2\theta$ scan of a 10 nm thick NBCO film revealing low-angle oscillations and finite size effects around the (001) peak. (right) Top: Scanning tunneling microscope topography of a 0.5 x 0.5 μ m² region of the surface of a 10 nm thick NBCO film. Bottom: Line scan along the black line shown above revealing one-unit-cell thick oscillations in thickness.

tigate the surface morphology of the thin films we performed atomic force microscopy (AFM) and scanning tunneling microscopy (STM) topographic measurements. These studies revealed smooth surfaces with a low density of scattered precipitates. The STM image shown in figure 3.7(right) displays a scan of 0.5 x 0.5 μ m² over a surface of a 10 nm thick NBCO film: we can observe that the film shows thickness variations of plus or minus one unit cell, confirming that the material grows locally unit cell by unit cell.

We tried to get some insight into the chemical composition of the precipitates by performing chemical analysis in a scanning electron microscope but their size was too small to allow for an analysis.

3.5.2 Finite size effect in High- T_c thin films

High-temperature superconductors are characterized by a layered crystal structure which results in anisotropic properties. This observation has led scientists to investigate the role played by the quasi 2D nature of these compounds. One of the question that was asked is: what is the critical temperature of a one unit cell thick $H-T_c$ layer? If these materials are actually 2D, one would expect that the properties of such a unit cell layer would essentially be the same as those of the bulk crystal. On the other hand, if the coupling between the unit cell layers is important, the properties of a unit cell thick layer might be very different from those of thicker layers. This type of question has motivated extensive work in the 123 compounds and in the BiSrCaCuO system, the latter being much more anisotropic than YBCO. A review of the field can be found in [64].

The question has been addressed by studying both multilayer structures and ultrathin films

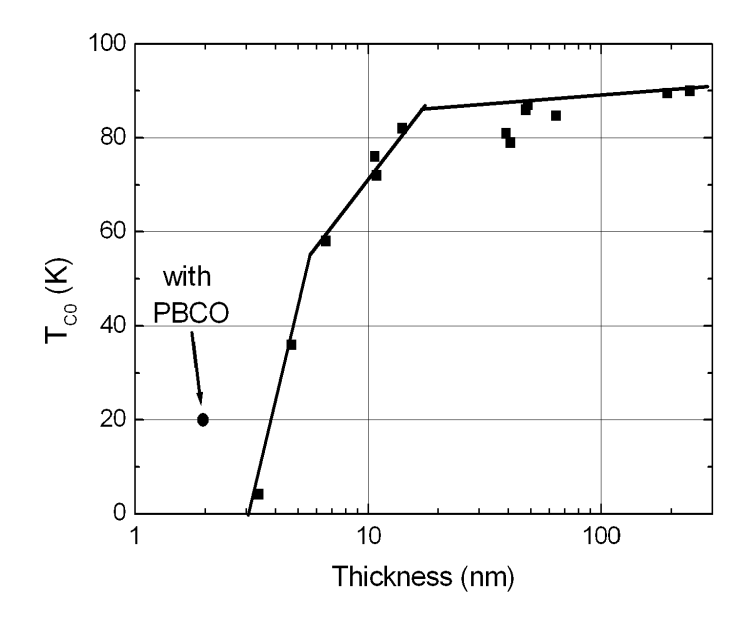


Figure 3.8: Plot of critical temperature T_c as a function of thickness for NBCO (single) thin films grown on bare (001) STO substrates: the experimental points are shown as squares and the line is a guide to the eye. An ultrathin GBCO layer grown on PBCO buffer layer is shown for comparison.

grown directly on the substrate. In YBCO, it was found that the critical temperature decreases as the film thickness is reduced. Various physical mechanisms have been put forward to explain this behavior, including substrate-induced strain effect [65], charge transfer or classical and quantum fluctuations [64].

Since in field effect experiments thin films will have to be used, we have investigated the effect of thickness on the properties of thin 123 films (with and without buffer layers). In figure 3.8 we show the critical temperature of thin NBCO films grown on STO substrates as a function of thickness: T_c decreases sharply below 20 nm. We note that a one unit cell thick 123 layer is not superconducting when deposited onto a bare substrate. Using a few unit cell thick PBCO buffer layer, the imperfections due to the substrate interface heal out and superconducting films can be obtained. The result obtained for an approximately 2 nm thick GBCO film prepared on a PBCO buffer is given in the graph. This data point fits well with what was found in multilayer experiments.

An important parameter for field effect experiments is the carrier density which can be influenced by the films thickness if, for instance, the oxydation process is modified. To check this, we carried out Hall effect measurements on single layer lithographically patterned samples with different thicknesses. As will be discussed later, the Hall effect in cuprates displays a complex behavior and extracting the carrier concentration is not obvious. However, several groups [66, 67, 68] have reliably shown that the measurement of the inverse Hall constant at 100 K in YBCO yields a carrier concentration value which

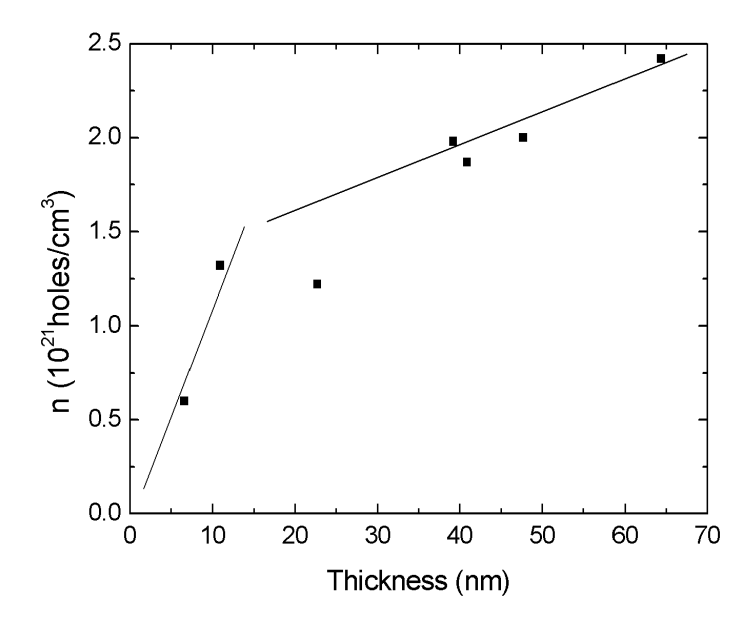


Figure 3.9: Carrier density at 100 K as a function of thickness for NBCO thin films grown on bare (001)STO substrates.

can be related to the chemical doping level. We will use this measurement to estimate the carrier concentration in our thin films.

Figure 3.9 displays the value of the carrier density n estimated at 100 K from the Hall constant R_H (using the formula $R_H^{-1} = ne$ where e is the electronic charge) versus the thickness. In this graph we observe a reduction of the effective hole doping with a decrease of the thickness of the layer. If this effect were due to a lower oxygen concentration, we would observe an increase in the c-axis of the films. From x-ray analysis of these films, we conclude that the c-axis does not vary significantly as a function of thickness. Nevertheless, we cannot exclude that the substrate tensile strain, which should result in a reduction of the c-axis for thinner films, is complicating the problem.

In these (single layer) films (which are still several unit cell thick) we found that the lowering of the critical temperature is in agreement with the reduction of the hole doping measured by Hall effect, as one would expect from the electronic phase diagram of H- T_c . The hole concentration p per unit cell can be related to the carrier density n in this doping range by $p=nV_{u.c.}-0.07$ where $V_{u.c}$ is the volume of a unit cell of the 123 compound ($V_{u.c}$ =0.167 nm³) and T_c in high- T_c compounds can be expressed as a function of p by the relation $T_c=T_c^*[1-\alpha(p-p^*)^2]$ where T_c^* is the maximum T_c of the 123 compound considered, p^* is the optimal doping ($p^*=0.16$) and $\alpha=82.6$ [69]. Figure 3.10 shows our experimental results and the relation for $T_c(p)$: the curve fits well to our data.

These results suggest that decreasing the thickness of the layer (in the thickness range investigated here) reduces the effective hole doping of the CuO₂, thus resulting in a low-

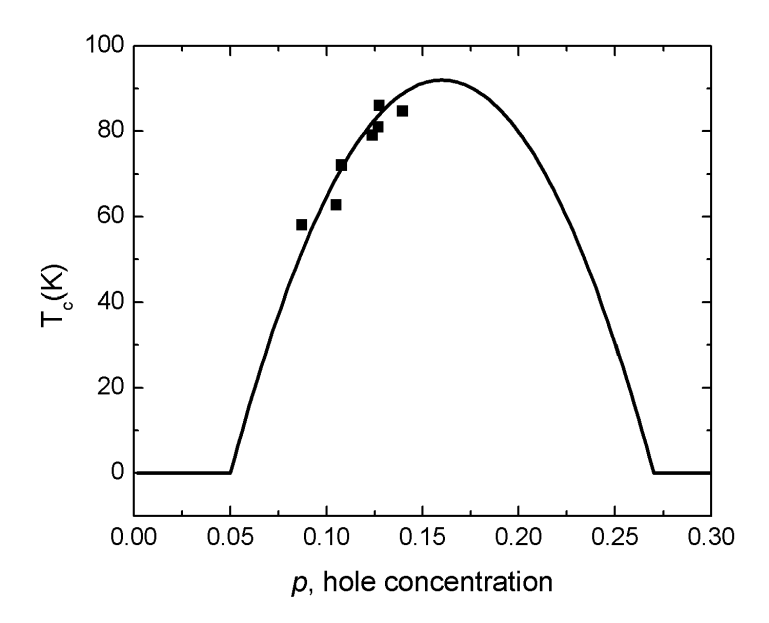


Figure 3.10: Critical temperature-doping $(T_c$ -p) phase diagram: the line is the observed T_c dependence with doping in chemical doping experiments, the dots are our thin NBCO films with different thicknesses.

ering of the critical temperature.

For this study, we will limit ourselves to this experimental result, i.e. reducing the thickness results in a natural underdoping of the (single) layer and we will measure the Hall constant at 100 K as systematically as possible to help us quantify the magnitude of the field effect. We note here that in the ultrathin (1-2 nm) GBCO films prepared on PBCO, the situation is more complicated, with different doping levels observed for rather similar preparation conditions.

3.5.3 PZT thin films

For ferroelectric field effect heterostructures we chose a ferroelectric material that is well lattice matched to the oxide superconductors and has a large remnant polarization. Our choice, also motivated by local competence [33], is Pb(Zr_{0.2}Ti_{0.8})O₃ (PZT), a perovskite compound which is tetragonal below the Curie temperature (\sim 490°C) with an in-plane lattice parameter of 0.395 nm, a c-axis of 0.415 nm and a remnant polarization of \sim 40 μ C/cm² [60]. PZT has two possible polarization directions, either parallel or antiparallel to the c-axis. Growing c-axis aligned thin films will result in a ferroelectric polarization normal to the metallic surface (the ideal configuration to obtain large field effect on the metallic layer underneath).

PZT thin films were grown by single target off-axis radio-frequency magnetron sputtering.

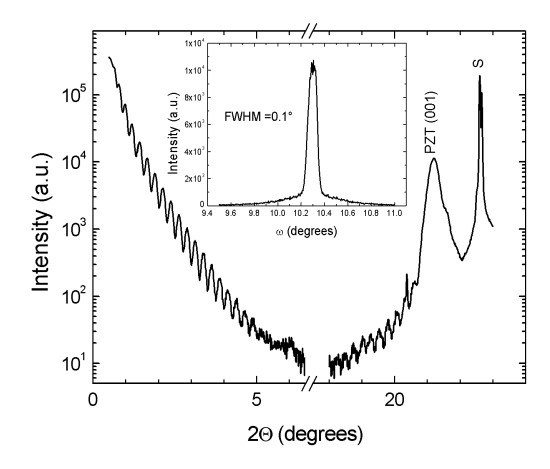


Figure 3.11: $\theta - 2\theta$ scan displaying low-angle oscillations and finite size effects around (001) peak of a 35 nm thick PZT layer grown on (001) STO substrate. Inset: rocking curve around (001) peak of the film displaying a full width at half maximum of 0.1° .

Due to the volatility of lead, the PZT targets had to have a 10% excess of Pb to obtain films with the desired composition [33]. An argon/oxygen atmosphere was used with a total pressure of 160 mTorr and an Ar/O₂ ratio of 10/3. The substrate was heated at \sim 510°C during deposition and the films were cooled in the background gas flow to room-temperature. With a radio-frequency power of 100 W and a target-substrate distance of \sim 30 mm the deposition rate is slow and found to be \sim 0.33 nm per minute. An x-ray analysis performed on the 35 nm thick PZT layer shown in figure 3.11 reveals c-axis growth and a high crystalline quality. Rocking curves taken around the 001 reflection typically have FWHM< 0.1°, comparable to the substrate values. We investigated the surface quality of PZT films by AFM topography and we observed smooth surfaces with a root-mean-square (RMS) roughness of \sim 0.2-0.3 nm over large areas, \sim 100 μ m².

3.6 Modulation of Superconductivity

3.6.1 PZT/GBCO/PBCO heterostructures

The schematic of the heterostructures grown to modulate superconductivity in ultrathin cuprate films is shown in figure 3.6(left). The growth of the PZT/GBCO/PBCO heterostructures was carried out in-situ as a sequential deposition of single layers, each layer grown as described in sections 3.5.1 and 3.5.3. After the growth of the PZT layer, the trilayer was cooled down to room temperature in an oxygen background pressure of 600 Torr.

X-ray diffraction confirmed the growth of PZT (001), GBCO (001) and PBCO (001) on STO (001) substrates. Off-axis scans revealed GBCO [100] (and PBCO [100])||STO [100], as well as epitaxial growth of tetragonal PZT (001) on GBCO (001), with PZT [100]||GBCO [100]. Rocking curves taken around the 005 reflection of PBCO and GBCO have typical full widths at half maximum (FWHM) of $\sim 0.09^{\circ}$, and rocking curves taken around the 001 reflection of PZT have a typical FWHM of $\sim 0.6^{\circ}$.

The heterostructures were then patterned into four-point resistivity paths, with gold being deposited for the current and voltage contacts as well as for the poling contact on top of the PZT layer.

3.6.2 P - E and R - E loops

We characterized ferroelectric layers by measuring P-E hysteresis loops taken using a Sawyer-Tower circuit. Figure 3.12 displays a P-E loop measurement performed on a 300 nm PZT/2 nm GBCO/7.2 nm PBCO heterostructure: the ferroelectric layer has a remnant polarization of $\sim 10~\mu\text{C/cm}^2$ and a coercive field of 100~kV/cm. Although the polarization of PZT thin films can reach $40~\mu\text{C/cm}^2$ [70,3], $10~\mu\text{C/cm}^2$ is the value generally measured in these types of heterostructures. We have no definite explanation for this low polarization. Most probably, since such a low polarization is not observed in single PZT layers, interface disorder and/or interdiffusion between PZT and YBCO are at the origin of this reduced polarization. It is however clear that further investigation should address this question since there is a lot of margin to improve the polarization of the PZT film and thus the magnitude of the field effect.

We also examined the ferroelectric properties by measuring the room temperature resistance of the channel as a function of the poling field used to establish the polarization state of the ferroelectric layer. A voltage pulse (\sim 1 s) was applied across the ferroelectric, after which the resistance was measured. By repeating this procedure for a series of different voltages, the ferroelectric hysteresis [resistance versus field (R-E)] was revealed. Figure 3.12 shows a R-E loop measured on the same sample. We observe a 10% change in resistance of the GBCO/PBCO bilayer channel between the two polarization states of PZT with the sign of the resistance change agreeing with the hole doped character of GBCO.

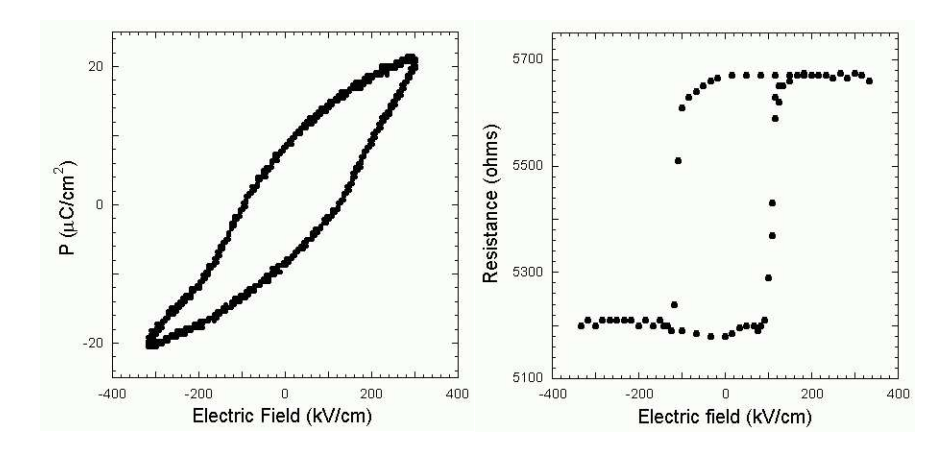


Figure 3.12: (left) A P_E hysteresis loop of a PZT/GBCO/PBCO heterostructure obtained trough a Sawyer-Tower measurement. (right) Ferroelectric hysteresis loop of this sample obtained with resistance measurements (R - E hysteresis).

The resistance states after application of the voltage pulses were nonvolatile for periods of weeks (the length of the experiments) and were also reversible, as demonstrated by the hysteresis. Although the coercive fields of $100\,\mathrm{kV/cm}$ evaluated from the P-E and R-E hysteresis loops agree (and agree with the bulk value of PZT), extracting a quantitative value for the remnant polarization is not straightforward from the R-E measurements, because the resistance change does not directly reveal the magnitude of the ferroelectric polarization. A free electron estimate, however, based on assuming $\Delta\sigma/\sigma\sim\Delta n/n$ where σ is the conductivity of the GBCO/PBCO bilayer and n is the carrier concentration, yields a value consistent with a polarization of $10~\mu\mathrm{C/cm^2}$ ($\Delta n/n=0.1$; from 3.4 $P_r=\Delta ned/2=0.1ned/2=0.1210^{21}[cm^{-3}]1.610^{-19}[C]10^{-6}[cm]/2=10[\mu\mathrm{C/cm^2}]$). We note that the hysteresis loop obtained with the resistance measurements (R-E) is considerably sharper than the P-E hysteresis loop obtained by the Sawyer-Tower measurement. The rounded nature of the P-E loop is attributable to leakage currents through the PZT layer, which are not present during the measurement of the R-E loop, because no voltage is applied across the ferroelectric during the measurement of the resistance.

3.6.3 Shift of T_c

We then studied the low-temperature transport properties of these heterostructures. The resistivity of two different 300 nm PZT/ 2 nm GBCO/ 7.2 nm PBCO heterostructure as a function of temperature for both polarization states of the PZT layer is shown in figure 3.13 and 3.14. We have observed that during the fabrication of the heterostructures, the ferroelectric layer is uniformly poled. As a result, it was not possible to measure the resistivity for the unpolarized (randomly polarized) state of the ferroelectric. The resistivity of the channel results from the contribution of the two layers connected in parallel:

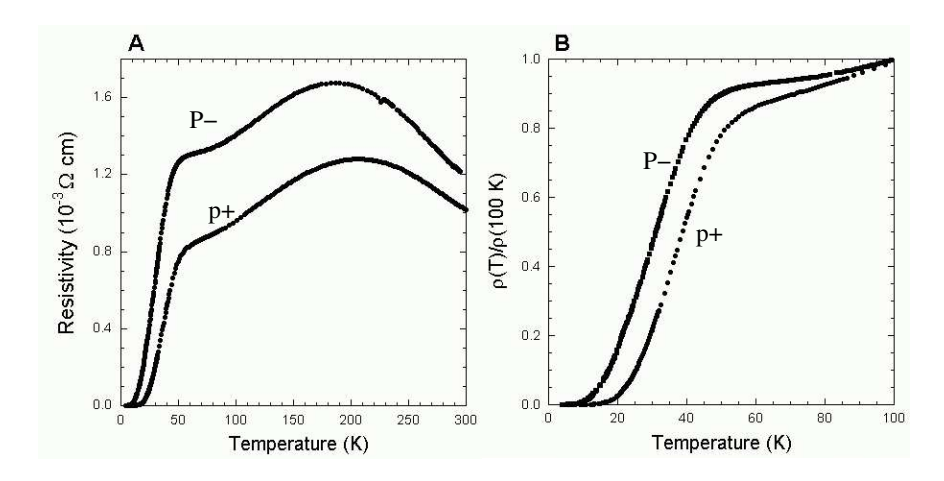


Figure 3.13: (A) Resistivity versus temperature of a 300 nm PZT/2 nm GBCO/7.2 nm PBCO heterostructure for the two polarization states of the PZT layer. The upper curve corresponds to a removal of holes from the p-type GBCO, resulting in an increase in the normal state resistivity and a depression of T_c by 7 K. (B) Expanded view of the data presented in (A). The resistivity of the two curves have been normalized at 100 K.

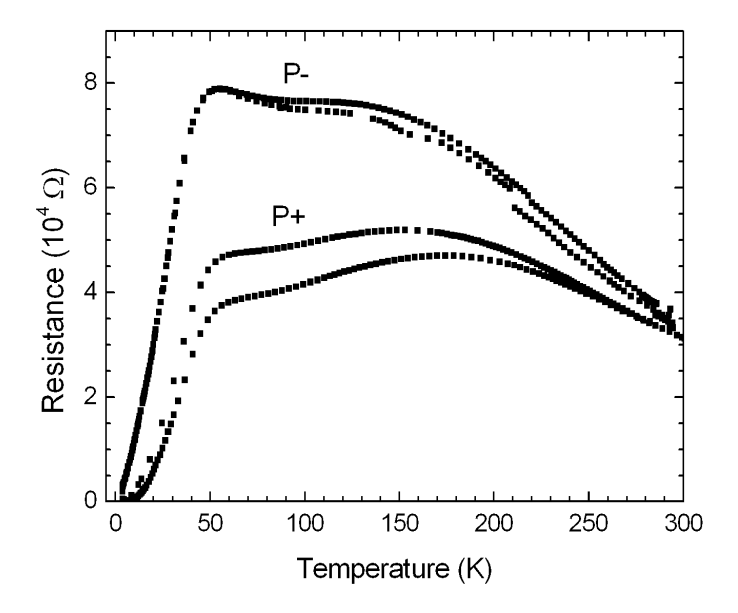


Figure 3.14: Resistivity versus temperature of a 300 nm PZT/2 nm GBCO/7.2 nm PBCO heterostructure for the two polarization states of the PZT layer. The upper curves correspond to a removal of holes from the p-type GBCO, resulting in an increase in the normal state resistivity and a depression of T_c . The resistance states are reversible, as demonstrated by the two measurements performed after the backswitching of the ferroelectric polarization.

the PBCO layer has a semiconducting behavior while the GBCO layer is metallic and becomes superconducting at ~ 20 K. At room temperature, the resistance of the thicker PBCO is lower than that of the GBCO layer and dominates the channel resistance. Focusing in turn on figure 3.13 we measured a resistivity change of 15% at room temperature upon switching the PZT polarization. Below 200 K, where the contribution of PBCO to the overall conductivity becomes negligible, metallic behavior is observed and the size of the field effect increases to $\sim 50\%$ at the transition temperature. At the transition, the polarization reversal induces a shift of 7 K between the two resistivity curves, the shift being maintained throughout the transition region, as demonstrated in figure 3.13(B). For the upper curve, the polarization vector points toward the substrate, corresponding to a removal of holes from the p-type GBCO, which results in a depression of T_c , whereas the lower curve corresponds to an addition of holes to the system.

In order to better quantify the ferroelectric field effect, we have carried out Hall effect measurements to determine the carrier concentration of these films. Because of geometrical constraints, it was not possible to measure the carrier concentration in the same heterostructures. The Hall effect measurements were performed on GBCO/PBCO bilayers showing similar resistivities, critical temperature and temperature dependence. Measurements of the inverse Hall constant at 100 K suggest a carrier density of \sim 2 10^{21} holes/cm³. With a measured remnant polarization of $10~\mu\text{C/cm}^2$, the polarization field of the ferroelectric removes 6 10^{20} holes/cm³ in our GBCO layer of thickness 2 nm ($\Delta n = \Delta P/ed$). We have reported these results on the experimental phase diagram obtained by chemical doping shown in figure 3.15. The arrow in the plot indicates the expected shift in carrier density due to the polarization field of the ferroelectric.

The large shift in transition temperature obtained by the ferroelectric field reversal illustrates the key role of the electronic doping level in determining the physical properties of these materials.

3.6.4 Superconductor-insulator transition

Superconductor-insulator (SI) transitions have been investigated theoretically and experimentally in a variety of systems. These transitions have been obtained by means of control parameters such as pressure, magnetic field, disorder and thickness. It has also been found in several low T_c systems that the SI transition takes place at a particular value of the sheet resistance of 6.4 k Ω ($4h/e^2$) although in many cases larger values were observed. A review on the SI transition has been written by A. Goldman and N. Markovic [71]. In HTSCs the phase diagram presents, in the underdoped regime, a SI transition at zero temperature, thus suggesting a quantum phase transition controlled solely by the doping level. Since a quantum phase transition takes place at T=0, critical fluctuations are purely quantum mechanical.

In our experiment we tuned the doping level using the polarization field of the ferroelectric as the control parameter and observed a transition from a superconducting to an insulating state. Figures 3.16 and 3.17 display the resistivity curves versus temperature

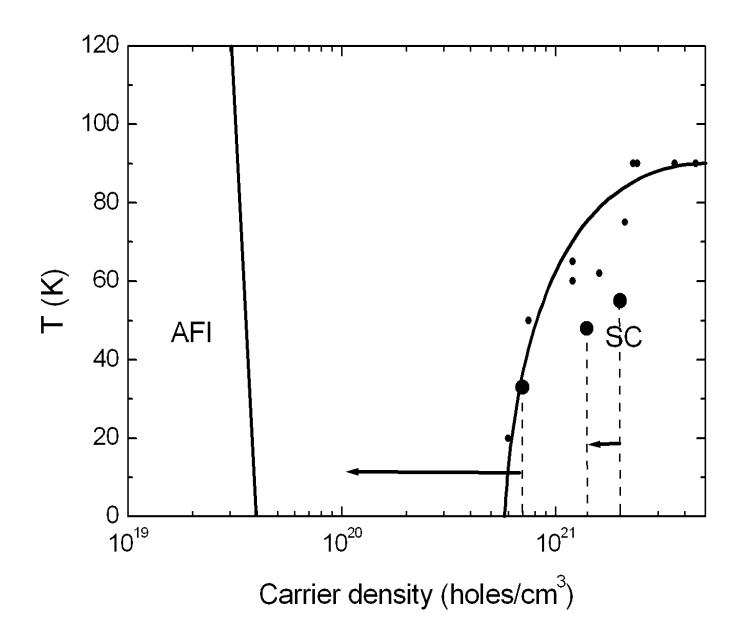


Figure 3.15: Schematic temperature-doping phase diagram for high-temperature superconductors. AFi and SC refer to the antiferromagnetic insulating Néel state and the superconducting state, respectively. The small circles are experimental data from [68]. Large circles indicate the experimental T_c onset data of this work, and the arrows indicate the shift in carrier density induced by the field effect. The orizontal axis is plotted on a log scale.

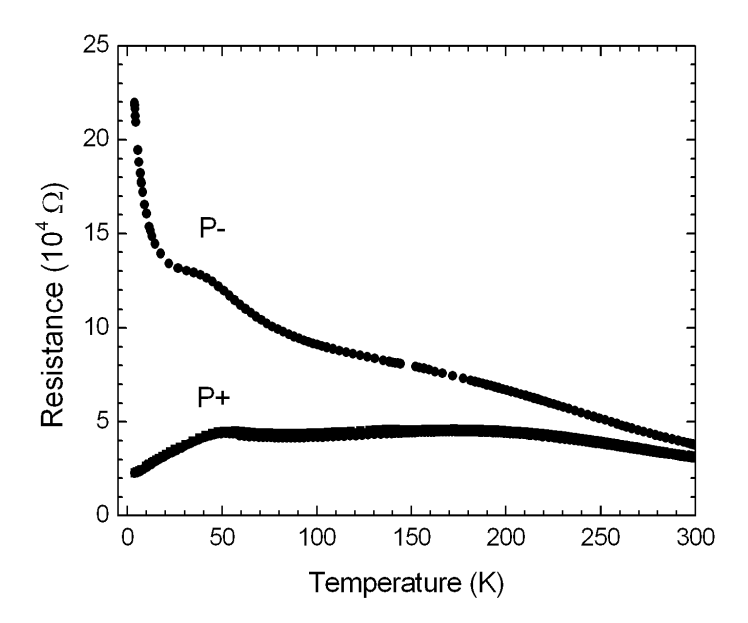


Figure 3.16: Resistivity versus temperature of a 300 nm PZT/2 nm GBCO/7.2 nm PBCO heterostructure for the two polarization states of the PZT layer. The upper curves, in which holes have been depleted from the channel, are insulating throughout the temperature range investigated.

for two different 300 nm PZT/ 2 nm GBCO/ 7.2 nm PBCO heterostructures 1: we focus our discussion on the data of figure 3.17. The thick lines are measurements taken in zero applied magnetic field, whereas the other curves (below 60 K) are measurements in magnetic fields of 1, 4 and 7 T applied perpendicular to the plane of the film. For the lower zero-field curve, the resistivity is essentially temperature-independent from 200 K down to \sim 50 K, where the onset of the superconducting transition occurs. The application of magnetic fields of up to 7 T has essentially no effect above 50 K, other than the small magnetoresistance that is expected in the normal state of GBCO. Below 50 K, however, the resistive transition broadens substantially with increasing magnetic field because of the motion of field-induced vortices in the superconducting state. Down to 1.5 K, the resistance of the channel remained finite. In contrast, the upper curves, which correspond to a depletion of holes by the ferroelectric polarization, are insulating throughout the temperature region investigated, except for a dip observed below 20 K. This dip proved to be sensitive to the applied magnetic fields, revealing its superconducting nature. We think that this dip on the insulating side is due to the non uniformity of the GBCO thickness over the entire film. In STM imaging we have indeed observed one-unit-cell thick variations in the film thickness. Because of the small Thomas-Fermi screening length in these materials, these thickness variations prevent the polarization field from acting throughout

¹We believe the differences between the samples investigated are due to run-to-run variations in the deposition parameters, such as, the substrate temperature and oxygenation of the samples.

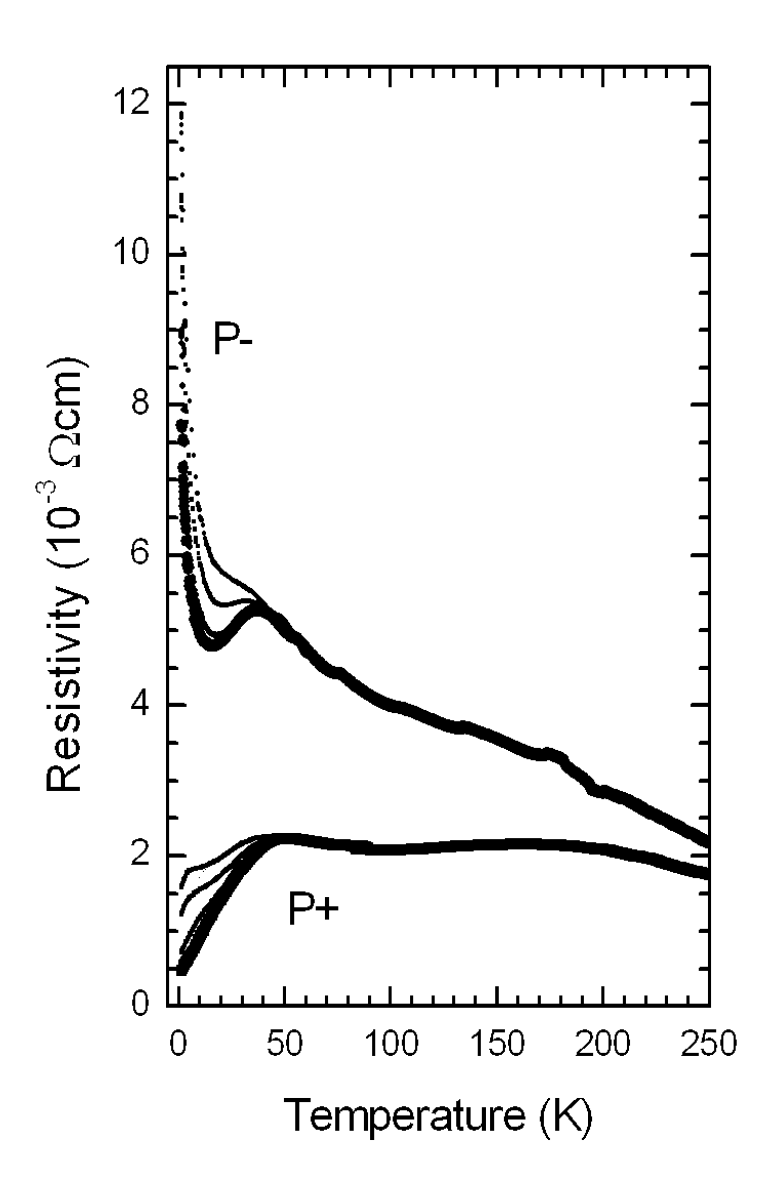


Figure 3.17: Resistivity versus temperature of a 300 nm PZT/2 nm GBCO/7.2 nm PBCO heterostructure for the two polarization states of the PZT layer. The upper curves, in which holes have been depleted from the channel, are insulating throughout the temperature range investigated. The thick curves are zero field measurements, whereas the other curves are measurements in magnetic fields of 1, 4 and 7 T.

the entire film thickness, leaving regions of the sample still superconducting.

We find that the transition occurs at a sheet resistance of about \sim 40 k Ω per square, a value six times higher than the quantum sheet resistance.

Although a detailed analysis of the insulating behavior was precluded by the limited temperature range of investigation, we tried to determine the mechanism of conduction by fitting the resistance with different temperature dependencies. At low temperatures, the insulating behavior is not simply thermally activated $\rho = \rho_o \exp[(E_c - E_F)/k_BT]$ with localized carriers excited from the Fermi level E_F to a mobility edge E_c by the thermal energy k_BT . Rather it can be fitted to variable range hopping (VRH) [16]

$$\rho = \rho_o \exp\left[-\left(\frac{T_o}{T}\right)^{-\frac{1}{4}}\right] \tag{3.5}$$

VRH describes electrons that hop from one localized state to another whose wave function overlaps that of the first state. The term T_o is related to the density of states N(E) at the Fermi energy and the localization length α

$$K_B T_o = \frac{1.5}{\alpha^3 N(E)} \tag{3.6}$$

Assuming a localization length $\alpha \sim 1$ nm, the density of localized states deduced from the fit to VRH is $\sim 10^{24}$ states/eV cm³. This unphysically large value suggests that VRH is not the appropriate conduction mechanism.

Recently, a study of the superconductor-insulator crossover [72, 73, 74, 75] in the underdoped and optimally doped region of the phase diagram of $H-T_c$ (both electron and hole doped) revealed that suppressing superconductivity with large (60 T) pulsed magnetic fields induces an insulating behavior which is characterized by the in-plane resistivity ρ_{ab} increasing as $\log(1/T)$. The authors note that this apparently diverging resistivity is sufficiently weak that it is experimentally difficult to precisely establish its functional form. Because the $\log(1/T)$ divergence is not attributable to any known localization mechanism, it has attracted substantial theoretical interest. The authors [72] speculate that the $\rho_{ab} \sim \log(1/T)$ insulating behavior might be associated with low dimensionality imposed by charge confinement onto stripes. Although, there are not many available data , a similar temperature dependence $\rho \sim \ln(1/T)$ in a 1D spin ladder compound [76] has recently been reported.

We have fitted the insulating behavior observed in our field effect experiments to the $\ln(1/T)$ behavior; the fit is shown in figure 3.18. The fits suggest that because the insulating state is not consistent with VRH, the samples may instead be in a quantum disordered state that exists between the Néel and the superconducting ground states [77, 78]. We note here that in bulk samples, VRH is observed at low doping levels in the antiferromagnetic Néel insulating state up to high temperature (\sim 50 K), and VRH in a Coulomb gap seems to be the dominant transport mechanism between the AF and SC state. Our data suggest that the field induced quantum insulating disordered state observed here might be similar to the state obtained by applying large magnetic fields to underdoped

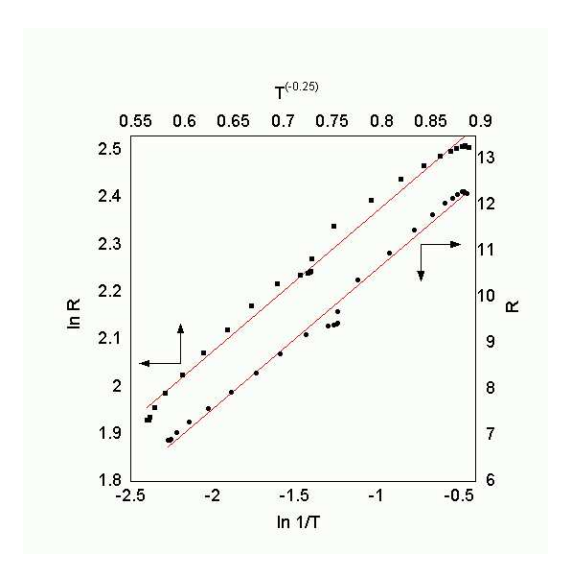


Figure 3.18: Fits of the low-temperature insulating behavior to variable range hopping and to $\ln(1/T)$ behavior.

cuprates ($\text{La}_{2-x}\text{Sr}_x\text{CuO}_4$, $\text{Pr}_{2-x}\text{Ce}_x\text{CuO}_4$, $\text{Bi}_2\text{Sr}_{2-x}\text{La}_x\text{CuO}_{6+\delta}$). We also note that in the field effect experiment, the disorder (doping) is fixed whereas the carrier concentration is changed. In chemical doping experiments, the disorder (doping) scales with the carrier density. In this sense the field induced insulating state (which displays the same temperature dependence of the resitivity as the magnetic field induced insulating state) also presents similarities with the magnetic field induced insulating state since the "disorder" is larger than in the "conventional" insulating state observed at low doping levels.

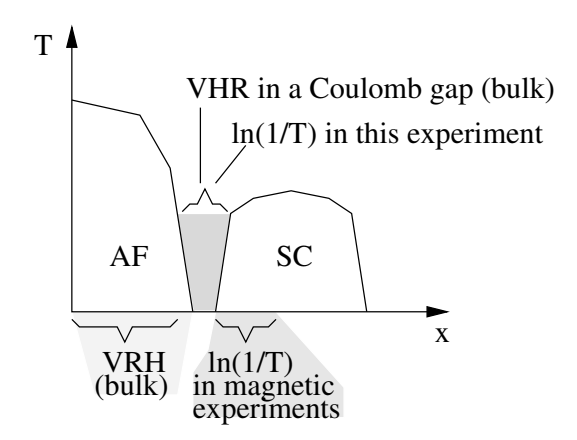


Figure 3.19: Schematic temperature-doping phase diagram of cuprates with the different temperature dependence fits observed in the insulating behavior of the antiferromagnetic region and the underdoped region.

3.7 Modulation of Normal State Properties

Soon after the discovery of cuprate superconductors, the anomalous normal state properties, which include a dc conductivity proportional to 1/T and a Hall angle proportional to 1/T² [79, 80, 81], have been recognized as distinctive signatures of these materials. However, the identification of the exact role of the carrier concentration in the temperature dependence of the longitudinal and transverse conductivities of these materials is a difficult task. Chemical doping, most commonly used to change the carrier concentration, invariably introduces disorder and often magnetic scattering, rendering the interpretation of data difficult.

Our experimental approach, based on the modulation of the carrier concentration using an electrostatic field effect, has allowed us to study the role of the carrier concentration in the resistivity and Hall constant without introducing any structural disorder.

3.7.1 PZT/NBCO heterostructures

Figure 3.6(right) shows a schematic side view of the devices studied in this work. To avoid the difficulty of having two "conducting" layers in parallel, we used single NBCO films without buffer layers in this experiment. Epitaxial PZT/NBCO heterostructures were grown by rf magnetron sputtering onto (001) STO substrates. Typical thicknesses were 8-10 nm for NBCO and 100 nm for PZT. X-ray finite size effects around the (001) reflection of NBCO layer allow for the direct determination of the film thickness. Figure 3.20 displays a $\theta-2\theta$ scan of a heterostructure revealing the (00l) peaks of NBCO and PZT layers. During the fabrication of the heterostructures, we observed that PZT layers sometimes present both c- and a-axis domains, probably due to a slight change in the substrate growth temperature. An a-axis domain has its ferroelectric polarization in the

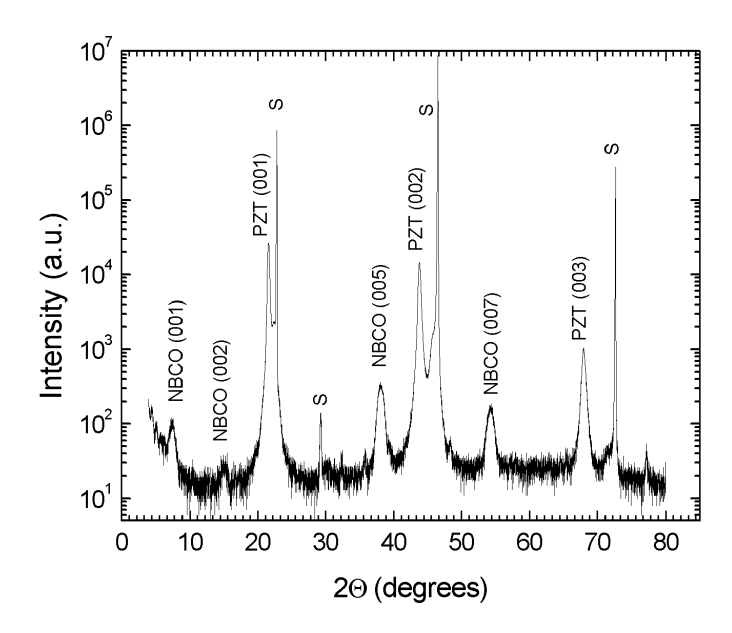


Figure 3.20: $\theta - 2\theta$ scan of a 100 nm PZT/ 10 nm NBCO bilayer grown onto (001) STO substrate.

plane of the film: thus it does not contribute to the field effect on the metallic layer underneath.

In order to acquire quantitative information about the transport properties of the HTSCs we locally switched the ferroelectric polarization in lithographically defined small resistivity paths using an atomic force microscope. This approach eliminates difficulties associated with shorting to top metallic electrode.

3.7.2 Lithographic patterning of FFE heterostructures

In this project, we developed a lithographic process [82] particularly suited to the sensitive films used here which avoids the degradation of the ultra-thin superconducting layer. The process begins by the deposition of photoresist onto the (001) STO substrate to define the path and contacts. The free surface area is then etched for 30 seconds in HF (concentration 10%) to promote the adhesion of a 30 nm thick Ti layer, which is deposited afterwards at room-temperature by DC sputtering. The photoresist is then removed with acetone and the Ti layer is oxidize in air at 400°C. During the oxidation process, the smooth Ti film becomes a rough layer of Ti-oxide grains. The substrate, with path and contacts carved in this Ti-oxide layer, is ready for deposition: the material grows epitaxially only onto the substrate, the Ti-oxide layer being too rough to allow crystalline growth of the material outside the path. We have verified that metallic conduction takes place only in the defined path: resistivity measurements performed on the Ti-oxide layer covered with a NBCO



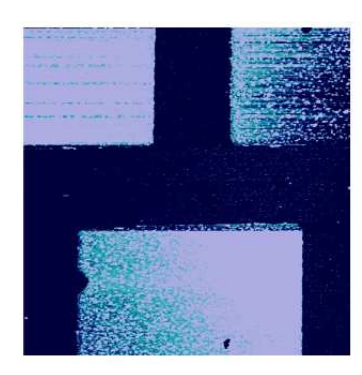


Figure 3.21: (left) A top view of a Hall path in a field effect heterostructure: the width of the path is 20 μ m and the distance between the resistivity (bottom) contacts is \sim 80 μ m. (right) AFM topography of the region between the contacts: the scan area is 100 μ m².

thin layer display very high resistance values and insulating behavior.

3.7.3 Local ferroelectric poling

Classically, to pole a ferroelectric material, one uses a capacitor structure with the ferroelectric sandwiched between two electrodes. By applying an electric field larger than the coercive field one switches the polarization. Since the ferroelectric state is non-volatile, it is possible to use a metallic atomic force microscope (AFM) tip as a mobile top electrode to polarize the regions of interest. In a previous series of works, our group has demonstrated the feasibility of using an AFM to polarize small regions of the ferroelectric layer [83, 84] and in FFE heterostructures to induce a local, non-volatile, and reversible changes in the electronic properties of the underlying metallic layer [2, 85]. In this study we have used a commercial atomic force microscope, a Nanoscope Multimode IIIa from Digital Instrument working in air at RT. An external voltage source operated at +10 V or -10 V was used to bias the tip while scanning the surface a few times with the lowest available scanning rate (0.1 Hz/line), in order to ensure a homogeneous final polarization state. Following the previous work of T. Tybell on ferroelectric AFM writing [85], we used a high bias voltage applied to the tip (2-3 times larger than the coercive field). This large voltage is necessary to ensure homogeneous polarization since any surface contamination will reduce the effective voltage applied across the ferroelectric film.

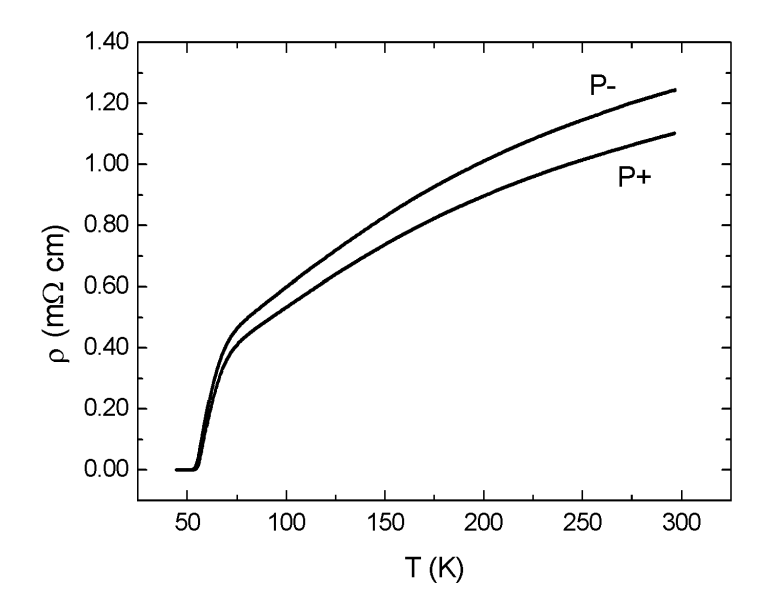


Figure 3.22: Resistivity versus temperature for the two polarization states. P^+ is the polarization direction that adds holes to the superconducting layer.

3.7.4 Resistance and Hall modulation

Figures 3.22 and 3.23 show the resistivity of two different 100 nm PZT/ 8 nm NBCO heterostructures as a function of temperature for the two polarization states. For both polarizations, the resistivity is metallic in the normal state throughout the temperature range investigated and goes to zero around 50 K. We note that the resistivity is not linear in temperature, a behavior often observed in very thin films. The difference in resistivity between the two polarization states is about 9% for the sample in figure 3.22 and 4% for the sample in figure 3.23 and is essentially constant over the entire temperature range. The polarization state P^+ , corresponding to hole doping of the superconducting channel, yields a lower resistive state and a higher transition temperature (\sim 1 K higher) than P^- , in agreement with the hole doped character of NBCO.

We then carried out Hall effect measurements on these samples. In figures 3.24 and 3.25 we show the inverse Hall constant R_H^{-1} of the two heterostructures as a function of temperature for the two polarization states. As is generally observed at high temperatures in 123 compounds, R_H^{-1} depends linearly on temperature $(R_H^{-1} = AT + B)$. This linear region is generally observed down to T_c for optimally doped samples and down to the pseudogap temperature T^* for underdoped samples [67, 66, 86]. For the sample shown in figure 3.24, we estimate T^* to be around 150 K, the temperature at which R_H^{-1} deviates from a linear temperature dependence. As can be seen from the data, the ferroelectric field effect changes the Hall constant. The relative change in R_H^{-1} associated with the

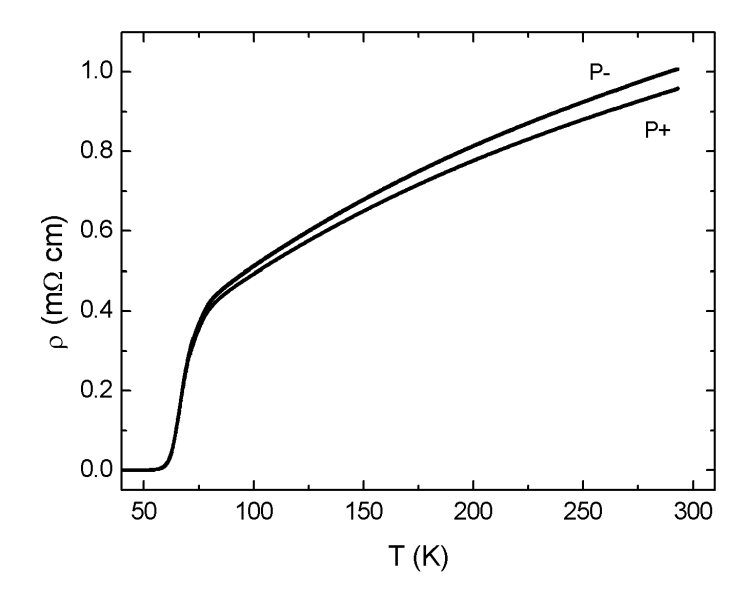


Figure 3.23: Resistivity versus temperature for the two polarization states. P^+ is the polarization direction that adds holes to the superconducting layer.

switching from P^+ to P^- is about 6% at any temperature with the sign being consistent with the hole doping of NBCO.

In the simplest theory of the Hall effect, the inverse Hall constant is related to the carrier density n: $R_H^{-1}=qn$, where q is the charge of the carriers. In HTSCs where the Hall constant is temperature dependent, the value of R_H^{-1} at a given temperature (usually 100 K) can be related to the doping level of the material and its carrier concentration. The change in R_H^{-1} demonstrates directly the change in the carrier concentration produced by the polarization reversal. One can try to estimate the polarization field by using the Hall data. Assuming that the inverse Hall constant is related to the carrier density by the expression $R_H^{-1}=qn$, the change in the Hall constant at $100~{\rm K}~\Delta R_H^{-1}\sim 2~10^7~{\rm C/m^3}$ in the film of thickness $\sim 10~{\rm nm}$ is produced by a polarization of $\sim 10~\mu{\rm C/cm^2}$, a value that agrees well with the measured polarization in the FFE heterostructures.

3.7.5 Variable versus fixed carrier density

The Hall effect results in HTSCs have forced some scientists to conclude that the mobile carrier density varies considerably with both doping and temperature. It does so in a manner which seems consistent with the idea that the system is making a gradual transition from a Hubbard band picture with some sort of mobility edge to a single band as the hole doping increases. The model has led to an essentially simple picture of the scat-

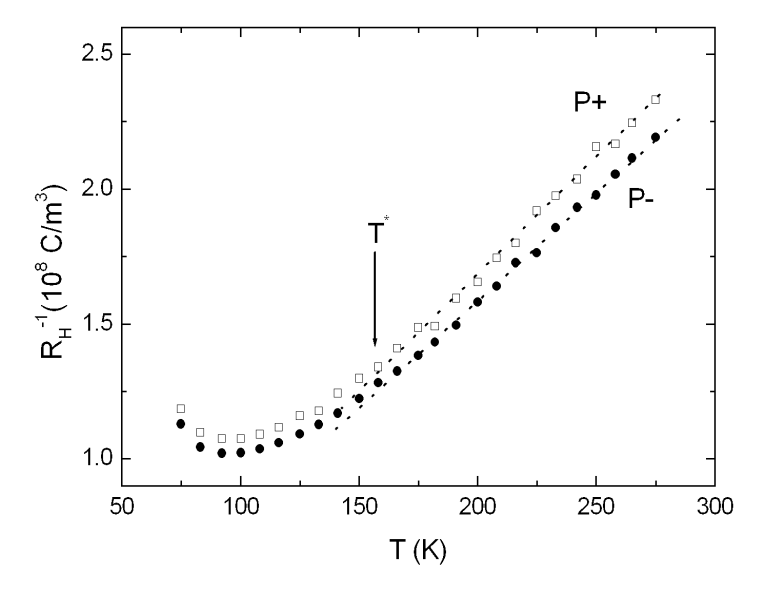


Figure 3.24: Inverse Hall constant R_H^{-1} as a function of temperature for the two polarization states. The dashed lines are fits of the data in the linear region.

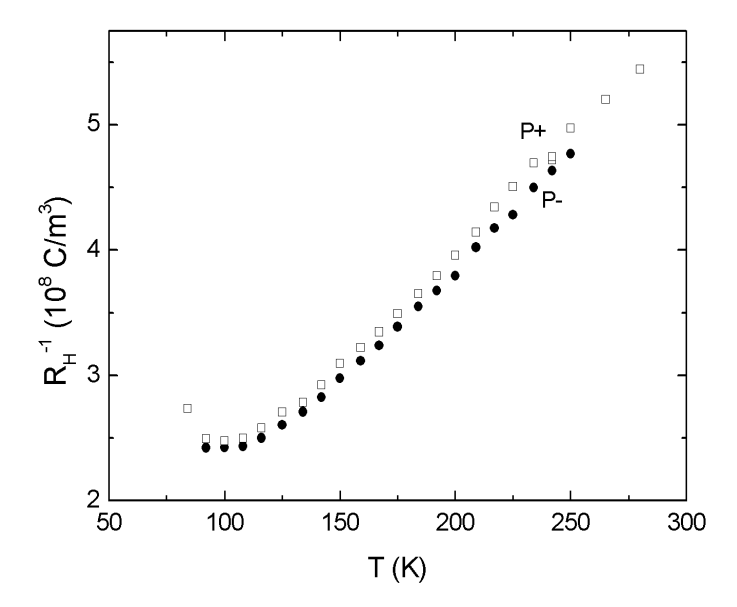


Figure 3.25: Inverse Hall constant R_H^{-1} as a function of temperature for the two polarization states.

tering: for all dopings we have isotropic electron-electron scattering proportional to T^2 plus residual scattering from impurities in the CuO_2 planes. At the other extreme some authors point to the ARPES measurements that display a Fermi surface which is close to the band-structure calculations and remains essentially constant over the whole of the metallic doping range. This would seem to correspond to a larger and more or less constant density of carriers.

These apparently very different ideas could perhaps be reconciled with the first model if we assumed that weakly localized states contributed to the ARPES Fermi surface but not to the transport properties. If this interpretation is correct, the apparent similarity of $\rho(T)$ in the optimally doped cuprates to that in copper is just a curious accident. The ideal scattering is interpreted as electron-electron scattering with a rate proportional to T^2 and not phonon scattering with a rate proportional to T. We just happen to get a linear $\rho(T)$ because the carrier concentration is not constant but roughly proportional to T in the optimized cuprates.

Such considerations have led some investigators to ask whether there might not be some way of explaining the transport measurements while retaining the picture of a more or less constant Fermi surface as found in the ARPES results without invoking localization. An alternative picture makes use of the fact that the measured Fermi surface has rather flat faces joined by relatively sharp corners and puts forward reasons for supposing that we may have very different scattering rates in these two regions. To explain the very different scattering rates at different places on the same Fermi surface, it is argued that the system has significant electron scattering of two types, scattering proportional to T by the spin fluctuations revealed by neutron scattering and electron-electron scattering proportional to T^2 .

3.7.6 Anderson localization of bipolarons

Belonging to the class of theories with variable carrier density, the description of the kinetic properties of bipolarons in copper oxides [56] takes into account their localization in a random potential. Because of low dimensionality (2D rather than 3D) any random potential leads to localization, no matter how weak it is. Coulomb repulsion limits the number of bosons in each localized state, so that the distribution function will show a mobility edge E_c . The total number of bosons per cell n is given by the sum of the density of extended (free) bosons $n_b(T)$ and of localized bosons $n_L(T)$: $n = n_b(T) + n_L(T)$. Localized charged bosons obey Fermi-Dirac statistics:

$$n_L(T) = \int_{-\infty}^{E_c} \frac{N_L(\epsilon)d\epsilon}{\exp((\epsilon - \mu)/T) + 1}$$
(3.7)

where $N_L(\epsilon)$ is the density of localized states and μ is the chemical potential. Near the mobility edge $N_L(\epsilon)$ remains constant $N_L(\epsilon) \simeq n_L/\gamma$ with γ of the order of a binding energy in a single random potential well and n_L the total number of localized states per

unit cell. The density n_b is then

$$n_b(T) = n - n_L + n_L bT \tag{3.8}$$

with temperature independent $b=\ln(1+y^{-1})/\gamma$ (with y given by $\mu=T\ln y$). Extended bosons are scattered by acoustic phonons, by each other and by an unscreened random potential with transport relaxation rates $\tau_{b-ac}\sim 1/T$, $\tau_{b-b}\sim 1/T^2$ and $\tau_{b-im}\sim 1/T$ respectively. Solving the Boltzmann equation for extended bosons yields

$$R_H = \frac{v_o}{2e(n - n_L + bn_L T)} \qquad \rho = \alpha \frac{T + \sigma_b T^2}{n - n_L + bn_L T}$$
(3.9)

where v_o is the volume of an elementary cell (0.167 nm³ for 123), α is a constant depending on the boson mass, charge and the scattering coefficients and σ_b is the boson-boson scattering cross section. In these formulas, there are two fitting parameters, n and n_L , expected to vary with doping.

3.7.7 Two scattering times model

A phenomenological model for the anisotropic quasiparticle scattering originates from the variation in the mean free path as one goes around the Fermi surface (FS). For simplicity, let us assume a cylindrical FS with approximately constant k_F but with an anisotropic effective mass m_k and anisotropic quasiparticle behavior which exhibit a fourfold symmetry. In this scenario, the quasiparticles are more strongly scattered in areas of the FS intercepting the magnetic Brillouin zone boundary, which are termed "hot" spots, than in other parts, which are called "cold" regions (see figure 3.26). This gives rise to two scattering times, τ_{hot} and τ_{cold} , that have a different temperature dependence and two effective masses m_{hot} and m_{cold} . The following expressions are then found for the resistivity and Hall constant [87]

$$\rho = \frac{1}{ne^2} \sqrt{\frac{m_{hot} m_{cold}}{\tau_{hot} \tau_{cold}}} \qquad R_H = \frac{1}{2ne} \sqrt{\frac{\tau_{cold} / m_{cold}}{\tau_{hot} / m_{hot}}}$$
(3.10)

One can use these equation to deduce the temperature dependence of $(m/\tau)_{hot}$ and $(m/\tau)_{cold}$ from the experimentally measured ρ and R_H ; only one undetermined parameter enters in this procedure, namely, n, the carrier density.

3.7.8 Implication of the modulation of the normal state properties

The estimate made in the following discussion is based on average changes in the Hall constant and resistivity of the film, although the field induced change in carrier concentration is inhomogeneous throughout the thickness of the layer. Since accounting for the

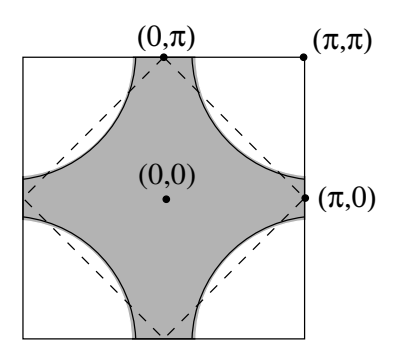


Figure 3.26: A model of the Fermi surface in cuprates (solid line) and the magnetic Brillouin zone boundary (dashed line). The intercepts of the two lines mark the hot regions.

inhomogeneous carrier distribution in a two-layer model requires a detailed modeling of the Hall response, we analyze the measured average change in the resistivity and Hall constant upon polarization reversal.

Since the ferroelectric polarization of PZT is temperature independent below room temperature, as shown in figure 3.27 [3], one expects the induced carrier density change Δn to be constant ($\Delta n = \Delta P/ed$) with temperature.

In our understanding of the localization scenario, the field effect modulates n, the total number of bosons per unit cell, but the number of localized states n_L stays constant, as we have not changed the random potential. From equation 3.9, a field-induced carrier modulation would result in a constant change of the inverse Hall constant $\Delta R_H^{-1}(T)$. The experimental data in figure 3.28 show, however,that ΔR_H^{-1} is not constant as a function of temperature. In fact, it changes by a factor of two between room temperature and T_c , as does R_H^{-1} itself. This behavior is observed for the samples shown in figures 3.24 and 3.25; later on, we will discuss in detail only figure 3.24.

The two-scattering-times scenario suggests that the carrier density n is a rescaling temperature-independent parameter for ρ and R_H , as shown in formulas 3.10. Figure 3.29 shows the two resistivity curves and figure 3.30 the two inverse Hall constant curves normalized at 100 K. We notice that the data rescale over the entire temperature range investigated and that the rescaling is not affected by the opening of the pseudogap.

Recent photoemission spectroscopy measurements of the temperature evolution of the FS reveal the partial destruction of the Fermi surface for $T < T^*$ with the corresponding lack of a continuous Fermi contour in momentum space [88]. In this phenomenological model, the pseudogap is taken into account through changes in τ_{hot} (the hot spots are the areas of the FS at which the pseudogap and superconducting gap open [89, 90]), leaving

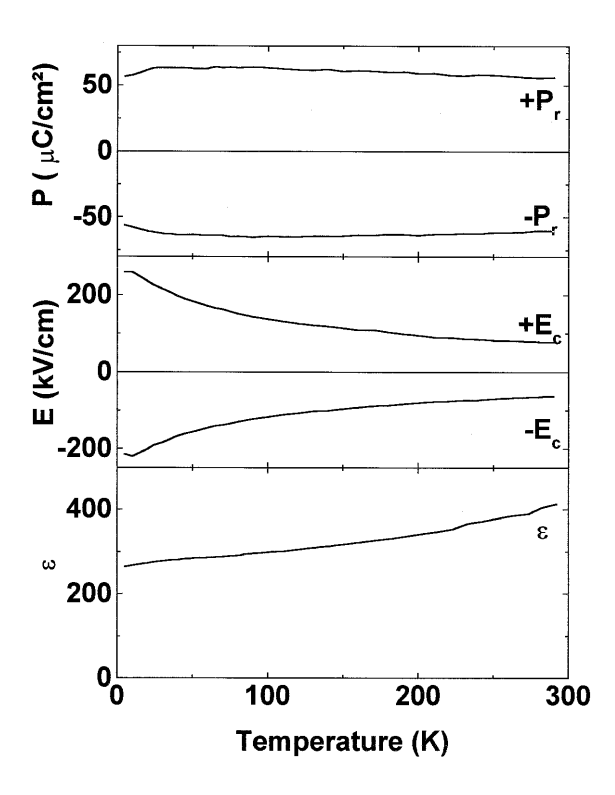


Figure 3.27: Temperature dependence of remnant polarization P, coercive field E and dielectric constant ϵ for PZT films (from [3]).

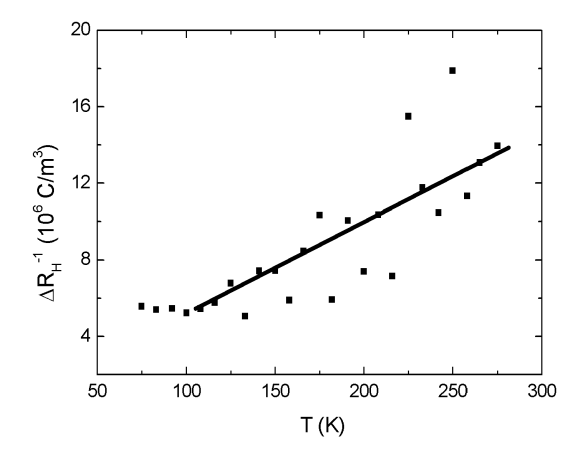


Figure 3.28: Difference in the inverse Hall constant between the two polarization states as a function of temperature. The solid line is the difference between the two fits shown in figure 3.24.

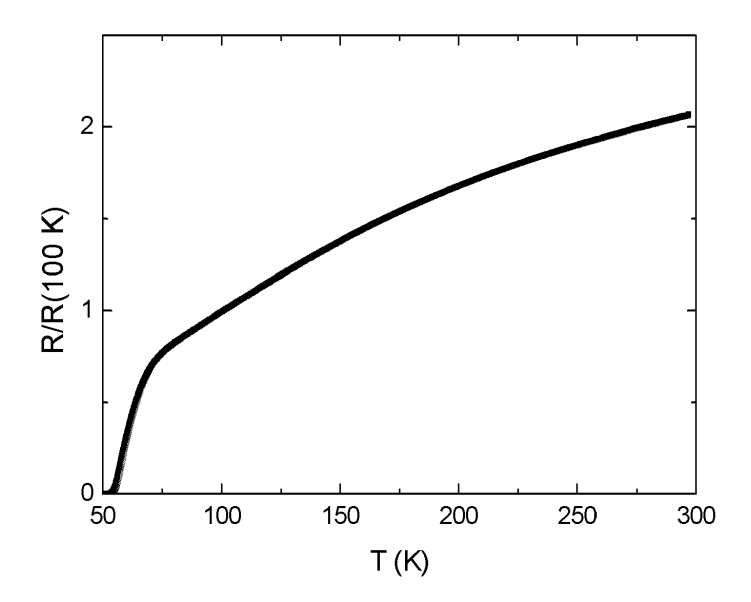


Figure 3.29: Resistivity curves versus temperature for the two polarization states normalized at 100 K.

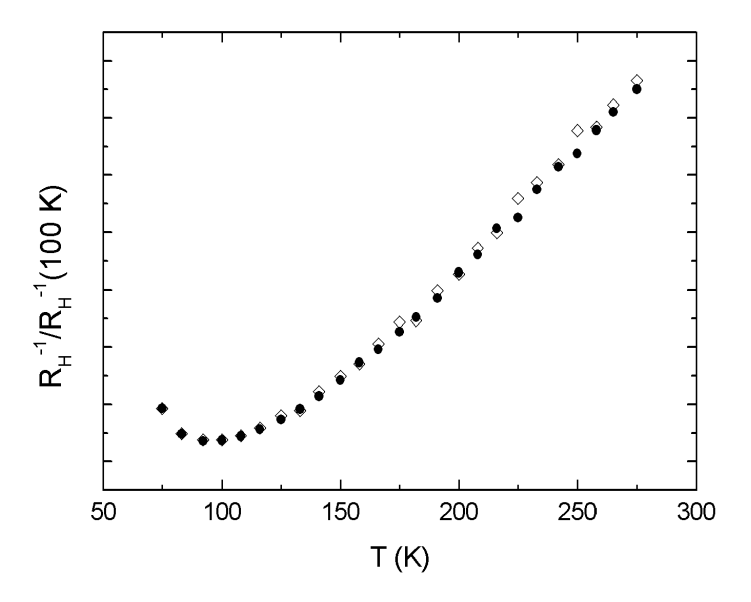


Figure 3.30: Inverse Hall constant curves versus temperature for the two polarization states normalized at 100 K.

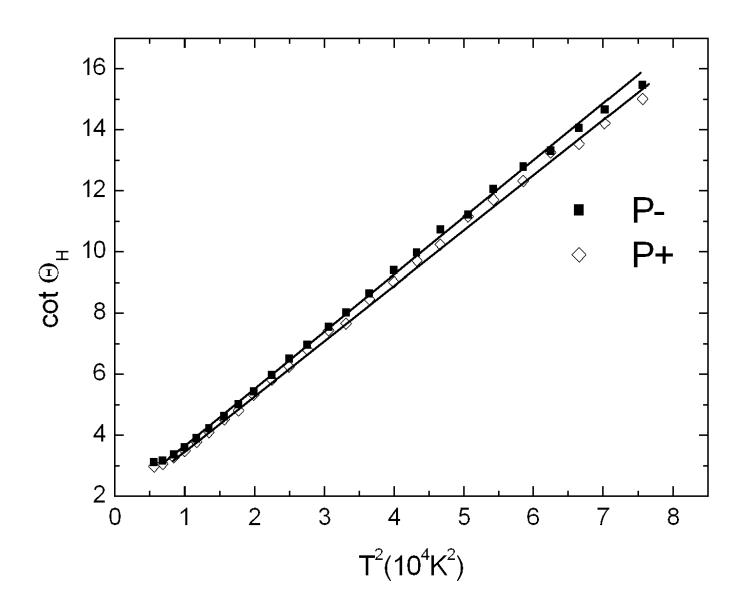


Figure 3.31: $\cot \theta_H$ as a function of T^2 for the two polarization states. The lines are a guide to the eye.

n unchanged.

Figure 3.31 shows the cotangent of the Hall angle, $\cot\Theta_H$ ($\cot\Theta_H = \rho_{xx}/\rho_{xy} = \rho_{xx}/BR_H$), as a function of temperature for the two polarization states. As observed by others for $REBa_2Cu_3O_7$ compounds [68], $\cot\Theta_H$ displays a T^2 temperature dependence down to 100 K, a result consistent with recent measurements on thin underdoped $GdBa_2Cu_3O_{7-\delta}$ films [86]. Upon polarization reversal, since the relative increase in resistivity (about 9%) does not equal the decrease in inverse Hall constant (about 6%), the cotangent of the Hall angle (essentially the product of these two quantities) should be affected by the polarization change. Although small, this effect can be observed in the data, in particular at high temperatures. In chemical doping experiments, the slope of $\cot\Theta_H$ versus T^2 generally decreases with decreasing doping levels [66,91]. In our experiments, we observe that decreasing the carrier density increases the slope of $\cot\Theta_H$. This difference could be linked to the absence of induced structural changes or disorder in our electrostatic modulation of n.

The difference observed between the relative change in ρ and R_H^{-1} is small but has been systematically observed in all the samples investigated. We note here that the Hirsch model predicts a difference in the relative change in ρ and R_H^{-1} due to a change in effective mass [92]. In the theoretical framework of Stojkovic and Pines, $\cot \Theta_H$ (proportional to $\rho * R_H^{-1}$) is equal to: $2m_{cold}/eB\tau_{cold}$. This formula depends only on τ_{cold} and m_{cold} (and not explicitly on the carrier density).

A possible explanation of the small difference observed between the cotangent of the Hall

angle for the two polarization states, about 3%, (and the difference in the relative change of ρ and R_H^{-1}) is that the effective mass m_{cold} is increased when the carrier concentration is lowered due to increased Coulomb interactions between the quasiparticles (since the system is closer to a Mott insulator), and/or that the magnetic fluctuations are stronger, leading to a smaller τ_{cold} ². Both effects lead to an increase of $\cot \Theta_H$.

In conclusion, our field effect data in the normal state, in particular the field modulation of the Hall response, suggest that the carrier concentration in cuprates is not temperature dependent. The temperature dependence of the inverse Hall constant observed experimentally might be related to the presence of two types of carriers with temperature dependent scattering times. In the superconducting state, we have succeeded in substantially modulating the critical temperature of ultrathin films and in the most extreme case we have induced a change from superconducting to insulating behavior although there zero resistance was not achieved in the "SC" state.

²While magnetic scattering affects mostly the hot parts of the Fermi surface, a small effect on the cold areas cannot be excluded.

Chapter 4

LaTiO $_{3+\delta}$ thin films: growth and transport properties

The study of LaTiO_{3+ δ} at the IBM Zürich Research Laboratory was originally motivated by the search for superconductivity. In fact, the discovery by Bednorz and Müller in 1986 [1] of high- T_c superconductivity in $Ba_xLa_{2-x}CuO_4$, a compound with a mixed valence state for a 3d element, generated extensive studies of this compound and related Cu-based compounds. These studies revealed that not only the mixed valence of Cu but also the layered structure of the compounds was central to high temperature superconductivity. This observation revived interest in other 3d elements, some of which were well-known to be superconducting but at considerably lower temperatures. In 1991 Lichtenberg et al. [29] reporting on the "Electronic and magnetic properties of the first layered conducting titanium and niobium oxides" wrote: "Three-dimensional titanium and niobium oxides are superconducting at temperatures considerably lower than layered copper oxides. Therefore it seems worthwhile to study layered titanium and niobium oxides." The complete phase diagram of LaTiO_{3+ δ} was subsequently unveiled [93] and presents various phases which possess different structural and physical properties depending on their actual oxygen stoichiometry. In fact, the perovskite LaTiO_{3+ δ} allows a very rich and flexible chemistry: the oxygen content can be changed from 3.0 to 3.5 while the formal titanium valency varies between +III to +IV. Starting with $\delta = 0$, LaTiO₃ is an antiferromagnetic Mott insulator with a 3D-distorted perovskite structure and becomes metallic with increasing oxygen content. For $\delta > 0.2$ semiconducting behavior is observed and for $\delta = 0.4$ the additional oxygen atoms order on an infinite {110} perovskite plane. For $\delta = 0.5$, periodic stacking of these planes with four perovskite blocks in between takes place. LaTiO_{3.5} is a ferroelectric phase with an extremely high critical temperature $(T_c=1773 \text{ K})$ [94] and a unique polarization axis in the {110} perovskite plane (parallel to the additional oxygen plane). Thus, if the insertion of the additional oxygen plane in LaTiO_{3+ δ} can be controlled, e.g. by the growth of a thin film, a multi layer system with an interesting chemical and structural compatibility could be fabricated.

We searched in the literature for a report on thin films of LaTiO_{3+ δ} but the published

research on the material has been performed on polycrystalline powders and single crystals. Only very recently work at Bell laboratories on superlattices based on LTO and STO [95,96] as well as work in Augsburg on epitaxial films of LTO has been reported [97]. At the IBM Zürich Research Laboratory, a molecular beam epitaxy (MBE) setup has been in operation for a number of years. The MBE technique allows the production of very high quality thin films with a layering that can be precisely controlled on an atomic scale. In collaboration with Dr. J.-P. Locquet, we started a project to grow and study the electronic properties of LTO thin films. In this project, Dr. J. W. Seo and Dr. J. Fompeyrine have studied the ferroelectric phase in detail, examining the growth and oxidation mechanism of LaTiO_{3.5} thin films [98,99], while we have focused our attention to the investigation of the transport properties of metallic thin films observed for a mixed valence state of Ti.

4.1 Growth of LaTiO_{3+ δ} thin films

Epitaxial thin films of LTO were prepared in a molecular beam epitaxy system, using a sequential deposition method. La and Ti were evaporated by an electron beam (e^- -beam) onto different substrates heated to 800° C and a deposition sequence of one La-O_x monolayer followed by one Ti-O_x monolayer was used.

High oxygen background pressure naturally favors the growth of oxygen-rich LaTiO $_{3+\delta}$. LaTiO $_{3.5}$ thin films were grown in a flow of atomic oxygen produced by a rf plasma source with a working pressure of 3 10^{-6} Torr on (110)-oriented SrTiO $_3$ (STO) substrates. This substrate orientation is the only one that allows epitaxial growth of single crystal LaTiO $_{3.5}$. The additional oxygen plane is then parallel to the interface and does not affect the inplane lattice mismatch. The growth mechanism has been studied in detail using reflection high energy electron diffraction (RHEED) and transmission electron microscopy (TEM). The results [98] indicate that the material grows in the perovskite structure for the first four perovskite unit cells. Afterwards a rearrangement takes place, leading to the insertion of an additional subsurface oxygen plane between the second and third unit cell.

To grow LTO films with a lower oxygen content, we reduced the molecular oxygen pressure to approximately 10^{-7} Torr and prepared thin films on (001)- and (110)-oriented LaAlO₃ and Cr-doped SrTiO₃ substrates [the Cr doping (5%) widening the band gap of SrTiO₃ keeps reduced (SrTiO_{3-x}) substrates insulating]. The resulting films had a 3D perovskite structure. Monitoring the in-plane lattice parameter by RHEED analysis during the growth, we noticed a relaxation/reorganization of the diffracted pattern after the growth of a few unit cells (usually at the fourth unit cell). The films clearly retain the perovkite structure of the substrate near the interface and the stoichiometric LaTiO₃ phase can be stabilized. After this interface layer, additional oxygen is inserted into the structure, driven energetically to achieve the equilibrium oxidative state of Ti.

Recently Ohtomo and coworkers [95,96] have grown SrTiO₃/LaTiO₃ superlattice films by pulsed laser deposition. They succeeded in stabilizing stoichiometric LaTiO₃ completely free of additional oxygen that otherwise orders on {110} planes due to the substrate choice

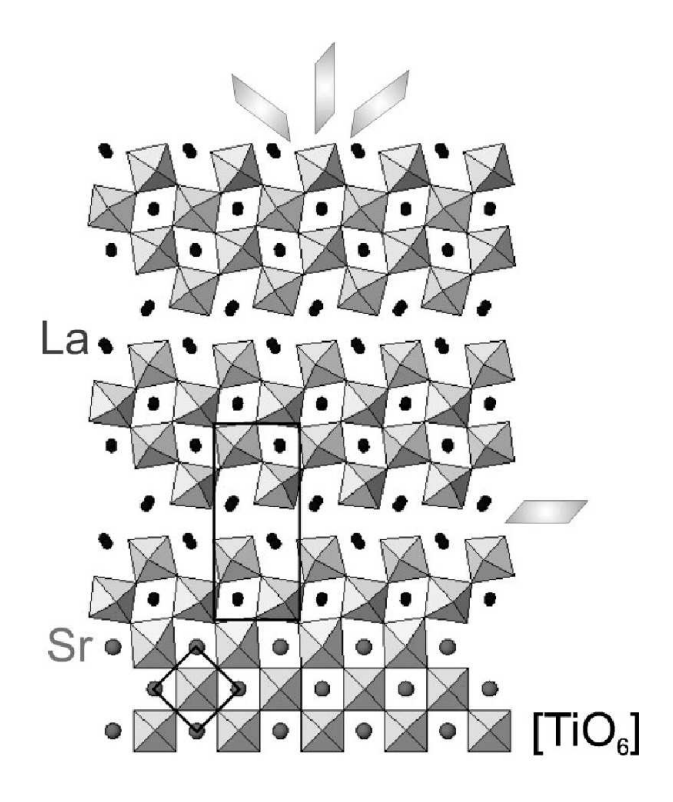


Figure 4.1: Schematic drawing of the epitaxial relationship between (110) STO and (100)-oriented LaTiO_{3.5} illustrated in a projection onto a plane perpendicular to the substrate surface. Filled circles indicate La and Sr atoms, while Ti atoms occupy the center of the $[TiO_6]$ octahedra. The four equivalent $\{110\}$ perovskite planes for oxygen insertion are indicated. [Figure from [99]]

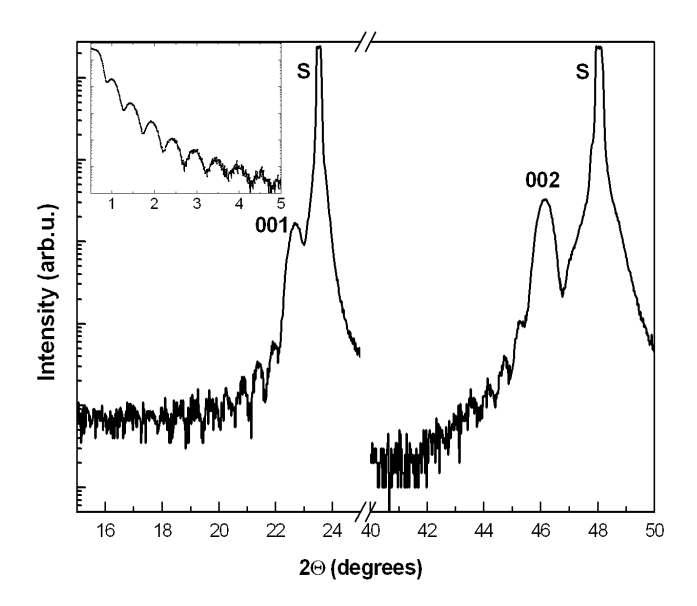


Figure 4.2: $\theta - 2\theta$ scan of a 20 nm thick LTO film grown on (001) LAO displaying finite size effect around (001) and (002) peaks. Inset: low angle oscillations indicative of the flat surface of the film.

by limiting to six the number of $LaTiO_3$ unit cells in each multilayer block. In their approach it is the kinematics of the deposition that constrain the Ti valence to +III, whereas in our approach it is the thermodynamics that determines the valence of Ti. In their work, the synthesis of stoichiometric $LaTiO_3$ thicker films proved to be impossible due to the extremely reducing conditions necessary to stabilize Ti^{3+} .

4.2 Structural analysis

Ex-situ $\theta-2\theta$ diffractograms of the films grown onto (001) LAO substrates can be indexed with (00l) reflections. Finite size effect oscillations around the (00l) peaks are observed, as shown in figure 4.2, indicative of good structural coherence throughout the film. Oscillations in the low angle scan suggest a flat surface confirmed by atomic force microscopy analyses which reveal a peak-to-valley height of about two unit cells and a root-mean-square (RMS) roughness of 0.4 nm.

LTO thin films have a mismatch of 4.7% with the LaAlO₃ substrate. The plan-view TEM image of a LTO thin film grown on (001) LAO, shown in figure 4.3, displays Moiré patterns which originate from the difference of the lattice spacing between substrate and film. The presence of Moiré patterns is therefore an indication that the film is fully (or almost fully) relaxed. The spacing of the Moiré pattern d_M is related to the lattice con-

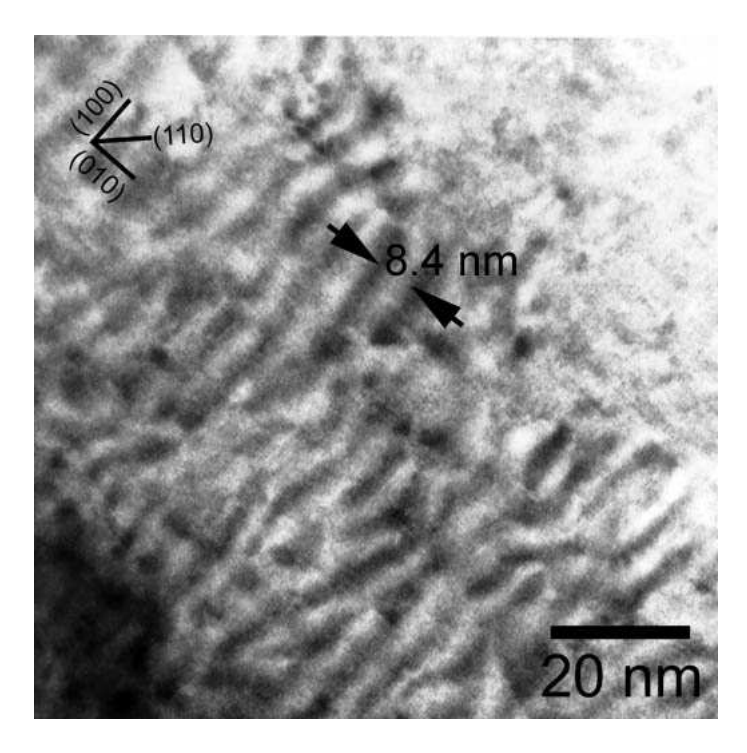


Figure 4.3: Plan-view TEM image of LTO on (001) LaAlO₃ substrate. The regular pattern on the image, called Moiré pattern, is due to the difference of the lattice spacing of the film and of the substrate. The scale is shown on the figure with the crystallographic axes.

stant of the substrate d_s and of the film d_f by the relation $d_M = (d_s - d_f)/(d_s + d_f)$. From the Moiré pattern spacing the lattice parameter of the film can then be derived to be approximately 0.394 nm, a value which agrees well with x-ray measurements performed on this film (0.392 nm).

For growth on Cr-doped SrTiO₃ (STO) substrates, the lattice mismatch with LTO is 1.7% and, as no Moiré patterns have been observed, it suggests that the film lattice is coherent with the substrate. The main difference between the films grown on LAO and STO is the presence of elongated structural defects, which can be seen in figure 4.4. The average spacing between defects is about 15 nm while their average length is about 10 nm. Their habit plane corresponds to the (110) and (1-10) planes of STO. The detailed structure of these films is rather complicated and will not be discussed here in its full complexity. We will only stress the important points which are relevant to "understand" the transport properties.

In figure 4.6, an enlarged image of the structural defect in the LTO thin film grown on (001) STO is shown. The line-scan (black line) across the defect reveals the variation of the (110) lattice spacing. Compared to the average (110) lattice spacing 0.394 nm * $\sqrt{2}$ = 0.557 nm, the lattice spacing in the area of the defect region has changed to 0.668 nm. Due to this enormous change of lattice spacing (16%) the film is strongly distorted. This is particularly clear around the start and end point of the defect where the lattice fringes

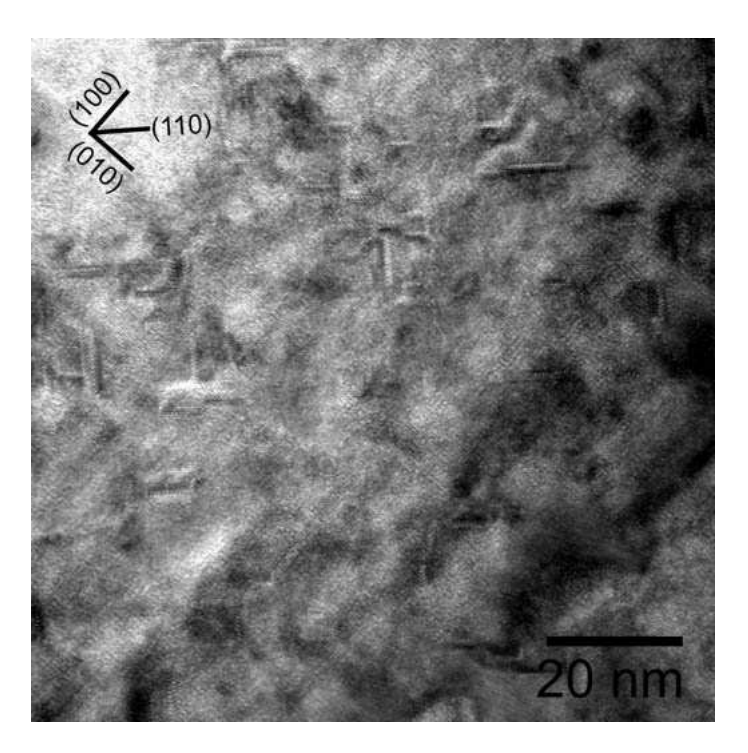


Figure 4.4: Plan-view TEM image of LTO on a (001) SrTiO₃ substrate. The defects, due to an inclusion of oxygen to accommodate the Ti valence, are visible because of their elongated structure. The crystallographic axes with the scale are shown on the figure.

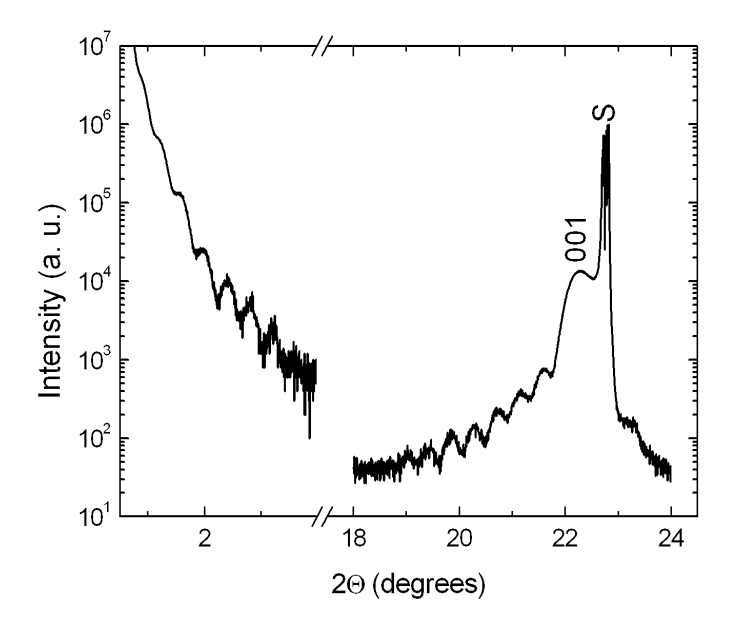


Figure 4.5: $\theta - 2\theta$ scan of a 20 nm thick LTO film grown on (001) STO. Finite size oscillations around the (001) peak reveal the good crystalline quality of the film.

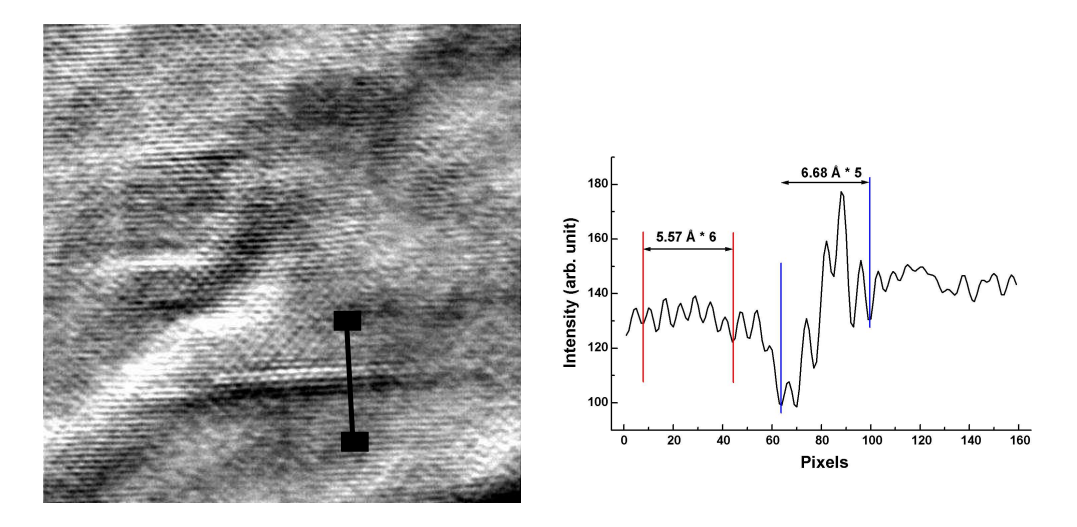


Figure 4.6: (left) Enlarged image of an elongated structural defect present in a LTO film grown on $SrTiO_3$. (right) Line-scan performed along the black line revealing the different lattice spacing for the "normal" and the defect region.

are strongly bent. From the line-scan in figure 4.6, the derived (110) lattice spacing within the defect (0.668 nm) is close to half the long a-axis of the LaTiO_{3.5} structure (0.64 nm). Hence, the lattice spacing and the habit plane results point to the intergrowth of a LaTiO_{3.5} crystallite inside the metallic LaTiO_{3+ δ} thin film.

Why do LaTiO_{3.5} crystallites appear in films grown on STO while they are absent in films grown on LAO substrates, especially as the oxygen pressure and substrate temperature are identical for all substrates during the growth? Of the substrates used, only STO is known to lose oxygen at high temperatures. For instance, after a half hour annealing in vacuum at 800°C the oxygen content of a STO substrate decreases from 3 to about 2.97. This observation suggests that the substrate can function as a large oxygen reservoir.

The STO substrate is also the only one to induce a coherent growth of the LTO thin film. Hence the insertion of the additional oxygen to accommodate the Ti valence develops along different mechanisms on STO than for thin films grown on LAO and could energetically favor a phase separation.

4.3 Transport properties for films prepared on (001) LAO substrates

We start the discussion of the transport properties with the films grown on LAO for which a clear physical picture of the conduction mechanism emerges. We will see that the properties of films prepared on STO are quite different and lead to more speculative interpretations.

For all the films, the transport properties have been studied in detail on patterned samples. Resistivity and Hall effect paths were prepared by lithographic processing and dry etching as described in section 2.3. For samples grown on LAO in low oxygen pressure ($P \le 10^{-8}$ Torr), a semiconducting behavior over the entire temperature range was observed. A temperature dependence analysis of the conduction mechanism suggests a thermally actived resistivity at high temperatures and a variable range hopping behavior at low temperatures. In polycrystalline $\text{La}_{1-x}\text{Sr}_x\text{TiO}_3$ specimens, Hays $et\ al.\ [100]$ report that in the range $x \le 0.025$ the resistance is well described by the thermal activation expression over the range $90\ \text{K} < T < 300\ \text{K}$. This behavior points to a localization of the carriers in the Mott insulating region, as previously observed, also in LaTiO_3 single crystals, by Crandles $et\ al.\ [101]$.

Samples grown at higher oxygen pressure (P in the range of 10^{-7} Torr) display a metallic behavior at room temperature. To quantify the doping level of the films we measured the Hall effect as a function of temperature to obtain the carrier density. Tokura $et\ al$. [4] have shown that the carrier density can be related to the doping level and thus to the Ti valence. In $La_{1-x}Sr_xTiO_3$ (LSTO) single crystals they observed a linear relation between the doping level and the carrier density up to the vicinity of the Mott insulator.

Figure 4.7 shows a characteristic result for the Hall constant R_H as a function of tem-

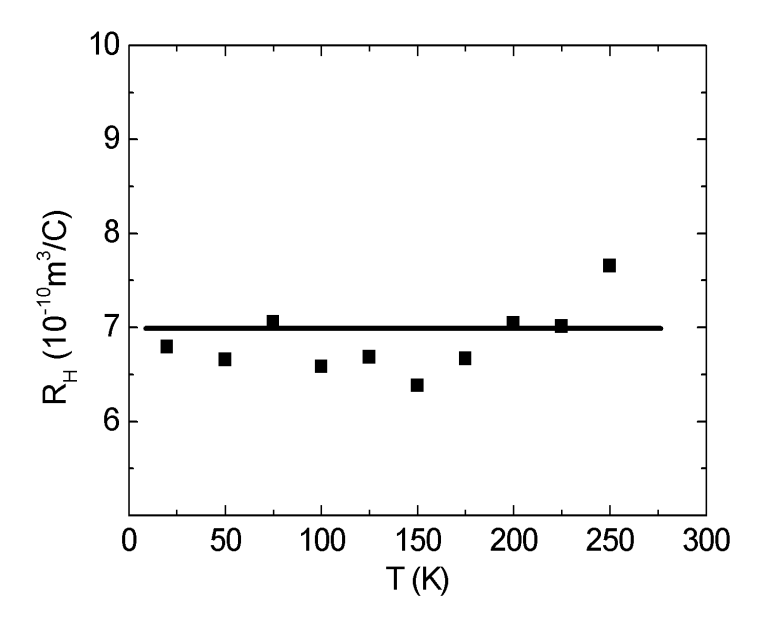


Figure 4.7: Hall coefficient of a LTO 22 nm thick film as a function of temperature. Using the free electron formula one finds a carrier density of $n=10^{22}$ cm⁻³.

perature in the range where metallic transport is observed. As can be seen from the data, the Hall constant is essentially independent of temperature with a sign corresponding to electrons as charge carriers. Using the standard free carrier Hall effect formula $R_H^{-1} = ne$, where e is the electron charge, and n the carrier density, one finds that the metallic films typically have a carrier concentration of between 5-12 10^{21} electrons per cubic centimeter, corresponding to a doping level of x^* =0.3-0.7 [x^* =Ti³⁺/(Ti³⁺+Ti⁴⁺)], typically in between the band and Mott insulator.

Figure 4.8 shows the resistivity ρ as a function of temperature for a LTO thin film 25 nm thick, with a carrier concentration of 1.2 10^{22} cm⁻³, plotted between 4 K and 600 K. At low temperatures, a metal-insulator transition is systematically observed: below a characteristic temperature T_{M-I} , the resistivity increases as the temperature is reduced. Searching for superconductivity in Ti metal oxides has been the subject of intense research as demonstrated by the large number of papers present in the literature. To our knowledge, none of these investigations have been carried out below 4 K on LTO. On our more metallic samples (T_{M-I} <4 K) we thus performed resistivity measurements in a dilution cryostat down to 15 mK: no superconductivity, however, was found. Rather, the resistivity increases as the temperature is reduced, as shown in the inset of figure 4.8, suggesting an insulating ground state.

At higher temperatures, the resistivity is roughly proportional to T^2 up to room temperature. To better investigate the extension in temperature of this conduction mechanism, we developed a set-up allowing the measurement of the resistivity at high temperatures.

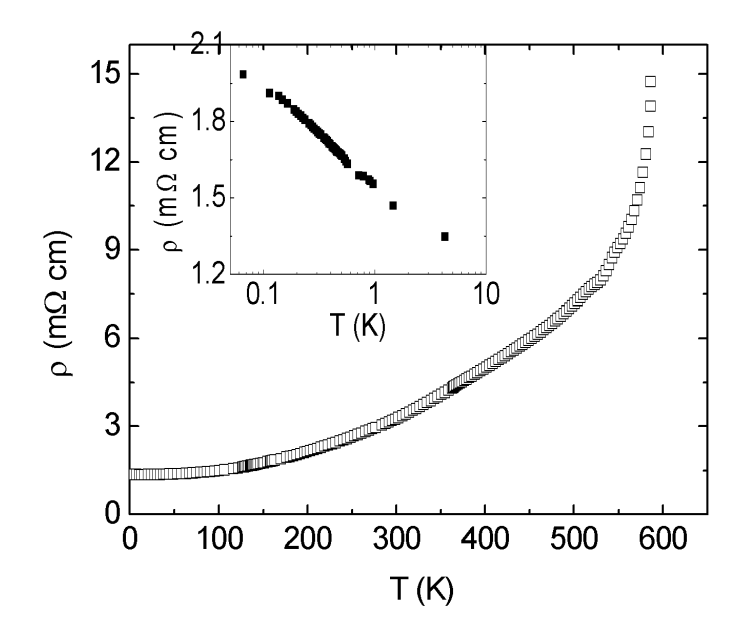


Figure 4.8: Resistivity of a LTO thin film as a function of temperature. A steep increase of resistivity at high temperatures and a following irreversibility in the cooling suggests a change in the film above 550 K.

Above room temperature the measurements were performed in oxygen flow up to 600 K. Above 550 K, the resistivity behavior changes dramatically and ρ increases steeply as the temperature increases. This high temperature increase of the resistivity is not reversible. We believe that at these high temperatures a compositional/structural change takes place in the film, since successive x-ray analysis did not reveal any peak from the layer. Surprisingly, the resistivity is still proportional to T^2 up to 500 K.

4.3.1 Transport mechanism

The T^2 resistivity behavior observed in the metallic region has often been taken to be a result of strong electron-electron correlations originating from the proximity to the Mott insulating state. This thesis has been supported by Tokura and coworkers who have studied in details the electronic properties close to the metal-Mott insulator transition. The behavior of the resistivity with a T^2 temperature dependence up to room temperature, as well as an increase in the carrier mass m^* as the transition is approached, are, at first sight, strong elements pointing to a Fermi liquid with enhanced electron-electron correlations and suggesting that the Fermi liquid picture may be applied up to the verge of the metal-insulator transition.

The theoretical description of the enhancement of m^* with band filling in strongly correlated electron systems has been originally proposed by Hubbard [20,21] and later restated

by Brinkman and Rice [102].

Fermi liquid theory asserts that the ground state and low-energy excitations can be described by an adiabatic switching on of the electron-electron interaction. Then, naively, the carrier number does not change in the adiabatic process of introducing the electron correlations, as demonstrated by the Luttinger theorem. Because the Mott insulator is realized for a partially filled band, this adiabatic continuation forces the carrier density to remain nonzero when one approaches the metal-insulator transition point in the framework of Fermi-liquid theory. In this case, the only way to approach the transition in a continuous fashion is the divergence of the single-quasiparticle mass m^* at the metal-insulator transition point. Therefore mass enhancement in metals near the Mott insulator is a natural consequence of the Fermi-liquid picture.

Although the theoretical picture presented by Tokura for LSTO has strong experimental arguments on its side, there are other puzzling experimental observations that do not fit this theoretical picture. First, the temperature range over which the T^2 behavior of resistivity is observed is very large as compared to what is observed in transition metals or heavy fermion compounds (in transition metals the T^2 behavior is observed at most up to 20 K) [103]. Also, the empirical relation $A \propto \gamma^2$, A being the coefficient of the T^2 term in the resistivity and γ the specific heat coefficient, usually observed in metals with strong correlations and in particular in heavy fermion systems, has been reported to hold well approaching the Mott insulator. However, the A/γ^2 value reported for LSTO is much larger than what is observed in transition metals exhibiting a T^2 behavior. It is also striking that the T^2 behavior of the resistivity is in fact observed more clearly for x^* =0.5, far from the metal-insulator transition, where the carrier effective mass is not strongly enhanced and the electronic correlations substantially reduced.

Fujomori et al. [104] in 1992 have studied the electronic structure of LSTO as a function of the doping level in photoemission experiments. They reported that the experimental results are incompatible with the rigid-band behavior predicted by one-electron band theory and also by Hubbard model calculations. An interesting peak, 1.5 eV below the Fermi level, was observed in the photoemission spectra. This feature, not predicted by band theory and tentatively attributed to the lower Hubbard band, had a maximum intensity for LaTiO₃ but did not disappear or shift even at high doping levels (La_{0.1}Sr_{0.9}TiO₃): a result, as pointed out by the authors, difficult to understand, since the short-range Coulomb repulsion should become less important far from the Mott insulator and band theory should be recovered. In 1996, the same group [7] interpreted its photoemission data, and in particular the 1.5 eV peak as a signature of strong electron-phonon interactions present in the compound. A detailed analysis of the energy peak considering short and long range interactions of electrons with the lattice suggests a polaronic nature for the charge carriers. The resulting polaron radius is rather small, 0.27 nm, consistent with the high carrier concentration of these materials. In this model, a doped electron is self-trapped due to the polaronic effect, with a small binding energy (and hence a small transport activation energy) but, when the electron is emitted in the photoemission process, the lattice is left with a large excess energy of ~ 1 eV, giving rise to the deep d-derived photoemission peak. Within this model with the tendency for carriers of self-trapping, one is left to explain the observed metallic transport.

The resistivity behavior observed in figure 4.8, however, can also be understood if polaronic transport is considered. The localization of electrons at regular lattice sites (polaron formation) does not remove them from the conductivity processes, although it does impart some specific features to them. The idea of a self-localization of an electron at a regular site has much in common with the idea of conductivity by means of a change in valency of lattice sites.

As described for crystalline semiconductors [105], there are three different transport regimes for polarons. At low temperatures, the electrons are bound and an activated resistivity is observed (ρ decreases as T increases). At higher temperatures, a polaronic band is formed and a small polaron metallic transport is observed. Above $1/2\Theta_D$, where Θ_D is the Debye temperature, the mean free path is smaller than the lattice spacing and hopping conduction should be observed, where ρ decreases again as T increases. The data in figure 4.8 are consistent with this scenario assuming that the latter hopping high temperature regime cannot be observed because of the changes in oxygen stoichiometry, as discussed previously.

To better understand whether the observed behavior is related to polaronic transport, we focused our attention on the "metallic" region which extends over a temperature range that is large enough to perform a detailed fit to the data. For polaronic transport in the metallic regime [5] the Hall constant should take the form:

$$R_H = \frac{\gamma}{en} \tag{4.1}$$

where e is the electron charge, n the carrier density, and γ a temperature independent constant close to 1, implying that the Hall constant is essentially probing the carrier concentration.

If small polaronic metallic conduction is considered, the resistivity should take the form

$$\rho(T) = (\hbar^2/ne^2 a^2 t_p) \frac{A}{\sinh^2(\hbar\omega_o/2k_B T)}$$
(4.2)

assuming only one low lying optical mode ω_o with strong electron phonon coupling. In the above formula, a is the lattice constant, A is a constant depending on the electron-phonon coupling strength and t_p is the hopping integral of polarons. Figure 4.9 shows the resistivity as a function of temperature between 4 K and 300 K. The line on the figure is a fit to:

$$\rho(T) = \rho_o + C/\sinh^2(\hbar\omega_o/2k_B T) \tag{4.3}$$

As can be seen, the fit is excellent with ρ_o =0.20 m Ω cm, C=2.3 $\mu\Omega$ cm, and $\hbar\omega_o/k_B$ =80 K. Although we show only the fit between 4 K and 300 K, we obtained a fit of similar quality between 4 K and 500 K.

The phonon frequency obtained from the fit can be compared with phonon measurements in Raman spectroscopy performed on this compound. Raman measurements performed

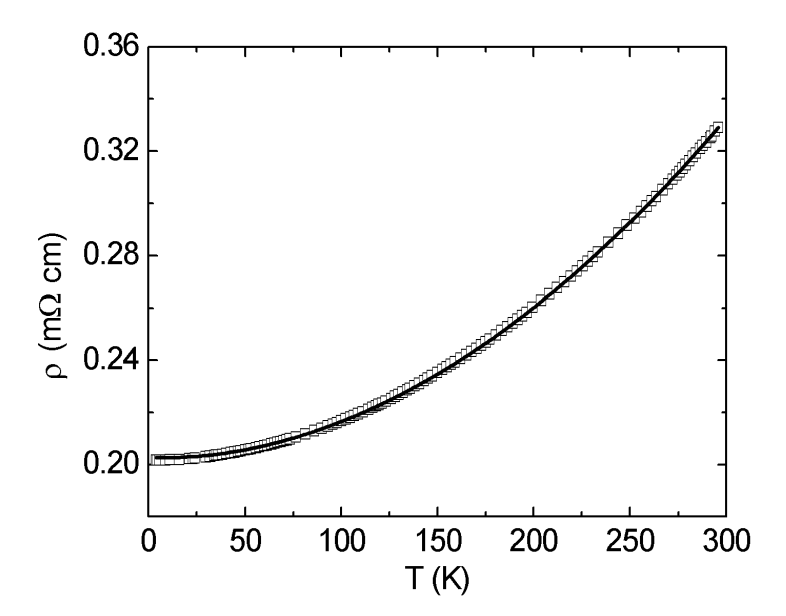


Figure 4.9: Resistivity of a LTO thin film as a function of temperature. The continuous line is a fit of the resistivity to a polaronic conduction mechanism.

on LaTiO₃ [6] give clear evidence of the existence of a soft mode at an energy of about 100 K, thus substantially reinforcing our interpretation of the resistivity data. This soft mode seems to be characteristic of a tilt/rotation of the oxygen octahedra and is present in different perovkite materials.

Our analysis of the transport properties in terms of polaronic conduction presented above was initially motivated by the work of Zhao $et\ al.$ on manganites [106, 107]. Analyzing the temperature dependence of the resistivity in $\text{La}_{1-x}\text{Ca}_x\text{MnO}_3$ below 100 K, they have proposed that their experimental resistivity data can be understood if small polaronic transport is the dominant conduction mechanism in these materials (however the situation in manganites is slightly more complicated since the magnon contribution to the resistivity cannot be neglected). We note here the interesting fact that the phonon frequency obtained from the fit to the manganite resistivity is $\hbar\omega_o=80$ K, a value very close to the one extracted from our fit in LTO. This similarity in the transport properties of metallic perovskite systems, due to the existence of a soft phonon mode, seems intimately related to the structure of the perovskites.

The body of data on LTO films prepared on LAO thus suggests that the physics in this system, in the composition range investigated, is dominated by electron-phonon interactions and not by electron-electron correlations as originally proposed.

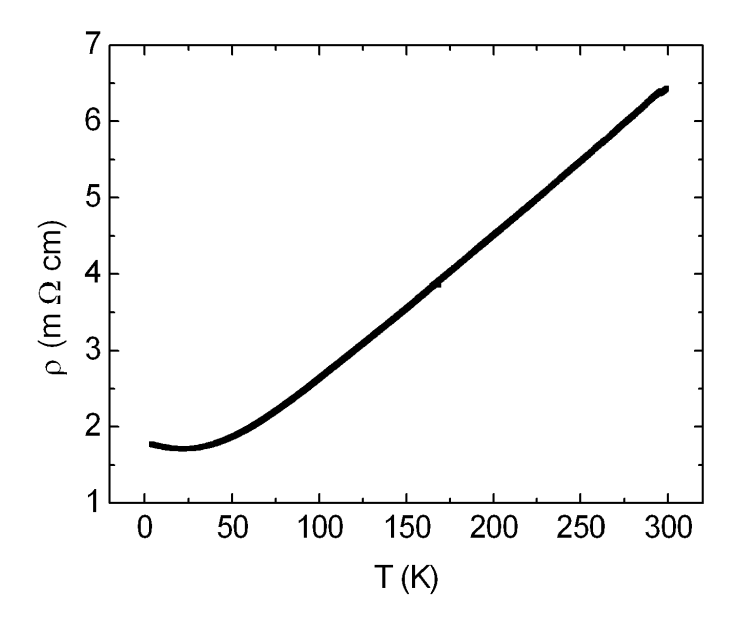


Figure 4.10: Resistivity of a LTO thin film grown on (001) STO as a function of temperature.

4.4 Films prepared on (001) STO substrates

Transport measurements on lithographically patterned samples grown on (001) Cr-doped $SrTiO_3$ substrates display very different behavior from the one of the samples prepared on LAO substates discussed above. What is systematically observed is a metallic behavior above a certain metal-insulator transition temperature (T_{M-I}) occurring at low temperatures. Measurements of the temperature dependence of the resistivity down to 15 mK have been performed without signs of superconductivity. In the metallic regime, the resistivity is linear in temperature, as shown in figure 4.10.

Other studies have already reported a linear temperature dependence of the resistivity in bulk samples with a Ti nominal valence of ~ 3.6 . Sunstrom et~al.~[108] reported metallic resistivity data with linear temperature dependence in the compound $\text{La}_{1-x}\text{Sr}_x\text{TiO}_3$ in the composition range $0.4 \leq x \leq 0.7$. MacEachern et~al.~[109], investigating the structure and electronic properties of $\text{La}_{1-x}\text{TiO}_3$ specimens, observed a linear temperature dependence of the resistivity for the composition $\text{La}_{0.8}\text{TiO}_3$, corresponding to a $x^*=0.6$ (in this system La vacancies self-organize in a regular structure).

While there is some disagreement between reports on the same nominal composition exhibiting different temperature dependence of the resistivity (for instance compare Sunstrom's data with Tokura's ones), our Hall effect data, discussed below, stand alone, differing strongly from the existing published results.

Figure 4.11 displays the inverse Hall constant as a function of temperature. The in-

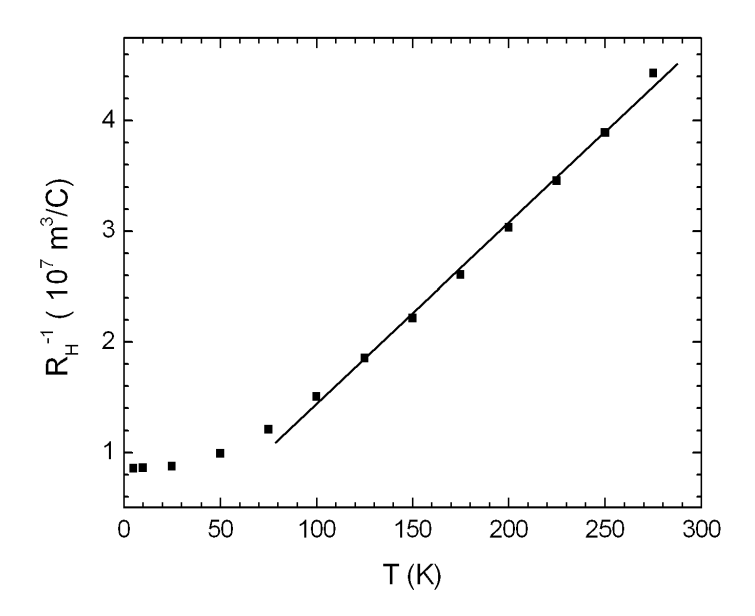


Figure 4.11: Inverse Hall constant of a LTO thin film grown on (001) STO as a function of temperature

verse Hall coefficient has a linear temperature dependence $R_H^{-1} \approx T$ down to T_{M-I} and a negative sign, corresponding to electron doping. We note that these transport properties are very similar to the ones displayed by high-temperature superconductors in the normal state.

The detailed analysis of the structural differences between LTO films grown on LAO and STO has revealed the presence of elongated structural defects. These defects are due to the intergrowth of LaTiO $_{3.5}$ crystallites inside the metallic LaTiO $_{3+\delta}$ thin film. One interesting possibility we would like to explore is that the films prepared on STO show a "patchwork" of the two different types of insulator (LaTiO $_3$ and LaTiO $_{3.5}$). At the interfaces between these insulators a 2D-like conduction might develop, eventually leading to transport properties similar to anisotropic high T_c superconductors. In collaboration with Dr. O. Kuffer, we recently tried to study such films by scanning tunneling spectroscopy to determine the local electronic structure and thus test this scenario. The film surfaces were found to be too insulating, preventing tunneling between the tip and the film; an oxidation surface layer can be the origin of this problem, as it is often observed in oxide thin films. The understanding of the difference between the behavior of films prepared on LAO and STO and also the origin of the anomalous transport properties observed on STO remains a stimulating subject since it could shed some light on the electronic properties of the normal state of cuprate superconductors.

Conclusions

In 1937 Peierls' observations, pointing out the importance of electron-electron correlation in transition-metal oxides, launched a wave of research in the field of strongly correlated electron systems. Until the 80's researchers investigated the role played by electronic correlations to drive a system from a metallic to an insulating state and/or from a paramagnetic to a ferro/antiferro-magnetic state in binary transition-metal compounds tuning external parameters such as temperature, pressure, magnetic field, or internal parameters such as doping or disorder.

In 1986 the revolutionary discovery by Bednorz and Müller of superconductivity in a ternary compound (La₂CuO₄), where the valence state of Cu could be tuned by chemical substitution over a wide range, opened a new avenue of research: band filling tunability by chemical doping in transition-metal oxides. Today, in compounds with perovskite structure, chemical doping allows researchers to explore new phase diagrams and to discover new electronic phases.

This thesis has developed in the large field of strongly correlated electron systems, exploring the role of electronic correlations using transport properties.

In this context, the field effect approach in cuprate superconductors has allowed us to electrostatically change the doping level in ultrathin layers, resulting in a purely band filling control of the material. This technique has been previously pursued to induce changes in the superconducting properties (T_c , critical current) of $H-T_c$ compounds, demonstrating its potential for applications both in basic science and in technological devices. In this study we have modulated the superconducting properties inducing a shift of the critical temperature and, in the most extreme case, obtained a superconductor-insulator transition. In these experiments we have also accessed the insulating state for the first time trough purely electrostatic hole doping: transport measurement analysis suggests that this field-induced insulating state is different from the one obtained by chemical doping.

Moreover, the use of the field effect to modulate the doping level in a controlled way has allowed us to address the fundamental issue of the carrier concentration contribution to the longitudinal and transverse conductivity of high-temperature superconductors. Our field effect data suggest that the resistivity and Hall constant are inversely proportional to a temperature independent carrier concentration.

Strongly correlated electron systems have for a long time meant exclusively electronelectron correlations (both charge and spin interactions). With the discovery of $H - T_c$, it 78 Conclusions

has been suggested that the properties of cuprate oxides can be explained by considering electrons strongly interacting with the lattice, leading to polaron formation. Recently, an interpretation of the properties of manganite oxides taking into account the polaron contribution has been proposed.

Following these footmarks, we have analyzed the transport properties of $LaTiO_{3+\delta}$ thin films, in particular the temperature dependence of the resistivity. These analyses seem to indicate that the conduction in this material has a polaronic nature and allow us to propose a scenario reconciling our transport measurements with the photoemission data obtained on this compound.

To conclude with some perspectives, it is clear that the ferroelectric field effect explored in this work has the potential to be used in the future on a nanoscopic scale. Using atomic force microscopy to control and modify the ferroelectric domain structure will lead to the very challenging realization of nanoscopic electronic features. This work is in development in the group.

Regarding the $\text{LaTiO}_{3+\delta}$ system, we did not fully explore the possibility of realizing artificial structures exploiting the rich $\text{LaTiO}_{3+\delta}$ phase diagram. Developments in this direction or more generally in the direction of the construction of "artificial" materials based on perovskite building blocks are certainly fascinating. Such developments, recently started in the group, are actively pursued worldwide.

Acknowledgements Remerciements

Je remercie le professeur Jean-Marc Triscone tout d'abord de m'avoir proposé un travail de thèse dans son groupe, et ensuite pour les discussions que nous avons eues pendant cette période. Les idées et les suggestions qu'il m'a apportées sont le témoignage de son amitié et de l'intérêt qu'il a porté à ma recherche.

J'exprime mes sincères remerciements à l'égard de tous les membres du jury: Professeur K. Alex Müller, Professeur Øystein Fischer, Docteur Jean-Pierre Locquet et Docteur Jean Fompeyrine.

Je désire exprimer ma reconnaisance particulière envers Charles Ahn pour le partage de ses connaisances dans l'activité de recherche, pour les discussions scientifiques, et surtout pour son amitié.

Par la chaleureuse ambiance qu'il a répandu au sein du groupe, Thomas Tybell a été d'une aide précieuse aucours des premièrs mois, toujours difficiles, de ce travail.

Au cours de ma thèse j'ai partagé beaucoup de mon temps de recherche avec Daniel Matthey: son amitié et notre confrontation scientifique continue ont été bénéfiques pour l'avancement de ma thèse.

Dans la collaboration avec IBM Rüschlikon dont cette thèse est une expression, les connaisances, l'amitié et le soutien de Jean-Pierre Locquet, Jean Fompeyrine et Maria Seo ont contribué à ma formation et au bon déroulement de ma recherche.

Au sein du DPMC, j'ai bénéficié du contact très enrichissant avec les autres expérimentateurs, ce qui m'a donné la chance de pouvoir me confronter à plusieurs approches de la physique du solide. Je les remercie tous pour leur aide et leur disponibilité, valeurs precieuses de ce département. Je tiens à remercier particulièrement:

Louis Antognazza, Edmond Koller, Serge Reymond, Pascal Reinert, les expertes en couches minces:

Patrycja Paruch pour ses connaisances en microscopie à force atomique et pour sa lecture attentive du manuscrit;

Ketty Beneduce et Daniele Marré pour la saveur de l'Italie qu'ils ont amenée pendant mon séjeur à Genève;

les membres du groupe STM pour tous les bons moments passés à discuter ensemble: Ivan Maggio-Aprile, Olivier Kuffer et Martin Kugler;

Daniel Chablaix pour son aide technique lors des divers développements;

Patrick Magnin qui m'a aidé à résoudre les problèmes d'informatique et avec lequel j'ai partagé aussi ma passion pour Linux.

Une de mes pensées s'adresse aussi aux secrétaires de notre département, Elisabeth Jeantin et Anne-Lise Pidoux pour leur aide et leur disponibilité.

Merci également à tous les membres de l'atelier de mécanique, á Spiros Zanos et Edouard Pérréard pour leur aide technique.

Ce travail a bénéficié du soutien financier du Fonds National Suisse de la Recherche Scientifique.

```
[1] J. G. Bednorz and K. A. Müller, Z. Phys. B 64, 189 (1986). viii, 11, 61
 [2] C. H. Ahn, T. Tybell, L. Antognazza, K. Char, R. Hammond, M. R. Beasley, Ø. Fischer, and J.-M.
     Triscone, Science 276, 1100 (1997). viii, 31, 50
 [3] R. Aidam, D. Fuchs, and R. Schneider, Physica C 328, 21 (1999). xiv, 39, 56, 57
 [4] Y. Tokura, Y. Taguchi, Y. Okada, Y. Fujishima, T. Arima, K. Kumagai, and Y. Iye, Phys. Rev. Lett.
     70, 2126 (1993). xv, 15, 68
 [5] V. N. Bogomolov, E. K. Kudinov, and Y. A. Firsov, Sov. Phys. - Solid State 9, 2502 (1968). xvi, 72
 [6] M. Reedyk, D. A. Crandles, M. Cardona, J. D. Garrett, and J. E. Greedan, Phys. Rev. B 55, 1442
     (1997). xvi, 73
 [7] A. Fujimori, A. Bocquet, K. Morikawa, K. Kobayashi, T. Saitoh, Y. Tokura, I. Hase, and M. Onoda,
     J. Phys. Chem. Solids 57, 1379 (1996). xvii, 71
 [8] P. Drude, Annalen der Physik 1, 566 (1900). 5
 [9] P. Drude, Annalen der Physik 3, 369 (1900). 5
[10] H. Bethe, Ann. Phys. (Leipzig) 87, 55 (1928). 5
[11] F. Bloch, Z. Phys. 57, 545 (1929). 5
[12] A. Sommerfeld, Z. Phys. 47, 1 (1928). 5
[13] A. H. Wilson, Proc. Phys. Soc. London, Ser. A 133, 458 (1931). 5
[14] A. H. Wilson, Proc. Phys. Soc. London, Ser. A 134, 277 (1931). 5
[15] N. Mott, Proc. Phys. Soc. London, Ser. A 62, 416 (1949). 6
[16] N. Mott, Metal-Insulator Transitions (Taylor&Francis, London, 1990). 6, 11, 46
[17] J. C. Slater, Phys. Rev. 82, 538 (1951). 6, 8
[18] P. W. Anderson, Phys. Rev. 115, 2 (1959). 6
[19] J. Hubbard, Proc. Phys. Soc. London, Ser. A 276, 238 (1963). 6
[20] J. Hubbard, Proc. Phys. Soc. London, Ser. A 277, 237 (1964). 6, 70
[21] J. Hubbard, Proc. Phys. Soc. London, Ser. A 281, 401 (1964). 6, 70
[22] J. Zaanen, G. A. Sawatzky, and J. W. Allen, Phys. Rev. Lett. 55, 418 (1985). 8
[23] D. H. Martin, Magnetism in Solids (Iliffe Books LTD, London, 1967). 9
```

[24] A. S. Alexandrov and N. Mott, *Polarons and Bipolarons* (World Scientific, Singapore, 1995). 11

[25] J. R. Waldram, Superconductivity of Metals and Cuprates (IOP, Bristol, 1996). 12

- [26] J. Rossat-Mignod and et al., Physica B **169**, 58 (1991). 13
- [27] M. Takigawa, A. P. Reyes, P. C. Hammel, J. D. Thompson, R. H. Heffner, Z. Fisk, and K. C. Ott, Phys. Rev. B **39**, 300 (1991). 13
- [28] T. Timusk and B. Statt, Rep. Prog. Phys. 62, 61 (1999). 13, 27
- [29] F. Lichtenberg, D. Widmer, J. G. Bednorz, T. Williams, and A. Reller, Z. Phys. B 82, 211 (1991). 15, 61
- [30] J.-M. Triscone, M. G. Karkut, L. Antognazza, O. Brunner, and Ø. Fischer, Phys. Rev. Lett. 63, 1016 (1989). 17
- [31] J.-M. Triscone, Ø. Fischer, O. Brunner, L. Antognazza, A. D. Kent, and M. G. Karkut, Phys. Rev. Lett. 64, 804 (1990). 17
- [32] O. Brunner, L. Antognazza, J.-M. Triscone, L. Miéville, and Ø. Fischer, Phys. Rev. Lett. 67, 1354 (1991). 17
- [33] J.-M. Triscone, L. Frauchiger, M. Decroux, L. Mieville, Ø. Fischer, C. Beeli, P. Stadelmann, and G.-A. Racine, J. Appl. Phys. **79**, 4298 (1996). 17, 37, 38
- [34] D. L. Smith, *Thin-film deposition* (Mc Graw-Hill, Inc., International edition, 1995). 18
- [35] B. Chapman, Glow discharge processes, sputtering and plasma etching (John Wiley & Sons, New York, 1980). 18
- [36] C. B. Eom, Ph.D. thesis, Standford University, 1991. 19
- [37] C. B. Eom, J. Z. Sun, B. M. Lairson, S. K. Streiffer, A. F. Marshall, K. Yamamoto, S. M. Anlage, J. C. Bravman, T. H. Geballe, S. S. Laderman, R. C. Taber, and R. D. Jacowitz, Physica C 171, 354 (1990). 19
- [38] A. Daridon, Ph.D. thesis, Universität Bern, Switzerland, 1998. 19, 20
- [39] J.-P. Locquet, Y. Jaccard, C. Gerber, and E. Mächler, Appl. Phys. Lett. 63, 1426 (1993). 20
- [40] P. Scherrer, Gött. Nachr. 2, 98 (1918). 21
- [41] A. Guinier, Radiocristallographie (Dunod, 29, 1945). 21
- [42] E. Koller, Ph.D. thesis, DPMC, University of Geneva, 1997. 22
- [43] L. G. Parratt, Phys. Rev. 95, 359 (1954). 22
- [44] P. F. Fewster, Rep. Prog. Phys. 59, 1339 (1996). 22
- [45] V. Holy, U. Pietsch, and T. Baumbach, *High-resolution x-ray scattering from thin films and multilay-ers* (Springer, International edition, 1998). 22
- [46] R. E. Glover and M. D. Sherrill, Phys. Rev. Lett. 5, 248 (1960). 25
- [47] J. Mannhart, D. G. Schlom, J. G. Bednorz, and K. A. Müller, Phys. Rev. Lett. 67, 2099 (91). 25
- [48] X. X. Xi, Q. Li, C. Doughty, C. Kwon, S. Bhattacharya, A. T. Findikoglu, and T. Venkatesan, Appl. Phys. Lett. **59**, 3470 (1991). 25
- [49] A. Walkenhorst, C. Doughty, X. X. Xi, Q. Li, C. J. Lobb, S. N. Mao, and T. Venkatesan, Phys. Rev. Lett. 69, 2709 (1992). 25
- [50] J. Mannhart, J. Ströbel, J. G. Bednorz, and C. Gerber, Appl. Phys. Lett. 62, 630 (1993). 25
- [51] J. Mannhart, Supercond. Sci. Technol. 9, 49 (1996). 25
- [52] H. L. Stadler, Phys. Rev. Lett. 14, 979 (1965). 26

- [53] J. Bardeen, L. N. Cooper, and J. R. Schrieffer, Phys. Rev. 108, 1175 (1957). 26
- [54] P. W. Anderson, Science 235, 1196 (1987). 26
- [55] J. Orenstein and A. J. Millis, Science 288, 468 (2000). 26
- [56] A. S. Alexandrov and N. F. Mott, Rep. Prog. Phys. 57, 1197 (1994). 27, 28, 54
- [57] A. S. Alexandrov and J. Ranninger, Phys. Rev. B 23, 1796 (1981). 27
- [58] P. Monthoux and D. Pines, Phys. Rev. B 47, 6069 (1993). 28
- [59] C. B. Sawyer and C. H. Tower, Phys. Rev. 35, 269 (1930). 30
- [60] B. Jaffe, W. R. Cook, and H. Jaffe, *Piezolectric Ceramics* (R.A.N. Publishers, International edition, 1971). 30, 37
- [61] Ashcroft and Mermin, Solid State Physics (Sauders College Publishing, International edition, 1976).
 31
- [62] V. V. Lemanov and A. L. Kholkin, Phys. Solid State 36, 841 (1994). 31
- [63] T. Terashima, Phys. Rev. Lett. 67, 1362 (1991). 33
- [64] J.-M. Triscone and Ø. Fischer, Rep. Prog. Phys. **60**, 1673 (1997). 33, 34, 35
- [65] H. Y. Zhai and W. K. Chu, Appl. Phys. Lett. 76, 3469 (2000). 35
- [66] R. Jin and H. R. Ott, Phys. Rev. B 57, 13872 (1998). 35, 51, 59
- [67] T. Ito, K. Takenaka, and S. Uchida, Phys. Rev. Lett. 70, 3995 (1993). 35, 51
- [68] A. Carrington, A. P. Mackenzie, C. T. Lin, and J. R. Cooper, Phys. Rev. Lett. 69, 2855 (1992). 35, 43, 59
- [69] J. T. Kucera and J. C. Bravman, Phys. Rev. B 51, 8582 (1995). 36
- [70] O. Kuffer, Ph.D. thesis, DPMC, University of Geneva, 2001. 39
- [71] A. M. Goldman and N. Markovic, Phys. Today 11, 39 (1998). 42
- [72] S. Ono, Y. Ando, T. Murayama, F. F. Balakirev, J. B. Betts, and G. S. Boebinger, Phys. Rev. Lett. 85, 638 (2000). 46
- [73] Y. Ando, G. S. Boebinger, A. Passner, T. Kimura, and K. Kishio, Phys. Rev. Lett. 75, 4662 (1995).
- [74] G. S. Boebinger, Y. Ando, A. A. Passner, T. Kimura, M. Okuya, J. Shimoyama, K. Kishio, K. Tamasaku, N. Ichikawa, and S. Uchida, Phys. Rev. Lett. 77, 5417 (1996). 46
- [75] P. Fournier, P. Moanty, E. Maiser, S. Darzens, T. Venkatesan, C. J. Lobb, G. Czjzek, R. A. Webb, and R. L. Greene, Phys. Rev. Lett. 81, 4720 (1998). 46
- [76] F. F. Balakirev, J. B. Betts, G. S. Boebinger, N. Motoyama, H. Eisaki, and S. Uchida, cond-mat 9808284, (1998). 46
- [77] M. Kastner, R. J. Birgeneau, G. Shirane, and Y. Enodh, Rev. Mod. Phys. 70, 897 (1998). 46
- [78] N. W. Preyer, Phys. Rev. B 39, 11563 (1989). 46
- [79] M. Gurvitch and A. T. Fiory, Phys. Rev. Lett. 59, 1337 (1987). 48
- [80] T. R. Chien, Z. Z. Yang, and N. P. Ong, Phys. Rev. Lett. 67, 2088 (1991). 48
- [81] J. M. Harris, Y. F. Yan, and N. P. Ong, Phys. Rev. B 46, 14293 (1992). 48
- [82] B. Grevin, private communication. 49

- [83] T. Tybell, C. H. Ahn, and J.-M. Triscone, Appl. Phys. Lett. **72**, 1454 (1998). **50**
- [84] P. Paruch, T. Tybell, and J.-M. Triscone, Appl. Phys. Lett. **79**, 530 (2001). 50
- [85] T. Tybell, Ph.D. thesis, DPMC, University of Geneva, 2000. 50
- [86] D. Matthey, S. Gariglio, B. Giovannini, and J.-M. Triscone, Phys. Rev. B 64, 24513 (2001). 51, 59
- [87] B. Stojkovic and D. Pines, Phys. Rev. B **55**, 8576 (1997). **55**
- [88] M. R. Norman, H. Ding, M. Randeria, J. C. Campuzano, T. Yokoya, T. Takeuchi, T. Takahashi, T. Mochiku, K. Kadowaki, P. Guptasarma, and D. G. Hinks, Nature **392**, 157 (1998). 56
- [89] H. Ding, T. Yokoya, J. C. Campuzano, T. Takahashi, M. Randeria, M. R. Norman, T. Mochiku, K. Kadowaki, and J. Giapintzakis, Nature **382**, 51 (1996). 56
- [90] A. G. Loeser, Z. X. Shen, D. S. Dessau, D. S. Marshall, C. H. Park, P. Fournier, and A. Kapitulnik, Science 273, 325 (1996). 56
- [91] H. Y. Hwang, B. Batlogg, H. Takagi, H. L. Lao, J. Kwo, R. J. Cava, J. J. Krajewski, and W. F. Peck Jr., Phys. Rev. Lett. 72, 2636 (1994).
- [92] J. E. Hirsch and F. Marsiglio, Physica C 195, 355 (1992). 59
- [93] F. Lichtenberg, T. Williams, A. Reller, D. Widmer, and J. G. Bednorz, Z. Phys. B 84, 369 (1991).
- [94] S. Nanamatsu, M. Kimura, K. Doi, S. Matsushita, and N. Yamada, Ferroelectrics 8, 511 (1974). 61
- [95] A. Ohtomo, D. A. Muller, J. L. Grazul, and H. Y. Hwang, Appl. Phys. Lett. 80, 3922 (2002). 62
- [96] A. Ohtomo, D. A. Muller, J. L. Grazul, and H. Y. Hwang, Nature 419, 378 (2002). 62
- [97] A. Schmehl, F. Lichtenberg, D. G. Schlom, H. Bielefeldt, and J. Mannhart, submitted to Appl. Phys. Lett. (2003). 62
- [98] J. Fompeyrine, J. W. Seo, and J.-P. Locquet, J. Eur. Ceram. Soc. 19, 1493 (1999). 62
- [99] J. W. Seo, J. Fompeyrine, and J.-P. Locquet, Phys. Rev. B 63, 205401 (2001). 62, 63
- [100] C. C. Hays, J. S. Zhou, J. T. Markert, and J. B. Goodenough, Phys. Rev. B 60, 10367 (1999). 68
- [101] D. A. Crandles, T. Timusk, and J. E. Greedan, Phys. Rev. B 44, 13250 (1991). 68
- [102] W. F. Brinkman and T. M. Rice, Phys. Rev. B 2, 4302 (1970). 71
- [103] G. K. White and R. Tainsh, Phys. Rev. Lett. 19, 165 (1967). 71
- [104] A. Fujimori, I. Hase, M. Nakamura, Y. Fujishima, Y. Tokura, M. Abbate, F. M. F. de Groot, M. Czyzyk, J. C. Fuggle, O. Strebel, F. Lopez, M. Domke, and G. Kaindl, Phys. Rev. B 46, 9841 (1992).
 71
- [105] N. F. Mott and E. A. Davis, *Electronic processes in non-crystalline materials* (Clarendon Press, Oxford, 1979). 72
- [106] G. Zhao, V. Smolyaninova, W. Prellier, and H. Keller, Phys. Rev. Lett. 84, 6086 (2000). 73
- [107] G. Zhao, H. Keller, and W. Prellier, J. Phys. Condens. Matter 12, 361 (2000). 73
- [108] J. Sunstrom, S. Kauzlarich, and P. Klavins, Chem. Mater. 4, 346 (1992). 74
- [109] M. J. MacEachern, H. Dabkowska, J. D. Garrett, G. Amow, W. Gong, G. Liu, and J. E. Greedan, Chem. Mater. 6, 2092 (1994). 74